Measurement of the polarization of τ–leptons produced in Z^0 decays at CMS and determination of the effective weak mixing angle $\sin^2\theta_{eff}$

Von der Fakultät für Mathematik, Informatik und Naturwissenschaften der RWTH Aachen University zur Erlangung des arkademischen Grades eines Doktors der Naturwissenschaften genehmigte Dissertation

vorgelegt von

Diplom-Physiker

Vladimir Cherepanov

aus Kustanay/Russland

Berichter: Prof. Dr. Achim Stahl

Prof. Dr. Wolfgang Lohmann

Tag der mündlichen Prüfung: 1. July 2016

Abstract

In this thesis the first measurement of the τ-lepton polarization in $Z \to \tau\tau$ decays is performed at a proton-proton collider. A sample of 8818 events of the decay $Z^0 \to \tau^+\tau^- \to \mu\nu\nu$, $a_1\nu$ is used. It is selected in data corresponding to a luminosity of 19.6 fb^{-1} collected by the CMS detector at 8 TeV. The average polarization is measured to be:

$$< P_\tau >= -0.1261 \pm 0.073(stat)^{+0.018}_{-0.019}(syst).$$

From the value of the measured τ polarization the effective weak mixing angle is derived:

$$\sin^2\theta_{eff} = 0.2336 \pm 0.0096.$$

The ratio of vector to axial-vector neutral current couplings for τ leptons derived from the measured value of $\sin^2\theta_{eff}$:

$$g_V^\tau / g_A^\tau = 0.0656 \pm 0.0384.$$

The result for the weak mixing angle is consistent with previous measurements and the value of the ratio between vector and axial-vector couplings supports lepton universality.

Zusammenfassung

In dieser Arbeit wird die erste Messung der Polarisation des τ-Leptons in $Z \to \tau\tau$ Zerfällen an einem Proton-Proton-Collider durchgeführt. Dazu werden Daten ausgewertet, die mit dem CMS-Detektor bei 8 TeV Schwerpunktsenergie aufgezeichnet wurden und einer integrierten Luminosität von 19.6 fb^{-1} entsprechen. Ein Datensatz von 8818 Ereignissen des Zerfalls $Z^0 \to \tau^+\tau^- \to \mu\nu\nu, a_1\nu$ wird zur Bestimmung der Polarisation genutzt. Die gemessene gemittelte Polarisation beträgt

$$< P_\tau >= -0.1261 \pm 0.073(stat)^{+0.018}_{-0.019}(syst).$$

Aus der gemessenen τ-Polarisation wird der effektive elektroschwache Mischungswinkel bestimmt zu

$$\sin^2 \theta_{eff} = 0.2336 \pm 0.0096.$$

Das Verhältnis zwischen Vektor- und Axialvektorkopplungen in neutralen Strömen ergibt sich daraus für τ-Leptonen zu

$$g_V^\tau / g_A^\tau = 0.0656 \pm 0.0384.$$

Der gemessene Wert des elektroschwachen Mischungswinkels ist konsistent mit vorherigen Messungen. Das Verhältnis von Vektor- und Axialvektorkopplungen bekräftigt die Gültigkeit der Leptonuniversalität.

Contents

Figures

Chapter 1

Introduction

At the Large Electron-Positron collider, LEP, extensive measurements of the electroweak parameters with data taken at the Z^0 resonance have been performed [1] and the electroweak theory was tested on the level of quantum corrections. Today, the Large Hadronc Collider, LHC, provides the opportunity to improve the precision and to see possible indications of new physics. The parity violation in the weak neutral current introduces various asymmetries, in particular the τ lepton polarization asymmetry which can be experimentally accessed analyzing the τ lepton decay products. From the value of the τ polarization asymmetry the value of the weak mixing angle $\sin^2\theta_{eff}$ and the ratio of vector to axial-vector neutral couplings for τ leptons can be derived.

There is a discrepancy between the two most precise measurements of $\sin^2\theta_{eff}$, which are 0.23221 ± 0.00029 from the combined LEP measurements and 0.23098 ± 0.00026 from the SLD measurement [2]. An independent measurement is therefore important to probe the difference and clarify the situation, as well as to see the impact on the precision tests of the Standard Model.

A precise determination of the Z^0 couplings to τ leptons provides in addition a test of lepton universality in the neutral current. With the currently reached experimental precision these couplings are the same for all leptons. Any deviation would point to new physics.

The thesis is organized as follows: In Chapter 2 the Standard Model of electroweak interaction is briefly introduced. The various observable asymmetries in the process $f\bar{f} \rightarrow Z^0 \rightarrow \tau^+\tau^-$, the forward-backward asymmetry, the τ polarization asymmetry, the forward-backward polarization asymmetry and their connection to the weak mixing angle are described. In Chapter 3 the Drell-Yan process and parton density functions are briefly introduced. Chapter 4 summarizes the static properties and the decay structure of τ leptons. The polarization observables in the decay $\tau \rightarrow a_1\nu \rightarrow 3\pi\nu$ and the decay model of $a_1 \rightarrow 3\pi$ are described in Chapter 5. In Chapter 6 the main features of the LHC and CMS detector are given. Chapter 7 describes the standard τ lepton reconstruction at CMS, the selection of $Z \rightarrow \tau\tau \rightarrow a_1\nu, \mu\nu\nu$ events , and the estimation of the background. The Global Event Fit used to reconstruct the whole event kinematic is described in Chapter 8. Chapter 9 describes the measurement of the polarization asymmetry using the selected data events and the determination of the effective weak mixing angle. Summary and comments about the future prospects of the τ polarization measurement at CMS are given in Chapter 10.

Chapter 2

The Standard Electroweak Model

2.1 Concept and Couplings

The whole physics is revolving around symmetries. From classical physics it is known that, e.g. the time translation symmetry gives conservation of energy, space translation symmetry gives conservation of momentum, rotation symmetry gives conservation of angular momentum. In other words, any conservation law follows from symmetry properties of nature. The numerical expression of this principle is given by the Noether theorem [3], which is as important in physics as Pythagorean theorem in geometry. Modern quantum field theories are gauge invariant theories i.e. they are theories where the Lagrangian, which describes the interaction dynamics, does not change when a gauge transformation is performed. The Noether theorem turned out to be fruitful in particle physics. For example, the Lagrangian for a free electron $\psi(x)$ derived from Dirac equation reads:

$$\mathcal{L} = i\bar{\psi}\gamma_{\mu}\partial^{\mu}\psi - m\bar{\psi}\psi. \tag{2.1}$$

Analyzing (2.1) one can notice that it is invariant under phase transformations $\psi(x) \rightarrow e^{i\alpha}\psi(x)$. From Noether theorem it follows that such invariance leads to the conservation of the electromagnetic current $\partial_{\mu}e\bar{\psi}\gamma^{\mu}\psi$ =0, or equivalently to the conservation of the electric charge $Q = \int d^3xj^0$. Transformations like $U(\alpha) = e^{i\alpha}$ with α being any real value form the group $U(1)$ and the symmetry of $\mathcal{L}$ under $U(1)$ transformation is called *global* gauge invariance. However, this choice of calibration is not general and the further natural step is to require the Lagrangian to be invariant under a stronger requirement of a *local* gauge transformation where $\alpha(x)$ is a function of space and time. One can show that the requirement of local gauge invariance generates a massless vector particle which interacts with an electron in the same manner as a photon field, and eventually one can build a quantum electrodynamics (QED) Lagrangian which can be used to give quantitative predictions. Various precision tests of QED have been performed, all show that QED is the most precise theory so far. The most impressive one is the high precision measurement of the anomalous magnetic moment of the electron whose best value in terms of the g factor is g/2 = 1.00115965218073(28) [4]. QED correctly predicts all these decimal digits!

The situation with the weak interaction is somewhat more complex. However the same gauge principles can be used to build a theory for quantitative predictions. Indeed, qualitatively in QED the transition of an electron from one state to another with a phase shift $e^- \rightarrow e^-$, required the radiation or absorption of a photon $e^- \rightarrow e^-\gamma$. One can define the gauge transformation that not only changes the phase but transforms leptons and neutrinos:

$$l^- \to \nu_l \qquad \nu_l \to l^- \qquad \nu_l \to \nu_l \qquad l^- \to l^- \tag{2.2}$$

And similarly as in QED the requirement that the Lagrangian is invariant under this gauge group will generate weak vector fields, i.e. gauge bosons.

A long time an effective current-current model was used to give numerical predictions for weak processes. The existence of heavy vector boson $W^{\pm}$ for the calculation of low energy amplitudes ($|q^2| \ll 100$ GeV) does not play a big role and effectively can be accounted for by the definition of Fermi constant, G_F. Calculation of other amplitudes besides low energy leads to problems in this approach. The assumption of the existence of heavy vector bosons was the first step towards building a renormalizable theory of weak interactions and to unify it with the electromagnetic interaction. The collected experimental data pointed to the $SU(2)_L \times U_Y$ gauge group for electroweak interaction and was suggested by Glashow [5] in 1961 long before the discovery of the neutral current. Later S. Weinberg [6] and A. Salam [7] extended the model and included massive vector bosons ($W^{\pm}, Z^0$). The theory is often called the Standard Model of electroweak interaction (SM).

In this theory fermions are grouped into left-handed weak *isospin* doublets and right-handed singlets. The weak charged currents are contained in the $SU(2)_L$ sub-group where the index L denotes left-handed *chiral* particles, or right-handed anti-particles, i.e. expressing the V-A structure of the weak charged currents. Because the generators of the $SU(2)$ group are 2×2 matrices the wave function is defined as an isospin doublet:

$$\psi_L = \begin{pmatrix} \nu_l \\ l \end{pmatrix}_L . \tag{2.3}$$

The weak isospin is defined similarly as, for example, the isospin for proton and neutron. The ν_l and l^- have weak isospin $I_W = \frac{1}{2}$ with the third components $I_W^3(\nu_l) = +1/2$ and $I_W^3(l^-) = -1/2$. From experiment it is known that charged weak currents interact only with left-handed particles and right-handed anti-particles. For this reason the right-handed particles and left-handed anti-particles are defined as a weak isospin singlet, $I_W = 0$. The charged currents $j_\mu^{\pm}$ can be written in compact form:

$$j_\mu^{\pm} = \bar{\psi}_L \gamma_\mu \tau_{\pm} \psi_L, \tag{2.4}$$

where $\tau_{\pm} = (1/2)(\tau_1 \pm \tau_2)$ are charge raising or lowering operators, and $\tau_{1,2}$ are the Pauli matrices:

$$\tau_+ = \begin{pmatrix} 0 & 1 \\ 0 & 0 \end{pmatrix} \qquad \tau_- = \begin{pmatrix} 0 & 0 \\ 1 & 0 \end{pmatrix}. \tag{2.5}$$

Using (2.3) one can also define a neutral current as:

$$j_\mu^3 = \frac{1}{2}\bar{\psi}_L \gamma_\mu \tau_3 \psi_L = \frac{1}{2}\bar{\nu}_L \gamma_\mu \nu_L - \frac{1}{2}\bar{e}_L \gamma_\mu e_L. \tag{2.6}$$

The currents j_μ^i (i=1,2,3) form the weak isotriplet. The current (2.6), however, can not be associated with the weak neutral current because, as known from experimental data, the weak neutral current interacts with right- and left-handed particles, although, not equally. In order to save the experimentally observed $SU(2)_L$ symmetry and correctly introduce the neutral current, the EM current $j^{EM}_\mu = \bar{\psi}\gamma_\mu\psi$ is used. Particularly, one can introduce a new current j^Y_μ which does not change under $SU(2)_L$ transformations and interacts with both chirality states of fermions. This current j^Y_μ is called weak hypercharge current and is given by combination of j^3_μ and j^{EM}_μ:

$$j^Y_\mu = \bar{\psi}\gamma_\mu Y\psi = 2Qj^{EM}_\mu - 2I^W_3 j^3_\mu, \tag{2.7}$$

where hypercharge Y is defined as $Y = 2Q - 2I^W_3$. From (2.7) for electrons one obtains:

$$j^Y_\mu = 2Qj^{EM}_\mu - 2I^W_3 j^3_\mu = -2(\bar{e}_R\gamma_\mu e_R) - 1(\bar{\psi}_L\gamma_\mu\psi_L). \tag{2.8}$$

Therefore for the isodoublet $\binom{\nu_l}{l}_L$ the hypercharge is $Y = -1$, while for the isosinglet e_R $Y = -2$. In the same way the weak eigenstates of quarks are grouped in left-handed doublets and right-handed singlets. The summary on hypercharge and weak isospin for fermions is given in Table 2.1.

Table 2.1: The electric charge, hypercharge, weak isospin and its third component for fermions in the Standard Model

Fermion type	Generations			Q	Y	I_W	I^3_W
Leptons	$\begin{pmatrix}\nu_e\\e^-\end{pmatrix}_L$	$\begin{pmatrix}\nu_\mu\\\mu^-\end{pmatrix}_L$	$\begin{pmatrix}\nu_\tau\\\tau^-\end{pmatrix}_L$	0 -1	-1 1	$-1/2$ $1/2$	$+1/2$ $-1/2$
	e^-_R	μ^-_R	τ^-_R	-1	-2	0	0
Quarks	$\begin{pmatrix}u\\d'\end{pmatrix}_L$	$\begin{pmatrix}c\\s'\end{pmatrix}_L$	$\begin{pmatrix}t\\b'\end{pmatrix}_L$	$+2/3$ $-1/3$	$+1/3$ $+1/3$	$1/2$ $1/2$	$+1/2$ $-1/2$
	u_R	c_R	t_R	$+2/3$	$+4/3$	0	0
	d'_R	s'_R	b'_R	$-1/3$	$-2/3$	0	0

The introduction of the hypercharge extends the symmetry group $SU(2)_L$ to $SU(2)_L \times U(1)_Y$. This is the idea of electroweak unification, but at this point the unification is not full because there are two uncoupled symmetries.

Analogically to QED, the local gauge invariance under local $SU(2)_L \times U(1)_Y$ phase transformation generates massless gauge bosons that interact with currents of weak isospin and weak hypercharge:

$$-igj_{i\mu}W^{i\mu} - i\frac{g'}{2}j^Y_\mu B^\mu, \tag{2.9}$$

here $W_{i\mu}$ is a $SU(2)_L$ triplet of gauge fields with coupling g to a triplet of weak isovector currents j^μ_i and B_μ is the $U(1)_Y$ vector field with coupling $g'/2$ to the hypercharge current (the factor $1/2$ is conventional).

So far all gauge bosons are massless, since the demand on the Lagrangian to be gauge invariant does not allow gauge fields to have a mass term. However in nature $W^{\pm}$, Z^0 have been observed to have a mass. The masses of gauge bosons can be induced by introducing a scalar (Higgs) field with a special potential, in a way that the full Lagrangian is invariant under $SU(2)_L \times U(1)_Y$ but the ground state is not. This mechanism is called spontaneous symmetry breaking [8].

After applying the spontaneous breaking of local gauge symmetry $SU(2)_L \times U(1)_Y$ fields $W^{\pm}_{\mu} = \sqrt{\frac{1}{2}}(W^1_{\mu} \mp W^2_{\mu})$ acquire mass and correspond to massive vector bosons $W^{\pm}$, while the neutral fields W^3_{μ} and B_{μ} are mixing with an angle $\sin\theta_W$ forming the massless vector boson A_{μ}(photon) and massive Z_{μ} (Z boson):

$$\begin{aligned} A_{\mu} &= B_{\mu}\cos\theta_W + W^3_{\mu}\sin\theta_W, \\ Z_{\mu} &= -B_{\mu}\sin\theta_W + W^3_{\mu}\cos\theta_W. \end{aligned} \tag{2.10}$$

The angle θ_W is called weak mixing angle.

Using Eq. (2.9) and (2.10) the weak neutral current can be written as:

$$-igj_{3\mu}W^{3\mu} - i\frac{g'}{2}j^Y_{\mu}B^{\mu} = -i(g\sin\theta_W j_{3\mu} + g'\cos\theta_W\frac{j^Y_{\mu}}{2})A^{\mu} - i(g\cos\theta_W j_{3\mu} - g'\sin\theta_W\frac{j^Y_{\mu}}{2})Z^{\mu}. \tag{2.11}$$

The term proportional to A^{μ} describes the electromagnetic interaction and thus the expression in brackets should be equal to Eq.(2.7):

$$ej^{EM}_{\mu} = e(j^3_{\mu} + \frac{1}{2}j^Y_{\mu}). \tag{2.12}$$

Consequently the relation between g and g' is:

$$g\sin\theta_W = g'\cos\theta_W = e, \tag{2.13}$$

where e is the unit charge. The second term in (2.11) is the weak neutral current interaction. Using Eq. (2.11) and (2.7) it can be written in the form:

$$-i(g\cos\theta_W j_{3\mu} - g'\sin\theta_W\frac{j^Y_{\mu}}{2})Z^{\mu} = -i\frac{g}{\cos\theta_W}(j^3_{\mu} - \sin^2\theta_W j^{EM}_{\mu}), \tag{2.14}$$

where the expression in brackets is the weak neutral current:

$$j^{NC}_{\mu} = j^3_{\mu} - \sin^2\theta_W j^{EM}_{\mu}. \tag{2.15}$$

It is more convenient to rewrite (2.15) in terms of fermion spinors ψ_f with the electrical charge Q and the third component of weak isospin I^3_W:

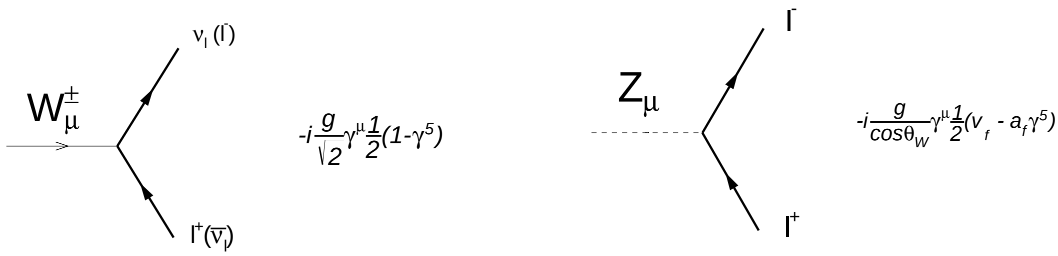

Figure 1: Vertex factors for $W \to l\nu_l$ and $Z \to l^+l^-$.

$$
\begin{aligned}
j^{NC}_{\mu} = \bar{\psi}_f\gamma^{\mu}[\frac{1}{2}(1-\gamma^5)I^3_W - Q\sin^2\theta_W]\psi_f = \bar{\psi}_f\gamma^{\mu}\frac{1}{2}(v_f - a_f\gamma^5)\psi_f \\
= \frac{g_L}{2}\bar{\psi}_L\gamma^{\mu}\psi_L + \frac{g_R}{2}\bar{\psi}_R\gamma^{\mu}\psi_R,
\end{aligned} \tag{2.16}
$$

where the following definitions were used:

$$
\begin{aligned}
v_f &= I^3_W - 2Q\sin^2\theta_W \\
a_f &= I^3_W \\
g_L &= v_f + a_f \\
g_R &= v_f - a_f.
\end{aligned} \tag{2.17}
$$

From Eq. (2.16) follows that the weak neutral current does not change the fermion type, i.e. translates a fermion to itself. For charged fermions it couples to both left- and right-handed components as g_L and g_R, respectively ($g_L \neq g_R$). Values of g_L, g_R, v_f and a_f for fermions are given in Table. 2.2. The vertex factors for weak charged and weak neutral current interaction are shown in Fig. 1.

Table 2.2: Couplings for $Z \to f\bar{f}$ in Standard Model (with $\sin^2\theta_W = 0.231$).

f	Q_f	v_f	a_f	g_R	g_L
ν_e, ν_μ, ν_τ	0	$\frac{1}{2}$	$+\frac{1}{2}$	0	1
e^-, μ^-, τ^-	-1	$-\frac{1}{2} + 2\sin^2\theta_W \approx -0.037$	$-\frac{1}{2}$	0.463	-0.537
u, c, t	$+\frac{2}{3}$	$\frac{1}{2} - \frac{4}{3}\sin^2\theta_W \approx 0.191$	$+\frac{1}{2}$	-0.309	0.691
d, s, b	$-\frac{1}{3}$	$-\frac{1}{2} + \frac{2}{3}\sin^2\theta_W \approx -0.345$	$-\frac{1}{2}$	0.155	-0.845

One can derive the relation between g and the Fermi constant G_F by requiring the agreement between the effective Fermi V-A calculation of beta decay and Standard Model calculation:

$$\frac{G_F}{\sqrt{2}} = \frac{g^2}{8M_W^2} = \frac{\pi\alpha}{2\sin^2\theta_W M_W^2}, \tag{2.18}$$

where M_W is the mass of the W boson and $\alpha = e^2/4\pi$ the fine-structure constant. The Standard Model also predicts the relative strength of weak charged and neutral interactions through the parameter ρ:

$$\rho = \frac{M_W^2}{M_Z^2 \sin^2\theta_W}. \tag{2.19}$$

With the simplest choice of the Higgs field as an isospin doublet the parameter ρ is fixed and equal to 1. Other choices of the Higgs sector may lead to a different relation between masses of bosons. Measurements show that with good precision the parameter ρ is 1 [2]. Combination of Eq. (2.18) and (2.19) with $\rho = 1$ relates the weak mixing angle to precisely measured Standard Model quantities:

$$\sin^2\theta_W \cos^2\theta_W = \frac{\pi\alpha}{\sqrt{2}G_F M_Z^2}. \tag{2.20}$$

From Eq. 2.17 and values in Table 2.1 one can derive a useful relation between the weak mixing angle and the ratio of vector and axial-vector couplings of charged leptons:

$$\frac{v_f}{a_f} = 1 - 4\sin^2\theta_W. \tag{2.21}$$

This equation and its relation to the observable quantities in the process $Z \to \tau^+\tau^-$ will be discussed in Chapter 2.3.

2.2 Helicity and Chirality

In this chapter a brief discussion on two important concepts, *Helicity* and *Chirality*, as well as the connection between them, is given. It is often convenient to analyze the cross section in terms of spin states of particles involved. The helicity of a particle is defined as the projection of spin along the particle momentum:

$$h = \frac{\vec{S}\vec{p}}{p}. \tag{2.22}$$

One can show that for a four-component spinor, the helicity operator:

$$\hat{h} = \frac{\hat{\Sigma}\hat{p}}{2p} = \frac{1}{2p}\begin{pmatrix} \hat{\sigma}\hat{p} & 0 \\ 0 & \hat{\sigma}\hat{p} \end{pmatrix}, \tag{2.23}$$

commutes with the Dirac Hamiltonian and therefore helicity is a conserved quantum number, i.e. one can introduce definite helicity states. For a spin-half particle, the components of spin quantized along any axis can be either $\pm 1/2$. Consequently, eigenvalues of the helicity

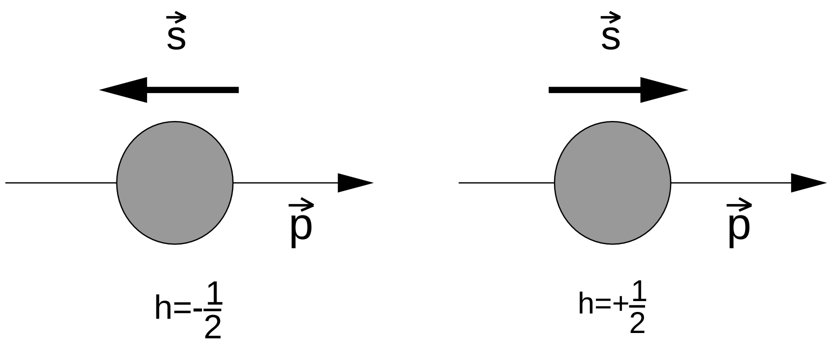

Figure 2: The negative (left) and positive (right) helicity states. The thin arrows show the momentum and the thick arrow indicates the spin projection.

operator (2.23) are $\pm 1/2$. The two possible helicity states of a spin-half fermion are shown in Fig. 2, and usually referred to as $h = -1$ and $h = 1$ helicity states.

The helicity is not Lorentz-Invariant, as can be noticed in (2.23), since the spin operator is multiplied by a three-momentum. For a massive particle one can always find a reference frame in which the direction of the particle is reversed and therefore helicity changes the sign. The related Lorentz-Invariant concept is *Chirality*. Qualitatively, the chirality expresses different properties of the Dirac spinor components under space rotation. A left-chiral particle, for example, can have either helicity $-1/2$ and $1/2$ state depending on the reference frames relative to the particle. But in all reference frame the particle will still be in left-chiral state, regardless of the helicity. Quantitatively chirality is introduced using the γ^5 operator, defined as:

$$\gamma^5 = i\gamma^0\gamma^1\gamma^2\gamma^3 = \begin{pmatrix} 0 & 0 & 1 & 0 \\ 0 & 0 & 0 & 1 \\ 1 & 0 & 0 & 0 \\ 0 & 1 & 0 & 0 \end{pmatrix}. \tag{2.24}$$

Eigenstates of the γ^5 operator define left- and right-chiral states, such that for fermions:

$$\gamma^5 u_R = u_R \qquad \gamma^5 u_L = -u_L. \tag{2.25}$$

Any Dirac spinor ψ can be decomposed into the left- and right-chiral states using the projection operators, P_L and P_R:

$$\begin{aligned} P_L &= \frac{1}{2}(1 - \gamma^5), \\ P_R &= \frac{1}{2}(1 + \gamma^5). \end{aligned} \tag{2.26}$$

In order to establish a quantitative relation between helicity and chirality states one can decompose the general form of the helicity spinor into left- and right-chiral components. For example the general $h = +1$ helicity solution of the Dirac equation, with spin along the z-axis is (see for example [9]):

$$u_\uparrow = N \begin{pmatrix} 1 \\ 0 \\ \frac{|\vec{p}|}{E+m} \\ 0 \end{pmatrix}. \tag{2.27}$$

Projecting out the helicity spinor onto left- and right-chiral states using operators (2.26) gives:

$$\begin{aligned} P_L u_\uparrow &= \frac{1}{2}N(1 - \frac{|\vec{p}|}{E+m}) \begin{pmatrix} 1 \\ 0 \\ -1 \\ 0 \end{pmatrix} = \frac{1}{2}N(1 - \frac{|\vec{p}|}{E+m})u_L, \\ P_R u_\uparrow &= \frac{1}{2}N(1 + \frac{|\vec{p}|}{E+m}) \begin{pmatrix} 1 \\ 0 \\ 1 \\ 0 \end{pmatrix} = \frac{1}{2}N(1 + \frac{|\vec{p}|}{E+m})u_R. \end{aligned} \tag{2.28}$$

And hence:

$$u_\uparrow = P_L u_\uparrow + P_R u_\uparrow = \frac{1}{2}N(1 - \frac{|\vec{p}|}{E+m})u_L + \frac{1}{2}N(1 + \frac{|\vec{p}|}{E+m})u_R. \tag{2.29}$$

In the limit ($m \ll E$) the first term in Eq. (2.29) tends to zero and $u_\uparrow = P_R u_\uparrow$, which means that in the ultra relativistic limit (or in the limit of massless particle) the chirality and helicity are the same.

Using Eq. (2.29) one can explain, for example, the suppression of the τ decay $\tau^- \rightarrow \pi^- \nu_\tau$ (branching fraction $\mathcal{B} \approx 10\%$) compared to the not suppressed decay into the about 6 times heavier ρ resonance, $\tau^- \rightarrow \rho^- \nu_\tau$ ($\mathcal{B} \approx 25\%$). The charged pions are $J^P = 0^{-1}$ states formed of $d\bar{u}$ or $u\bar{d}$ quarks. In the decay τ to $d\bar{u}$, in the rest frame of $d\bar{u}$, quarks are emitted back-to-back. In order to make a spin-0 state, helicities of $\bar{d}$ and u must be the same, but since the weak interaction couples only to the left-chiral particle state and the right-chiral antiparticle state one of the quarks is produced with the *wrong* helicity, i.e. a left-chiral quark with positive helicity or the right-chiral anti-quark with negative helicity as shown in Fig. 3.

According to (2.29), the amplitude for the production of the *wrong* helicity state (for the upper sketch in Fig. 3) is proportional to the size of left-chiral component in the right-helicity state:

$$M \propto (1 - \frac{|\vec{p}|}{E+m_d}) \approx \frac{m_d}{m_\pi + m_d} \approx \frac{m_d}{m_\pi}. \tag{2.30}$$

Adding the second amplitude (lower sketch in Fig. 3)) the total suppression factor for the production of two quarks in a spin-0 state is

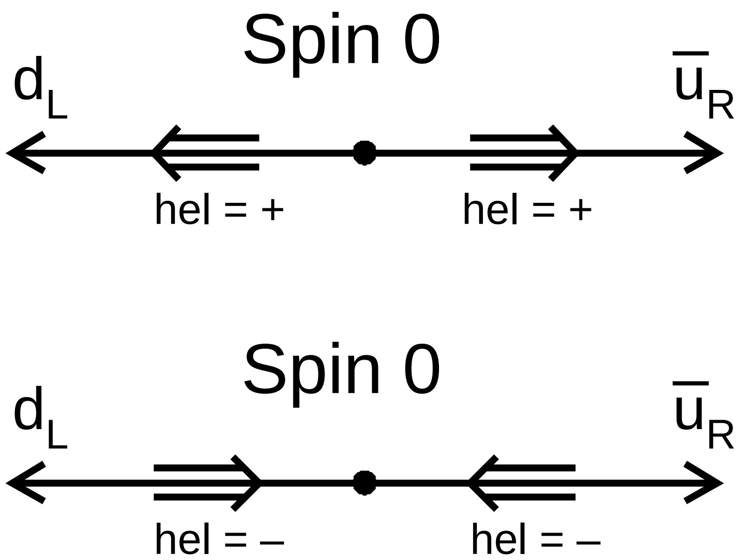

Figure 3: The two spin configurations providing spin-0 state in the decay $\tau \to \pi\nu$.

$$M \propto \frac{m_d}{m_\pi} + \frac{m_u}{m_\pi} + \mathcal{O}(\frac{m_{u/d}^2}{m_\pi^2}), \tag{2.31}$$

where $m_{u/d}$ is the mass of quark u/d and m_π the mass of the π meson.

2.3 The τ- Asymmetries

The decay $Z \to \tau\tau$ provides information on the relative strength of the neutral current vector and axial-vector couplings to τ leptons and initial quarks. This information can be extracted from the forward-backward asymmetry, polarization asymmetry and forward backward polarization asymmetry. The polarization asymmetry is a purely weak interaction effect arising from parity violation in the neutral current.

The four possible helicity states for $\tau^+\tau^-$ are:

$$h_{\tau^-}h_{\tau^+} = ++,\ \ --,\ \ +-,\ \ -+\,. \tag{2.32}$$

The polarization asymmetry for τ^- and τ^+ is then defined as:

$$\begin{aligned} P_{\tau^-} &= \frac{[\sigma_{++} + \sigma_{+-}] - [\sigma_{--} + \sigma_{-+}]}{\sigma_{total}}, \\ P_{\tau^+} &= \frac{[\sigma_{++} + \sigma_{-+}] - [\sigma_{--} + \sigma_{+-}]}{\sigma_{total}}, \end{aligned} \tag{2.33}$$

where σ_{++}, σ_{--}, σ_{+-} and σ_{-+} are cross sections that correspond to the helicity states in Eq. (2.32). $\sigma_{total} = \sigma_{++} + \sigma_{--} + \sigma_{+-} + \sigma_{-+}$ is the total cross section.

In the limit $\frac{m_\tau}{E_\tau} \to 0$, the helicities of τ^- and τ^+ are opposite to each other. The two contributions σ_{++} and σ_{--} are suppressed by a factor $1/\gamma = \frac{m_\tau}{E_\tau}$. At high energy the cross sections σ_{++} and σ_{--} are negligibly small and only σ_{+-}, σ_{-+} contribute to the τ polarization. Hence, from Eq. (2.33):

$$P_{\tau^-} = -P_{\tau^+}. \tag{2.34}$$

Hereafter the τ polarization asymmetry P_τ will always be referred to as the polarization of the τ^-.

In pp scattering, Z bosons and photons are formed by annihilation of quarks and antiquarks. The differential cross section of the process $q\bar{q} \to \tau\tau$, mediated by a vector boson at tree level, neglecting the transversal spin components of τ leptons, is derived in Appendix A to be:

$$\frac{d\sigma}{dcos\theta} = F_0(s)(1 + cos^2\theta) + 2F_1(s)cos\theta - h_\tau[F_2(s)(1 + cos^2\theta) + 2F_3(s)cos\theta], \tag{2.35}$$

where θ is the angle between the τ^- and the incoming anti-quark and h_τ the helicity of the τ^-. $F_i(s)$ are the structure functions describing the energy dependence of the cross section. They are given by:

$$\begin{aligned} F_0(s) &= \frac{\pi\alpha}{4s}[q_q^2 q_\tau^2 + 2Re\chi(s) q_q q_\tau v_q v_\tau + |\chi(s)|^2 (v_q^2 + a_q^2)(v_\tau^2 + a_\tau^2)], \\ F_1(s) &= \frac{\pi\alpha}{4s}[2Re\chi(s) q_q q_\tau a_q a_\tau + |\chi(s)|^2 2v_q a_q 2v_\tau a_\tau], \\ F_2(s) &= \frac{\pi\alpha}{4s}[2Re\chi(s) q_q q_\tau v_q a_\tau + |\chi(s)|^2 (v_q^2 + a_q^2) 2v_\tau a_\tau], \\ F_3(s) &= \frac{\pi\alpha}{4s}[2Re\chi(s) q_q q_\tau a_q v_\tau + |\chi(s)|^2 2v_q a_q (v_\tau^2 + a_\tau^2)]. \end{aligned} \tag{2.36}$$

F_0 comprises contributions from photon exchange, $\gamma - Z^0$ interference and Z^0 exchange, and F_1, F_2 and F_3 contributions from $\gamma - Z^0$ interference and Z^0 exchange. They also contain the charge and weak couplings of the initial quarks and thus depend on the quark flavour. For u and d quarks they are depicted in Fig. 4.

In order to obtain the cross section in pp collisions the $F_i(s)$ on Eq. (2.36) have to be averaged over the initial quark flavours. A factor α_u is introduced, describing the contribution of u/c quarks in the Z^0 formation. Using Monte Carlo simulation of the process $pp \to Z^0 \to \tau^-\tau^+$ the factor α_u is estimated to be 0.428. The averaged functions $F_i(s)$ and separately contributions from Z^0/γ exchange and their interference are shown in Fig. 5.

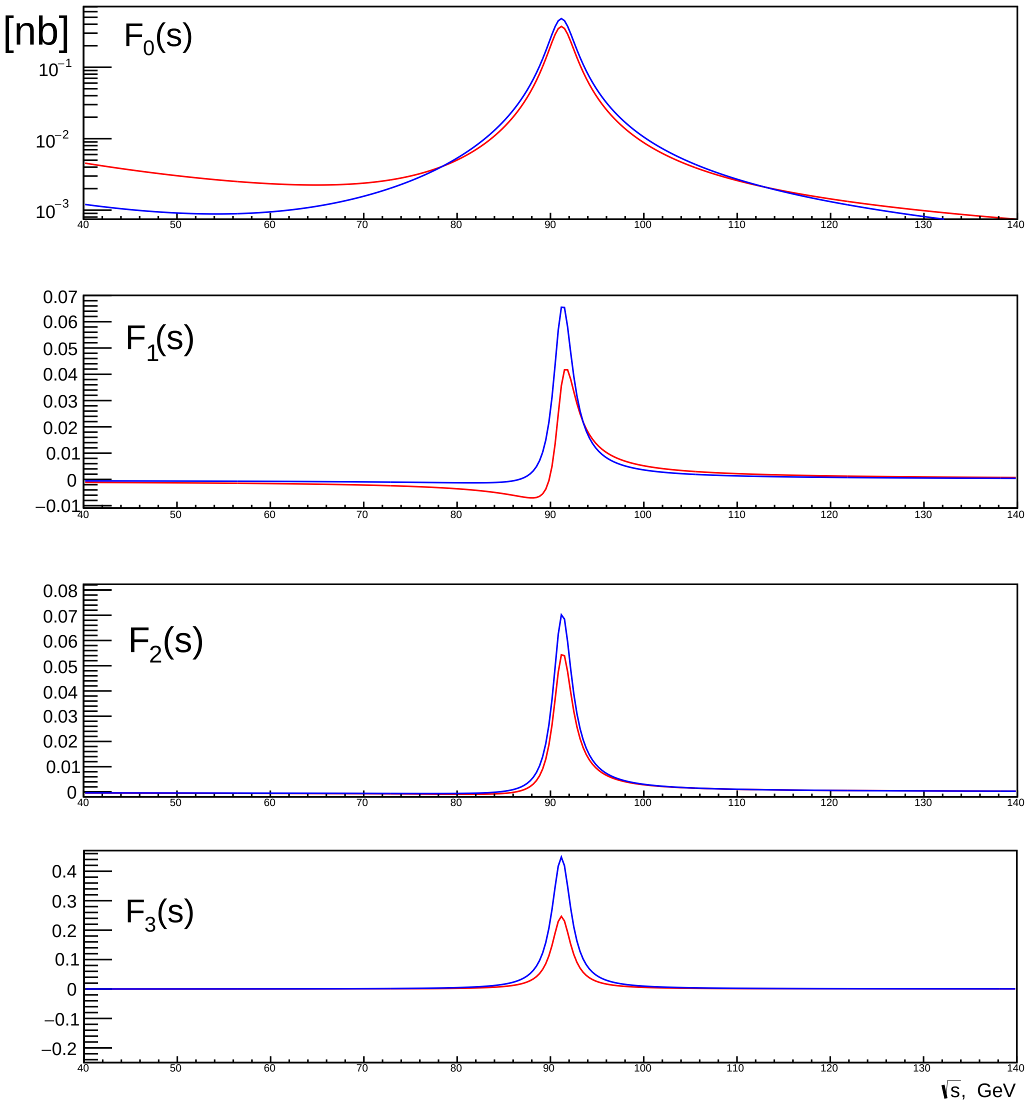

Figure 4: The functions F_i for the initial states $u\bar{u}$ (*blue*) and $d\bar{d}$ (*red*). *Horizontal axis*: center-of-mass energy in GeV; *vertical axis*: F_i in nanobarns. The parameters $m_Z = 91.1867 GeV$, $\Gamma_Z = 2.4939 GeV$, $sin^2\theta = 0.23155$ are used.

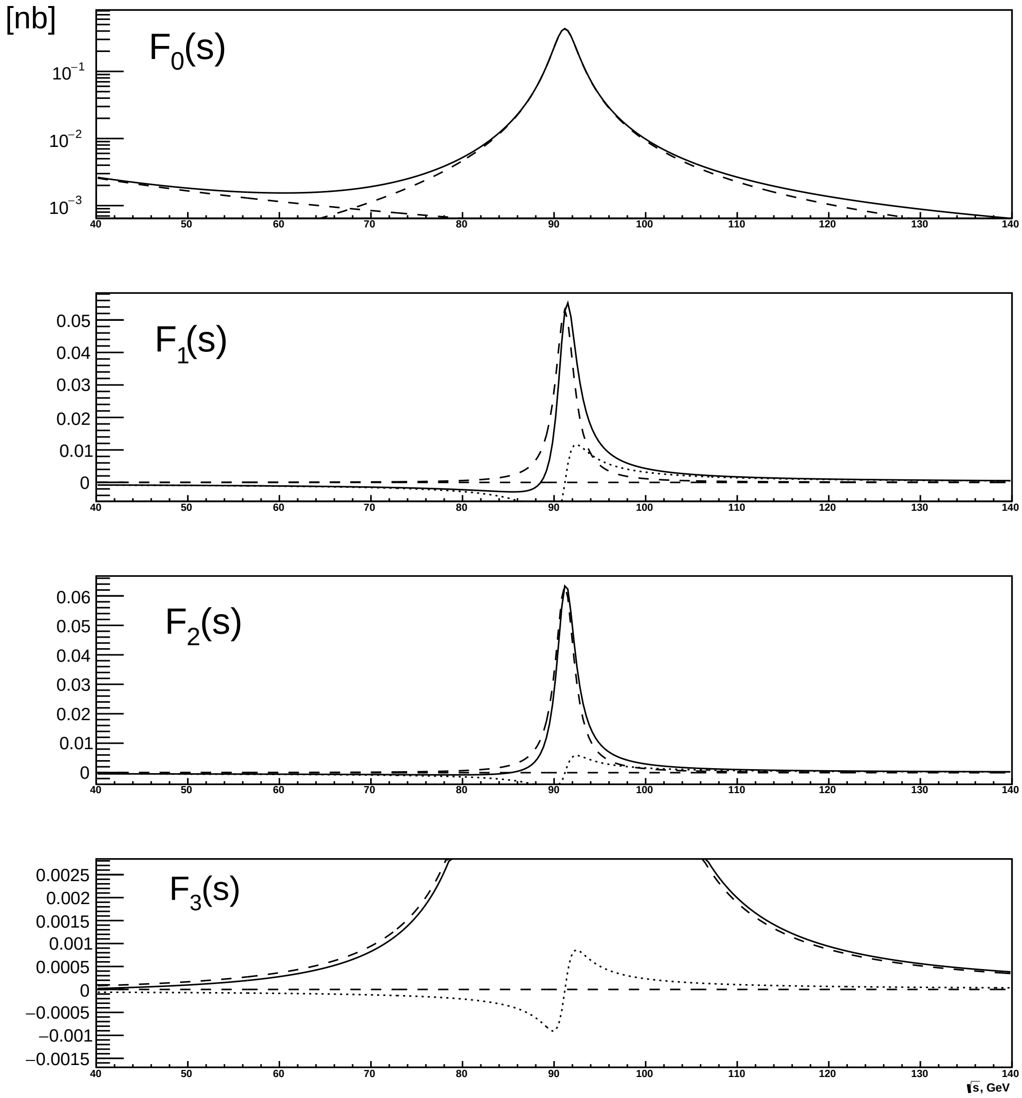

Figure 5: The averaged functions F_i. *Horizontal axis*: center-of-mass energy in GeV; *vertical axis*: F_i in nanobarns. The *solid line* is the total function, the dashed lines represent γ and Z^0 exchange, and the *dotted line* the interference term. The parameters $m_Z = 91.1867 GeV$, $\Gamma_Z = 2.4939 GeV$ and $sin^2\theta = 0.23155$ are used.

In total there are four helicity amplitudes that give non-zero contribution to the cross section (2.35), schematically shown in Fig. 6. The labels LL, LR, RR and RL denote the helicity of incoming quark and outgoing τ^-.

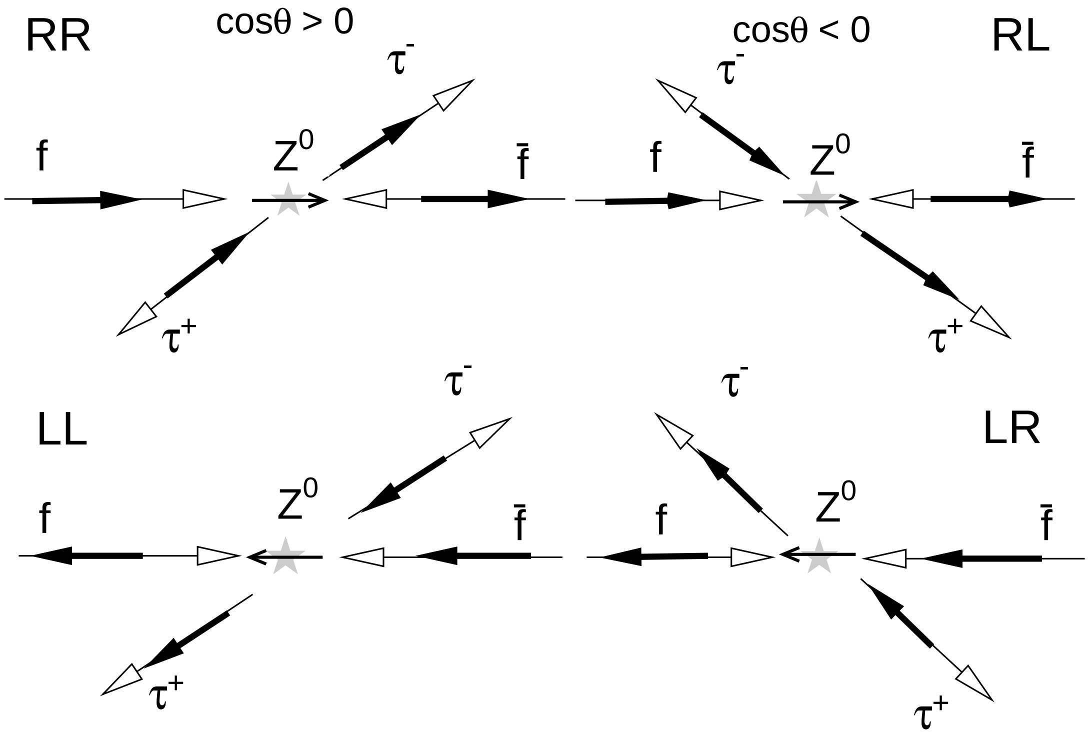

Figure 6: Orientation of helicities in τ production in forward (*left column*) and back scattering (*right column*). The open arrow indicates the direction of the momentum, the *solid arrow* the spin. The *arrow* in the center of each plot shows the spin of the Z^0.

From Eq. (2.35) one can construct the following observable cross sections:

$$
\begin{aligned}
\sigma^F(s) &= \sigma(s, h_{\tau^-} = +1, \cos\theta > 0) + \sigma(s, h_{\tau^-} = -1, \cos\theta > 0) = \frac{8}{3}F_0(s) + 2F_1(s) \\
\sigma^B(s) &= \sigma(s, h_{\tau^-} = +1, \cos\theta < 0) + \sigma(s, h_{\tau^-} = -1, \cos\theta < 0) = \frac{8}{3}F_0(s) - 2F_1(s) \\
\sigma(s, h_{\tau^-} = +1) &= \sigma^F(s, h_{\tau^-} = +1) + \sigma^B(s, h_{\tau^-} = +1) = \frac{8}{3}(F_0(s) - F_2(s)) \\
\sigma(s, h_{\tau^-} = -1) &= \sigma^F(s, h_{\tau^-} = -1) + \sigma^B(s, h_{\tau^-} = -1) = \frac{8}{3}(F_0(s) + F_2(s)),
\end{aligned}
\tag{2.37}
$$

and the total cross section is given as:

$$
\sigma_{total} = \sum_{h_\tau} \int \frac{d\sigma}{d\cos\theta} d\cos\theta = \sigma^F(s) + \sigma^B(s) = \frac{16}{3}F_0(s). \tag{2.38}
$$

Combining equations (2.37) one can derive for the forward-backward asymmetry, A_{FB}:

$$A_{FB} = \frac{\sigma^F(s) - \sigma^B(s)}{\sigma_{total}} = \frac{3F_1(s)}{4F_0(s)}. \tag{2.39}$$

In the same way the polarization asymmetry P_τ:

$$P_\tau = \frac{\sigma(s, h_\tau = +1) - \sigma(s, h_\tau = -1)}{\sigma_{total}} = -\frac{F_2(s)}{F_0(s)}. \tag{2.40}$$

and the polarization asymmetry for each of the hemispheres:

$$\begin{aligned} P_\tau^F &= \frac{\sigma^F(s, h_\tau = +1) - \sigma^F(s, h_\tau = -1)}{\sigma^F(s)} = -\frac{4F_2(s) + 3F_3(s)}{4F_0(s) + 3F_1(s)}, \\ P_\tau^B &= \frac{\sigma^B(s, h_\tau = +1) - \sigma^B(s, h_\tau = -1)}{\sigma^B(s)} = -\frac{4F_2(s) - 3F_3(s)}{4F_0(s) - 3F_1(s)}. \end{aligned} \tag{2.41}$$

Using Eq. (2.41) the forward-backward polarization asymmetry is defined as:

$$\begin{aligned} A_{FB}^{pol} = &\frac{[\sigma^F(s, h_\tau = +1) - \sigma^F(s, h_\tau = -1)] - [\sigma^B(s, h_\tau = +1) - \sigma^B(s, h_\tau = -1)]}{\sigma_{total}} \\ &= -\frac{3F_3(s)}{4F_0(s)}. \end{aligned} \tag{2.42}$$

Utilizing the defined asymmetries the differential cross section for a given helicity state $h_\tau = \pm 1$ (2.35) can also be written as:

$$\frac{d\sigma}{dcos\theta}(s, h_\tau) = F_0(s)(1 + \cos^2\theta) + \frac{8}{3}A_{FB}(s)\cos\theta + h_\tau[P_\tau(s)(1 + \cos^2\theta) + \frac{8}{3}A_{FB}^{pol}(s)\cos\theta]. \tag{2.43}$$

The polarization asymmetry provides the determination of the weak mixing angle $\sin^2\theta_W$. Indeed, at the Z^0 pole the interference term in Eq. (2.36) vanishes and neglecting the QED term the expression for the τ polarization becomes:

$$P_\tau(s = M_Z^2) = -\frac{2v_\tau a_\tau}{v_\tau^2 + a_\tau^2} \approx -2 + 8\sin^2\theta_W. \tag{2.44}$$

As can be seen at the Z pole the τ polarization does not depend on the initial flavor. The information on the quark couplings can be accessed through A_{FB} and A_{FB}^{pol}, namely:

$$\begin{aligned} A_{FB}(s = M_Z^2) &\approx \frac{3}{4}A_q A_\tau, \\ A_{FB}^{pol}(s = M_Z^2) &\approx -\frac{3}{4}A_q. \end{aligned} \tag{2.45}$$

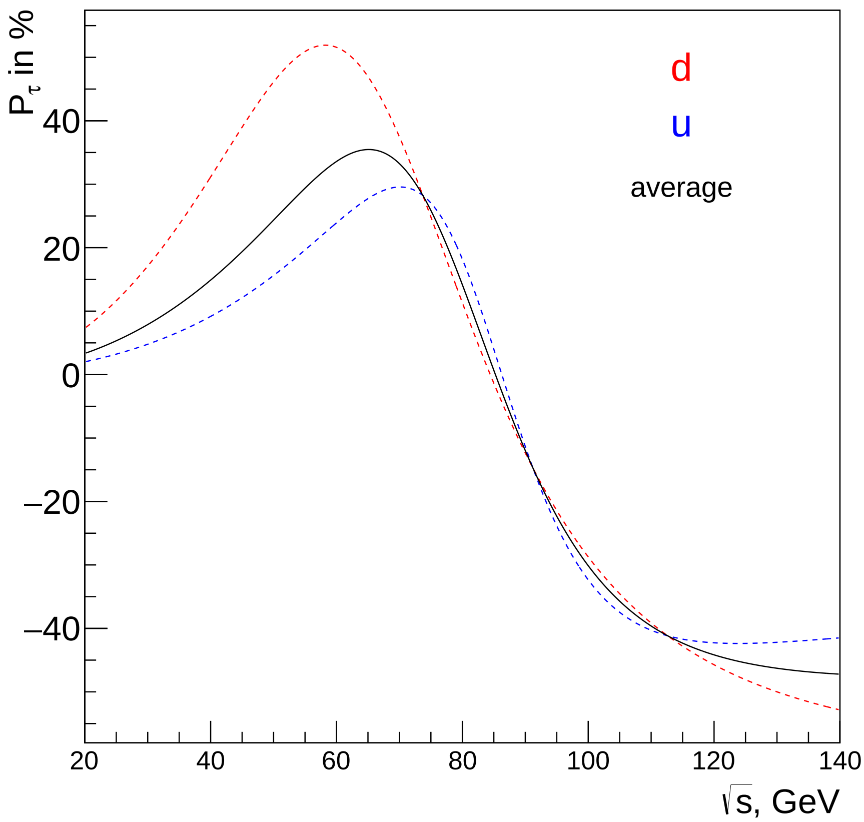

Figure 7: The τ polarization as a function of $\sqrt{s}$. *Dashed blue curve* polarization for $u\bar{u}$ in the initial state, *Dashed red curve* for $d\bar{d}$. *Solid curve* the average with the factor $\alpha_u = 0.423$ taken from Monte Carlo simulation. The parameters $m_Z = 91.1867 GeV$, $\Gamma_Z = 2.4939 GeV$, $\sin^2\theta_W = 0.23155$ are used in the tree-level calculation.

where $A_f = \frac{2v_f a_f}{v_f^2 + a_f^2}$. Inserting the value of $\sin^2\theta_W$ from previous measurements in Eq. (2.44) reveals that the charged leptons are produced with a polarization of about 15%, and, for example, b quarks are produced with a polarization of about 95%.

However, since τ pairs at LHC are produced from pp collisions the center-of-mass energy of the initial $q\bar{q}$ pair is not known. At e^+e^- collisions, for example at LEP, the center-of-mass energy can be set equal to M_Z, to perform measurements at the Z^0 pole. At LHC the invariant mass of the τ pair is distributed following $F_0(s)$, and the τ polarization P_τ depends on s. A measurement of P_τ for events in a certain mass band around M_Z results in an average P_τ. In addition, at the LHC due to the missing energy escaped with neutrinos, it is hard to reconstruct the center-of-mass energy of the τ pair, but possible when combining the whole available information of the event kinematic. This reconstruction is described in Chapter 8 .

The τ polarization as a function of $\sqrt{s}$ separately for $u\bar{u}$ and $d\bar{d}$ initials states and averaged over flavours using $\alpha_u = 0.423$ is shown in Fig. 7. All curves in Fig. 7 cross at the point $\sqrt{s} = M_Z$ which expresses the fact that at Z peak the polarization does not depend on the flavour of the initial state. However, moving away from the Z peak, the interference term in Eq. (2.36) introduces a difference between the flavours. To take this into account in the measurement, corrections will be applied to determine from the measured averaged over $\sqrt{s}$ polarization the value at the peak, $P_\tau(\sqrt{s} = M_Z)$.

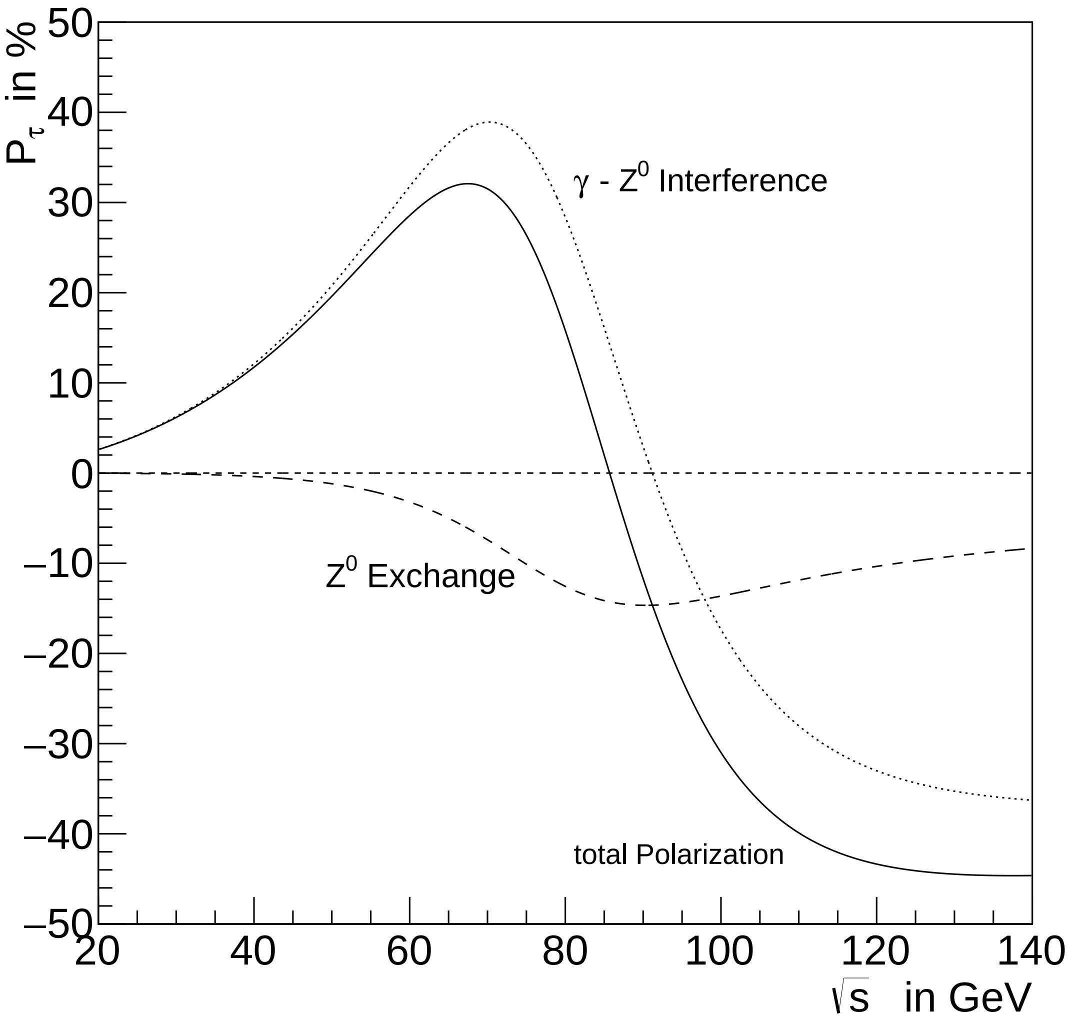

Figure 8: The averaged τ polarization as a function $\sqrt{s}$. *Solid line*: total polarization. *Dashed line*: pure Z^0 exchange. *Dotted line*: Z^0/γ interference. The parameters $m_Z = 91.1867 GeV$, $\Gamma_Z = 2.4939 GeV$, $\sin^2\theta_W = 0.23155$ are used for the tree-level calculation.

Fig. 8 shows the total polarization as a function of $\sqrt{s}$. The contributions from the Z^0 exchange and the $\gamma - Z^0$ interference are shown separately. The pure γ exchange does not create any polarization.

2.4 Radiative Corrections

So far only the tree-level equations were discussed. However, in the experiment one never measures tree-level quantities. In order to cover the full phenomenology one has to consider higher orders corrections, which can be grouped in two classes:

- QED corrections comprise diagrams with emission of a photon from initial or final state fermion, as shown in Fig. 9. The corrections are relatively large but calculated to a high precision. The initial state radiation changes the center-of-mass energy of incoming particles and significantly modifies the Z^0 lineshape. The effect of final state radiation is much smaller.
- Electroweak (EWK) corrections comprise the loop diagrams giving rise to modifications of the propagator, to vertex and box diagrams, as shown in Fig. 10. The corrections are smaller than those from QED, but introduce an additional fermion flavor dependence and $\sqrt{s}$ dependence of the coupling constants.

The corrections due to the box QED and EWK diagrams are not resonant at the Z peak and therefore their contribution is small.

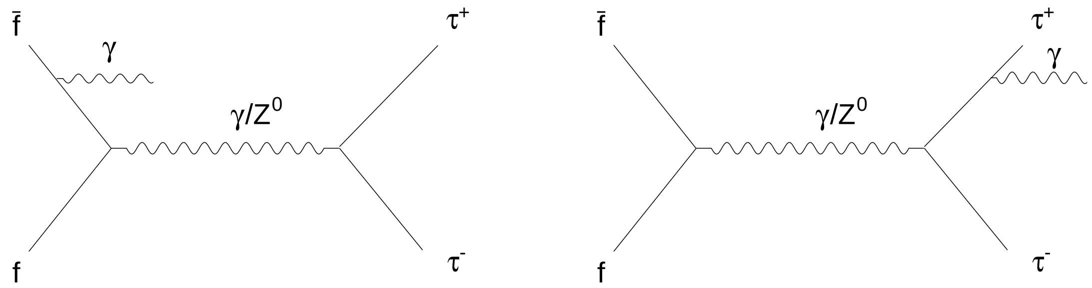

Figure 9: QED radiative corrections to the process $f\bar{f} \to \tau^+\tau^-$ due to the initial-state and final-state radiation.

They leave the qualitative form of Born approximation unchanged and can be accounted for by introducing the following modifications:

1. $\sqrt{s}$ dependence of the fine structure function

$$\alpha \to \alpha(s) = \frac{\alpha}{1 - \Delta\alpha(s)}, \tag{2.46}$$

2. $\sqrt{s}$ dependence of the Z boson propagator

$$\Gamma_Z \to \Gamma_Z = \Gamma_Z \frac{s}{M_Z^2}, \tag{2.47}$$

3. $\sqrt{s}$ dependence of *effective* vector and axial-vector coupling constants of the neutral currents

$$\begin{aligned} \bar{v}_f &= \sqrt{\rho_f(s)}(I_W^{3(f)} - 2Q_f k_f(s)\sin^2\theta_W), \\ \bar{a}_f &= \sqrt{\rho_f(s)} I_W^{3(f)}, \end{aligned} \tag{2.48}$$

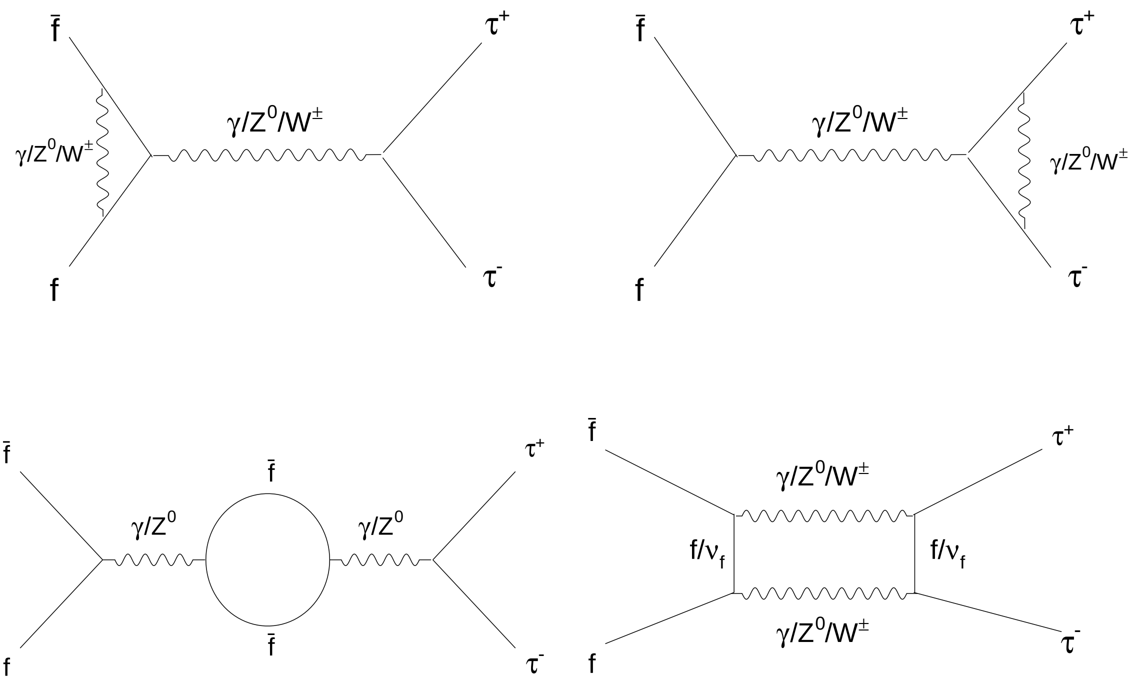

Figure 10: Electroweak corrections to the process $f\bar{f} \to \tau^+\tau^-$ due to vertex corrections, propagator corrections and box diagrams.

where $\sin^2\theta_W = 1 - \frac{M_W^2}{M_Z^2}$. The formfactors $\rho_f(s)$ and $k_f(s)$ depend on the fermion flavor and the renormalization scale ($\rho_f = k_f = 1$ at tree-level).

To connect the measurable quantities it is convenient to define the *effective* weak mixing angle for τ leptons as $\sin^2\theta^\tau_{eff} = k_\tau(M_Z)\sin^2\theta_W$. In terms of $\sin^2\theta^\tau_{eff}$ effective couplings constant $\bar{v}_\tau$ and $\bar{a}_\tau$ are given by $\sqrt{\rho_\tau(M_Z)}$ times their tree-level formulae, i.e.

$$\begin{aligned} \bar{a}_\tau &= -\frac{1}{2}\sqrt{\rho_\tau(s)} \\ \frac{\bar{v}_\tau}{\bar{a}_\tau} &= 1 - 4|Q_f|\sin^2\theta^\tau_{eff}. \end{aligned} \tag{2.49}$$

The value of the weak mixing angle measured in this analysis, hence, is quoted as the charged lepton [1] effective weak mixing angle $\sin^2\theta^\tau_{eff}$, determined by measurements of observables around the Z boson pole.

The effect of radiative correction on the τ polarization are calculated using ZFITTER [10] and shown in Fig. 11.

A comprehensive review of the electroweak radiative corrections in Z boson decays can be found in Ref. [11].

[1] Here lepton universality is assumed

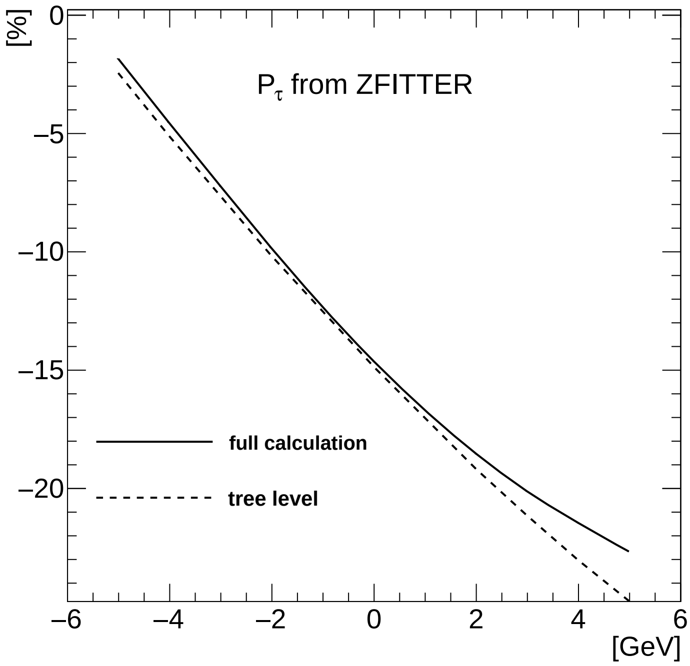

Figure 11: τ polarization as a function of center of mass energy relative to the Z^0 mass. *Dashed line*: tree level calculation; *Solid line*: full radiative corrections for the process $q\bar{q} \to Z^0 \to \tau\tau$.

Chapter 3

The Drell-Yan Process and Parton Distribution Functions

In Ref. [12] Drell and Yan noted that the parton model developed for the deep inelastic scattering can be extended to various processes, in particular to the production of lepton pairs in the high energy hadron-hadron collisions. A quark of one hadron and an antiquark of another hadron annihilate, producing a virtual photon or Z boson which then decays into a lepton pair as shown in Fig. 12. This is referred to as the Drell-Yan process.

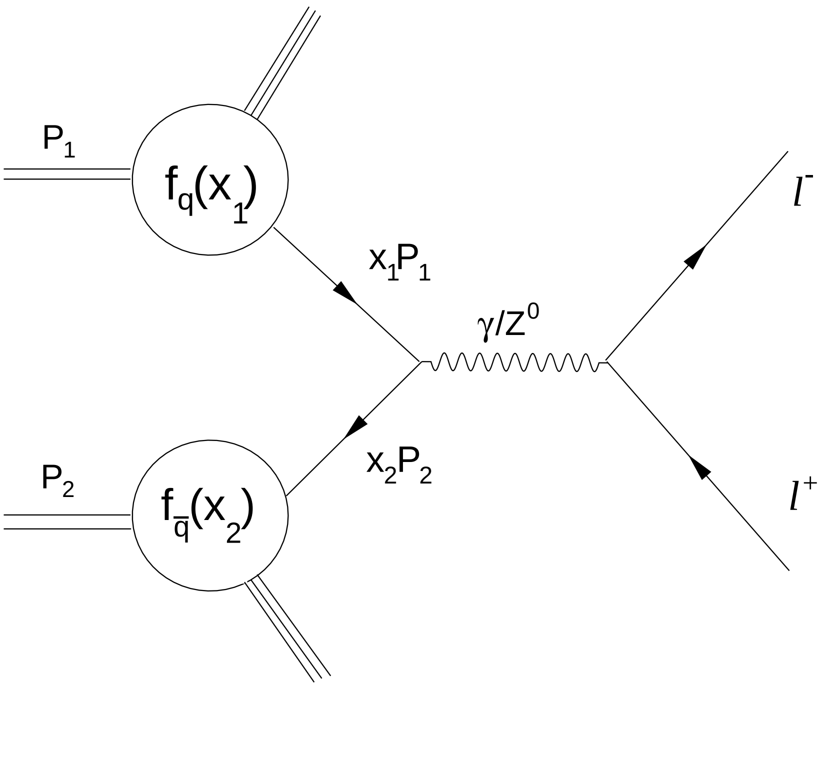

Figure 12: Production of a lepton pair in the Drell-Yan process.

The cross section of such a process is obtained by weighting the subprocess cross section $q\bar{q} \to l^+l^-$ with the *parton distribution functions* (PDF) $f_q(x)$ and $f_{\bar{q}}(x)$ obtained from deep inelastic scattering (DIS). The PDFs describe the probability density distribution of partons (quarks, antiquarks or gluons) as a function of x, the momentum fraction of a hadron carried by a parton.

The subprocess cross section to produce $\tau^+\tau^-$ pairs with a center-of-mass energy $\sqrt{s}$ from annihiliations of incoming quarks and antiquarks of flavor q with a collision energy $\sqrt{\hat{s}}$ is:

$$\frac{d\hat{\sigma}}{ds} = \sigma_q(s)\delta(s-\hat{s}), \tag{3.1}$$

where $\sigma_q(s)$ is taken from Eq. 2.38.

The four-momenta of the two partons in the center-of-mass system of the two hadrons are:

$$\begin{aligned} p_1 &= \frac{\sqrt{S}}{2}(x_1, 0, 0, \quad x_1), \\ p_2 &= \frac{\sqrt{S}}{2}(x_2, 0, 0, -x_2), \end{aligned} \tag{3.2}$$

where S is the square of the hadron-hadron collision energy. The square of $q\bar{q}$ collision energy is related to S by:

$$\hat{s} = (p_1 + p_2)^2 = x_1 x_2 S. \tag{3.3}$$

Using the above definitions the parton model cross section at leading order of α_S for the production of $\tau^+\tau^-$ pairs with the center-of-mass energy $\sqrt{s}$, for a quark flavor q, can be written as:

$$\begin{aligned} &\frac{d\sigma(s)}{ds} = \int_0^1 dx_1 dx_2 \left\{ f_q(x_1, s) f_{\bar{q}}(x_2, s) + (q \leftrightarrow \bar{q}) \right\} \frac{d\hat{\sigma}(s)}{ds} = \\ &\frac{\sigma_q(s)\kappa}{s} \int_0^1 dx_1 dx_2 \left\{ f_q(x_1, s) f_{\bar{q}}(x_2, s) + (q \leftrightarrow \bar{q}) \right\} \delta(x_1 x_2 - \kappa) = \frac{\sigma_q(s)}{s} \kappa \mathcal{F}(\kappa), \end{aligned} \tag{3.4}$$

where $\kappa = s/S$. The next-to-leading QCD orders can be written as perturbative expansion of $\mathcal{F}$ in powers of the strong coupling α_S

$$\mathcal{F}(\kappa) = \mathcal{F}_0(\kappa) + \frac{\alpha_S}{2\pi}\mathcal{F}_1(\kappa) + \dots. \tag{3.5}$$

There are three classes of contributions to $\mathcal{O}(\alpha_S)$: virtual gluon corrections, real gluon corrections and the quark-gluon scattering. The diagrams are shown in Fig. 56.

According to Eq. (3.5) the $\mathcal{O}(\alpha_S)$ corrections to the cross section (3.4) is:

$$\frac{d\sigma(s)}{ds} = \int_0^1 dx_1 dx_2 dz \delta(x_1 x_2 z - \kappa)$$
$$\times \left[\sum_q \frac{d\hat{\sigma}_q(s)}{ds} \left\{ f_q(x_1,s) f_{\bar{q}}(x_2,s) + (q \leftrightarrow \bar{q}) \right\} \left(\delta(1-z) + \frac{\alpha_S(s)}{2\pi} \Delta(z,x_1,x_2,s) \right) \right]. \tag{3.6}$$

An explicit form of the function $\Delta(z, x_1, x_2, s)$ can be found in Appendix E.

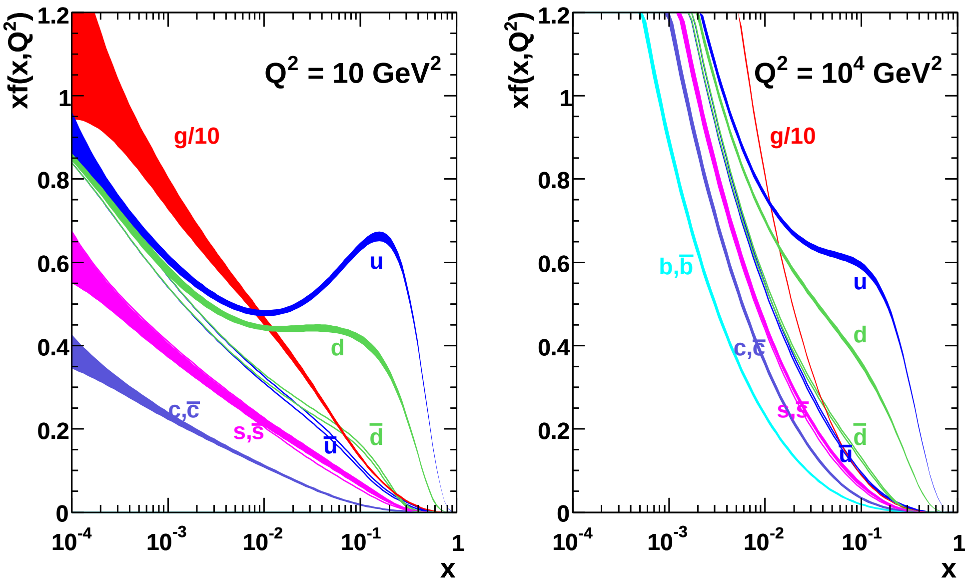

Figure 13: Distributions of x times the parton distributions $f(x)$ and their associated uncertainties using the NLO MSTW2008 parametrisation at a scale $Q^2 = 10$ GeV^2 and $Q^2 = 10,000$ GeV^2 .

The parton density functions f, used in this analysis to calculate the cross section (9.6) are provided by the MSTW08 [13] collaboration and are based on data from DIS, as well as results from the HERA and Tevatron colliders.

Chapter 4

The Tau Lepton

The idea of the possible existence of a heavy charged lepton has been raised after the muon discovery. Long before the discovery the signatures to be searched for a heavy lepton, including the hadronic decays of heavy lepton have been predicted by Tsai [14].

The clear evidence for the τ lepton was announced in 1975 by the MARK I group [15]. It was important to find a unique signature, being different from processes expected in the same mass region, e.g. from decays of charmed mesons. They presented 64 events identified as the process $e^+e^- \rightarrow e^\pm + \mu^\pm + \geq 2$ undetected particles in which no other charged particles or photons were detected.

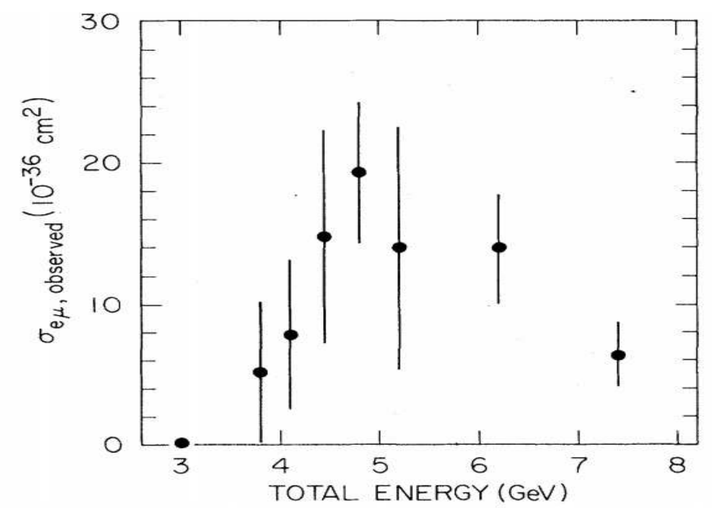

Figure 14: The cross section of the process $e^+e^- \rightarrow e^\pm + \mu^\pm + \geq 2$ undetected particles as a function of center-of-mass energy.

The observed cross section as a function of center-of-mass energy is shown in Fig. 14, from which the authors concluded:"the signature $e - \mu$ events can not be explained either by the production and decay of any presently known particles or as coming from any of the well-understood interactions which can conventionally lead to an e and a μ in the final state. A possible explanation for these events is the production and decay of a pair of new particles, each having a mass in the range of 1.6 to 2.0 GeV/c^2". Later the discovery of new lepton was confirmed by other experiments [16, 17].

4.1 The Mass

The τ lepton mass, m$_\tau$, is one of the fundamental parameter of the electroweak theory. However, the mass of τ, as well as the mass of two other charged leptons (e,μ), is not explained within the framework of the SM. It is interesting to note the large mass difference between leptons, the muon mass is approximately 210 times the electron mass, the tau is about 17 times heavier than the muon while the only fundamental difference between generations is the fact that they couple to their own neutrino. Many searches have been performed for heavier charged leptons that would belong to a fourth generation. So far up to a mass 1000 GeV, or about 56 times of the τ lepton mass, with negative results [18].

A precision measurement of m_τ is a proof of lepton universality. Lepton universality implies that the Fermi constant is flavor independent: $G_e = G_\mu = G_\tau = G_F$. Comparing the branching fractions of the τ and the μ into electron, lepton universality can be expressed as:

$$r = (\frac{G_\tau}{G_\mu})^2 = \frac{t_\mu}{t_\tau}(\frac{m_\mu}{m_\tau})^5 \frac{\mathcal{B}(\tau \to e\nu\bar{\nu})}{\mathcal{B}(\mu \to e\nu\bar{\nu})}(1+F_W)(1+F_\gamma), \tag{4.1}$$

where F_W and F_γ are the weak and electromagnetic radiative corrections and t_μ, t_τ the lifetime of the μ and τ, respectively.

Furthermore, the precision of m_τ also restricts the ultimate upper limit on the mass of the tau neutrino, m_{ν_τ}. The bound on m_{ν_τ} can be obtained by analysing the invariant mass spectrum of semileptonic τ decays. The present limit of $m_{\nu_\tau} < 18.2 MeV$ (95% C.L.) is based on the kinematics of the decay $\tau \to 2\pi^-\pi^+\nu_\tau$ and $\tau \to 3\pi^-2\pi^+\nu_\tau$ [19]. This method relies on a determination of the end point of the mass spectrum of the charged particle from the decay and thus requires the high precision of m_τ.

So far, the threshold scan method and the pseudo-mass technique have been used to determine the mass of τ lepton. The pseudo-mass method have been developed by the ARGUS [20] collaboration and allows to measure m_τ far above the production threshold. The method consist in analysing the invariant mass and energy of the hadronic system in the hadronic τ decays. The scanning method was used, for example, in KEDR [21] and is based on a study of the cross section of τ pair production in e^+e^- collisions near the center-of-mass energy threshold. The current averaged value for τ lepton mass is 1776.82 ± 0.16 MeV [18].

4.2 Spin of the τ

The spin of the τ has been determined by analysing the energy dependence of the production cross section near threshold. The cross section for $\tau\tau$ production in e^+e^- collisions near threshold is given by:

$$\sigma_{\tau\tau} = \sigma_{\mu\mu} F(\beta), \tag{4.2}$$

where $\sigma_{\mu\mu} = \frac{4\pi\alpha^2}{3s}$. $F(\beta)$ is a function accounting for threshold effects due to the τ mass, with $\beta = p_\tau / E_\tau$ the laboratory velocity of the τ. Consider spin $1/2$, $F(\beta)$ reads :

$$F(\beta) = \beta \frac{3-\beta^2}{2} \tag{4.3}$$

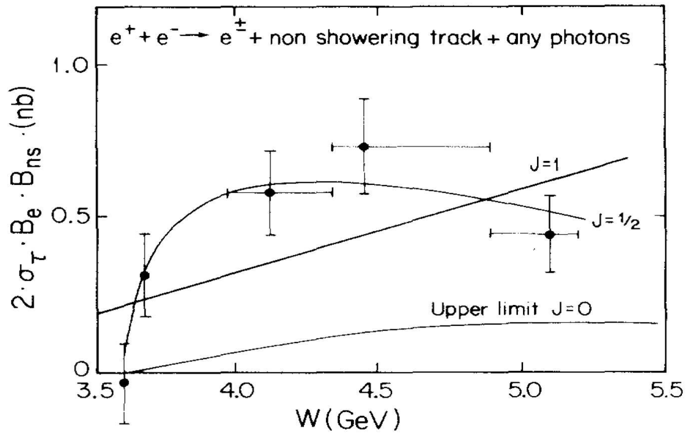

Figure 15: The energy dependence of the $\tau\tau$ cross section times decay branching fractions.

In Fig. 15 the energy dependence of the cross section obtained by DASP experiment [22] is shown. The curves represent different spin assignments.

As far as one can see the data is in good agreement for spin 1/2 and is inconsistent with spin 1 or 0.

4.3 The τ lepton lifetime

There are various methods used to measure the lifetime of the τ lepton. In this chapter the simplest method, the decay length (DL) method is described. The DL method can be applied to any three-prong τ decay and does not require to analyse the decay topology of $\tau^+\tau^-$ event, i.e. the decay of the second τ lepton.

The decay length of the τ is obtained from the secondary vertex (SV) reconstruction defined as the common point of origin of the three tracks from τ decay. The primary vertex (PV), the production point of τ lepton can be approximated by the center of the luminous region of the two colliding beams. The distance between PV and SV is the decay length. Fig. 16 shows the decay length distribution obtained by the OPAL Collaboration [23]. The distribution follows the exponential law, from which the lifetime can be extracted. The current value for the τ lepton lifetime is: $t_\tau = (290.3 \pm 0.5)$fs [18].

Other approaches to measure lifetime in different decay channels are described in Ref. [24].

4.4 The decays of τ lepton

In the following sections the τ decays to leptons and hadrons are discussed.

4.4.1 Leptonic decays

The leptonic τ decays to $\mu\nu\nu$ and $e\nu\nu$ can be straightforwardly calculated from the Feynman diagram shown in Fig. 17. The energy distribution of the charged leptons from τ lepton

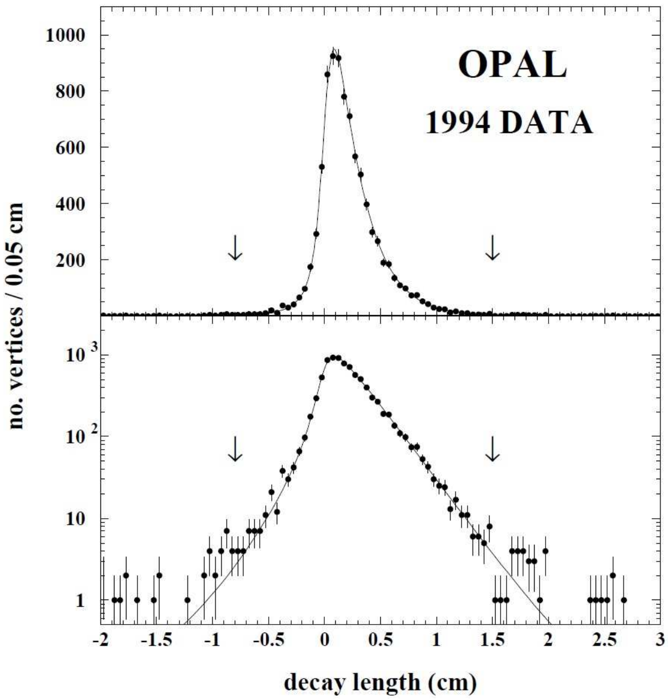

Figure 16: Decay length distribution from three-prong τ decays obtained by OPAL.

decays can be written in the rest frame of the τ as [14]:

$$\Gamma\left(\begin{array}{c}\tau^- \to \nu_\tau \bar{\nu}_l l^- \\ \tau^+ \to \bar{\nu}_\tau \nu_l l^+\end{array}\right) = \frac{G_F^2 m_\tau^5}{3\times 2^7\pi^4}\frac{8}{m_\tau^4}\int\limits_0^{p_{max}} p^2 dp \int d\Omega \Big[3m_\tau - 4E - \frac{2m_l^2}{E} + \frac{3m_l^2}{m_\tau} \mp (\mathbf{w}\cdot\hat{\mathbf{p}})\frac{p}{E}(4E - m_\tau - \frac{3m_l^2}{m_\tau})\Big]. \tag{4.4}$$

Here $\mathbf{w}$ is a polarization vector of the τ lepton, $\hat{\mathbf{p}}$ is a unit vector along the direction of the lepton, p the lepton momentum, $E = \sqrt{p^2 + m_l^2}$ and $p_{max} = \frac{m_\tau^2 - m_l^2}{2m_l}$.

Neglecting the mass of the lepton Eq. (4.4) can be simplified into:

$$\Gamma\left(\begin{array}{c}\tau^- \to \nu_\tau \bar{\nu}_l l^- \\ \tau^+ \to \bar{\nu}_\tau \nu_l l^+\end{array}\right) = \frac{G^2 m_\tau^5}{3\times 2^7\pi^4}\int d\Omega_l \int\limits_0^1 dx x^2[3 - 2x \mp \mathbf{w}\cdot\hat{\mathbf{p}}(2x-1)], \tag{4.5}$$

where $x = E/E_{max}$ with $E_{max} = m_\tau/2$.

Some qualitative features of the τ decay to leptons can be understood from the Eq. (4.5). If one considers l^- with nearly maximum energy ($x \approx 1$) then both neutrinos must be emitted in the direction opposite to that of the lepton. Noting that helicities of ν and $\bar{\nu}$ are of opposite sign, the angular momentum carried by neutrinos is zero. Consequently, the lepton l must be emitted with spin parallel to that of the τ.

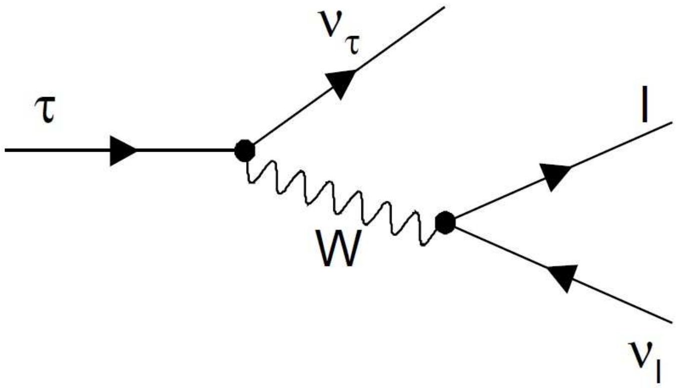

Figure 17: Feynman diagram for a leptonic τ decay.

For the case $x << 1$ the ν and $\bar{\nu}$ move in opposite directions with the total spin equal to unity and conservation of angular momentum requires that, the lepton is emitted along the τ spin direction.

Integration of (4.4), ignoring the mass of the final lepton and averaging over τ spin states, gives well know relation for the total decay width:

$$\Gamma_0 = \frac{G_F^2 m_\tau^5}{192\pi^3}. \tag{4.6}$$

Integrating of (4.4) without neglecting the mass of the lepton one obtains:

$$\Gamma\left(\begin{array}{c}\tau^- \to \nu_\tau \bar{\nu}_l l^- \\ \tau^+ \to \bar{\nu}_\tau \nu_l l^+\end{array}\right) = \Gamma_0(1 - 8\lambda + 8\lambda^3 - \lambda^4 - 12\lambda^2 \ln \lambda) \tag{4.7}$$

where $\lambda = \frac{m_l^2}{m_\tau^2}$. The difference between the masses of the electron and the muon introduces a difference in the τ decay rates. The ratio can be expressed as:

$$\frac{\Gamma(\tau^- \to \nu_\tau \bar{\nu}_\mu \mu^-)}{\Gamma(\tau^- \to \nu_\tau \bar{\nu}_e e^-)} = \frac{1 - 8y + \ldots}{1 - 8x + \ldots} \approx 0.973, \tag{4.8}$$

where $y = \frac{m_\mu^2}{m_\tau^2}$ and $x = \frac{m_e^2}{m_\tau^2}$. The branching fraction for the leptonic decays are defined as:

$$\mathcal{B}(\tau \to l\nu_\tau \bar{\nu}_l) = \frac{\Gamma(\tau \to l\nu_\tau \bar{\nu}_l)}{\Gamma_{tot}} = t_\tau \Gamma(\tau \to l\nu_\tau \bar{\nu}_l). \tag{4.9}$$

From the Eq. (4.6), (4.8) and with the current value of lifetime $t_\tau = (290.3 \pm 0.5) fs$ one gets the following numerical predictions for the branching fractions:

$$\begin{aligned}\mathcal{B}(\tau \to e\nu_\tau \bar{\nu}_e) &= (17.851 \pm 0.030)\% \\ \mathcal{B}(\tau \to \mu\nu_\tau \bar{\nu}_\mu) &= (17.352 \pm 0.029)\%,\end{aligned} \tag{4.10}$$

which perfectly agree with the measurements: [18].

$$\begin{aligned} \mathcal{B}(\tau \to e\nu_\tau\bar{\nu}_e) &= (17.85 \pm 0.05)\%, \\ \mathcal{B}(\tau \to \mu\nu_\tau\bar{\nu}_\mu) &= (17.36 \pm 0.05)\%. \end{aligned} \tag{4.11}$$

4.4.2 Hadronic decays

Unlike for the electron and the muon, the τ lepton has enough mass to decay into hadrons. Since the mass of the τ lepton is below that of the charmed mesons, the hadronic τ decay channels include only decay into non-strange and strange mesons. In general the matrix element for hadronic τ decay can be written as:

$$M = \frac{G_F}{\sqrt{2}} L^\mu H_\mu. \tag{4.12}$$

The leptonic current L^μ has the standard left-handed form. Noting that the final hadron system can have spin either 0 or 1 there are two options for H_μ:

$$\begin{aligned} H_\mu^{J=0} &= f_0(q^2) q_\mu, \\ H_\mu^{J=1} &= f_1(q^2) \epsilon_\mu. \end{aligned} \tag{4.13}$$

Here the scalar current is proportional to the Lorentz vector of the hadronic system and the vector part to the polarization vector of the spin-1 particle. In the vector part the term proportional to q_μ is absent due to the requirement that the polarization vector has to be orthogonal to q_μ ($q_\mu \epsilon^\mu = 0$). The coefficients f_0 and f_1 are scalar function and depend on q^2.

With these currents an elegant and general form for the hadronic τ decays can be derived as [14]:

$$\begin{aligned} &\Gamma(\tau^- \to hadrons + \nu_\tau) = \frac{G_F^2 m_\tau^3}{32\pi^2} \int_0^{m_\tau^2} dq^2 (m_\tau^2 - q^2)^2 \times \\ &\left[cos^2\theta_C \left[(m_\tau^2 + 2q^2)(v_1(q^2) + a_1(q^2)) + m_\tau^2 a_0(q^2) \right] + \right. \\ &\left. sin^2\theta_C \left[(m_\tau^2 + 2q^2)(v_1^s(q^2) + a_1^s(q^2)) + m_\tau^2 (v_0^s(q^2) + a_0^s(q^2)) \right] \right], \end{aligned} \tag{4.14}$$

where v and a are the vector and axial spectral functions and θ_C is the Cabibbo angle. Each spectral function is responsible for a final state having particular quantum numbers. The lower index labels the spin of the final state, and the upper the strangeness. The $J = 1$ state is associated with v_1, a_1, v_1^s and a_1^s, while a_0, v_0^s, a_0^s are describing the $J = 0$ state. The quantum numbers, spectral functions and the corresponding decays are summarized in Table. 4.1.

Table 4.1: Spectral functions of the hadronic τ decays

Spectral function	J^P	Strangeness	Possible final state
v_0	0^+	0	–
v_1	1^-	0	$\rho(770)$, $\rho'(1450)$, $\rho''(1700)$, (2π),(4π)
a_1, a_0	$1^+, 0^-$	0	π^-, $a_1(1260)$, $(3\pi)^-$
v_1^s, v_0^s	$1^-, 0^+$	-1	$K^*(892)$, $(K\pi)^-$
a_1^s, a_0^s	$1^+, 0^-$	-1	K^-, $K_1(1270)$, $K_1(1400)$, $K\pi\pi$, $KK\pi$

Equation (4.14) precisely describes hadronic τ decays depending only on unknown spectral functions which can not be determined in theory and have to be taken from experiment. However, there are several theoretical restrictions on the spectral functions. The conservation of vector current CVC is arising from isotopic properties of the vector current. The weak non-strange vector current and the isovector electromagnetic current are in the same isotopic multiplet and thus the first must be conserved in analogy to electromagnetic current. Specifically it means that

$$\partial_\mu < 0|V_\mu|had >= 0, \tag{4.15}$$

where V_μ is a vector current. It can be shown that relation 4.15 can be fulfilled only if there is no scalar ($J^P = 0^+$) in the final states [25, 26].

Also the CVC theorem relates the vector part of the non-strange weak current to the isovector part of electromagnetic current [27], which gives the prediction on v_1

$$v_1(q^2) = \frac{q^2\sigma_{I=1}(e^+e^- \to hadrons)}{4\pi\alpha^2}, \tag{4.16}$$

where $\sigma_{I=1}(e^+e^- \to hadrons)$ is the total cross section for e^+e^- annihilation into hadrons with quantum numbers $I^G = 1^+$ (G - parity combines C parity and isospin rotation). Thereby, CVC predicts the rate for τ decays into vector mesons, (e.g. $\tau \to \rho(770)\nu$ and $\tau \to \rho'(1450)\nu$) from measurements of $\sigma(e^+e^- \to$ hadrons)..

4.4.2.1 Pseudoscalar decays

Using Eq. (4.14), the decay widths for $\tau \to \pi\nu$ with the corresponding spectral function (**??**) reads:

$$\Gamma(\tau \to \pi\nu) = \frac{G_F f_\pi^2 cos^2\theta_C}{16\pi} m_\tau^3 (1 - \frac{m_\pi^2}{m_\tau^2})^2. \tag{4.17}$$

The decay constant $f_\pi cos\theta_C$, describing the strength of the pion coupling to the axial-vector current, is not predicted in theory and must be taken from experiment. For example, this quantity can be obtained from the well measured pion decay to muon, $\pi \to \mu\nu$, as shown in Fig. 18.

The decay rate for this channel is:

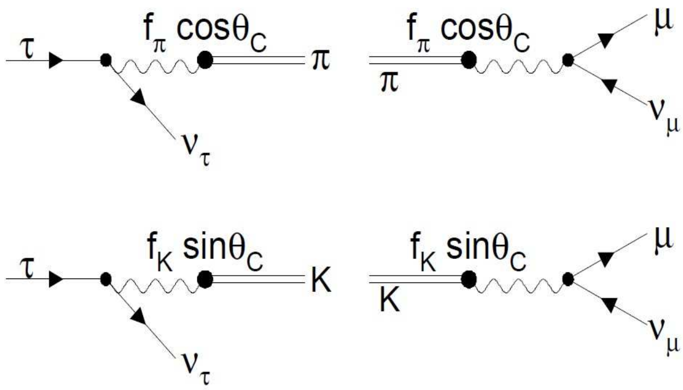

Figure 18: Diagrams for the decays $\tau \to \pi(K)\nu$ and $\pi(K) \to \mu\nu$.

$$\Gamma(\pi \to \mu\nu) = \frac{G_F f_\pi^2 cos^2\theta_C}{8\pi} m_\mu^2 m_\pi (1 - \frac{m_\mu^2}{m_\pi^2})^2, \tag{4.18}$$

Consequently the relation between the branching fractions for these two decays is:

$$\mathcal{B}(\tau \to \pi\nu) = \frac{m_\tau^3(1 - m_\pi^2/m_\tau^2)}{2m_\pi m_\mu^2(1 - m_\mu^2/m_\pi^2)} \frac{\tau_\tau}{\tau_\pi} \mathcal{B}(\pi \to \mu\nu). \tag{4.19}$$

The decay $\tau \to K\nu$ can be treated with the replacement $f_\pi \to f_K$ and $cos\theta_C \to sin\theta_C$.

The prediction for $\mathcal{B}(\tau \to \pi\nu)$ using the above equation is in a good agreement with the measured values [18]:

$$\begin{aligned} \mathcal{B}(\tau \to \pi\nu)_{prediction} &= (10.86 \pm 0.05)\% \\ \mathcal{B}(\tau \to \pi\nu)_{measurement} &= (10.83 \pm 0.06)\%. \end{aligned} \tag{4.20}$$

$$\begin{aligned} \mathcal{B}(\tau \to K\nu)_{prediction} &= (7.09 \pm 0.04) \times 10^{-3} \\ \mathcal{B}(\tau \to K\nu)_{measurement} &= (7.00 \pm 0.01) \times 10^{-3}. \end{aligned} \tag{4.21}$$

4.4.2.2 Multi pion decays

The situation with multi pion decays is somewhat more complicated, due to non-zero width of the final states and the presence of different spin states that have to be summed up.

The decay $\tau \to \pi\pi\nu$ does not suffer from any kind of suppression and thus has the largest branching fraction. The decay is going through the $\rho(770)$ resonance with a small contribution from $\rho'(1450)$ and $\rho''(1700)$. The decay width can be reasonably well estimated by invoking CVC. From (4.16) one can derive the quantitative relation:

$$\Gamma(\tau \to had\nu_\tau) = \frac{cos^2\theta_C G_F^2 m_\tau^3}{128\pi^4\alpha^2} \int_0^{m_\tau^2} sds(1-\frac{s}{m_\tau^2})^2(1+2\frac{s}{m_\tau^2})\sigma^{I=1}_{e^+e^-\to had}(s). \quad (4.22)$$

The CVC theorem can be applied to the various decay channels with even G-parity. Table 4.2 shows the comparison between measurements and predictions from CVC. All presented decays show reasonable agreement.

Table 4.2: Comparison of branching fractions obtained using CVC [28] [29] and experimentally measured values

Decay	Prediction, %	Measurement, %
$\pi^-\pi^0$	24.9 ± 0.07	25.52 ± 0.09
$\pi^-3\pi^0$	1.08 ± 0.05	1.19 ± 0.07
$2\pi^-\pi^+\pi^0$	4.20 ± 0.29	4.48 ± 0.06
$\eta\pi^-\pi^0$	0.155 ± 0.017	0.139 ± 0.001

The τ lepton decay to three pions is dominated by the a_1 resonance. There are two possible final states with equal probabilities, $\pi^-\pi^-\pi^+$ and $\pi^-\pi^0\pi^0$. From the Weinberg sum rules [30] it can be shown that $f_{a_1} = f_\rho$ and therefore:

$$\frac{\Gamma(\tau \to a_1\nu_\tau)}{\Gamma(\tau \to \rho\nu_\tau)} = \frac{(m_\tau^2 + m_{a_1}^2)^2(m_\tau^2 + 2m_{a_1}^2)}{(m_\tau^2 + m_\rho^2)^2(m_\tau^2 + 2m_\rho^2)}, \quad (4.23)$$

which gives for the branching fraction $\mathcal{B}(\tau \to a_1\nu) = (13.94 \pm 0.9)\%$ while the measured value is $(18.41 \pm 0.12)\%$. The reason for this discrepancy is that this approach does not take into account the finite width of the a_1 meson. In more details this decay channel will be discussed in chapter 5.3.

A comprehensive description of hadronic τ decays can be found in Ref. [31]. Fig. 19 shows the summary on the branching fractions classified by different categories.

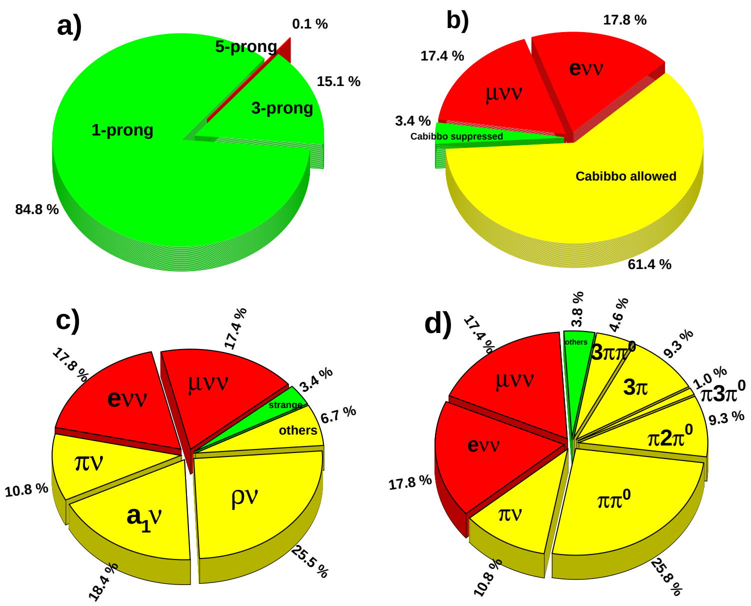

Figure 19: Summary of the τ lepton branching fractions. a) By number of prongs. b) Hadronic and Leptonic decays. c) The major resonances. d) Main exclusive decay channels.

Chapter 5

Polarization observables

The helicity state of a τ lepton is not a directly measurable quantity in the CMS experiment. However, it can be extracted by analyzing the τ decay products. In Chapter 2.3 the polarization is defined in terms of $\tau - Z^0$ couplings. Using the decay spectra as polarization analyzer the product ξP_τ is measured, where ξ is the chirality parameter:

$$\xi = \frac{2v_\tau^{CC} a_\tau^{CC}}{(v_\tau^{CC})^2 + (a_\tau^{CC})^2}, \tag{5.1}$$

where v_τ^{CC} and a_τ^{CC} are the vector and axial vector charged current couplings. If the maximal parity violation of the charged weak current is assumed then $\xi = -1$.

Due to helicity conservation the τ^+ and the τ^- produced in Z decays have to a good approximation at high energy have opposite helicities. Since the τ leptons have opposite charge and opposite helicity, CP conservation requires their decay distribution to be the same. The decay distributions of τ leptons from Z decay for a given helicity state does not depend on the τ charge.

In this chapter the spin sensitive variables in the decay $\tau \to a_1 \nu$ are considered.

5.1 Polarization in the decay $\tau^- \longrightarrow a_1\nu$

In the $\tau^- \to a_1\nu$ information on the τ lepton helicity state can be extracted from the angular distributions of the τ decay products. The first quantity to consider is the angle θ^* between the direction of flight of the τ^- in the laboratory frame and the direction of the a_1 as seen from the τ rest frame. Its cosine can be written as:

$$\cos\theta^* = \frac{(\vec{n}_\tau \vec{p}^{\,*}_{a_1})}{|\vec{p}^{\,*}_{a_1}|}, \tag{5.2}$$

where $\vec{n}_\tau$ is the vector pointing along the τ direction and $\vec{p}_{a_1}$ the momentum of the a_1 in the τ rest frame. Conservation of angular momentum allows the a_1 to have helicity λ_{a_1} = 0 or λ_{a_1} = -1. The four helicity configurations of a_1 and τ with non-zero amplitude are schematically shown in Fig. 20.

The amplitudes with the a_1 spin perpendicular to its flight direction (longitudinal a_1, $\lambda_{a_1} = 0$) are more sensitive to the τ helicity h_τ, while the amplitudes with the a_1 spin parallel to its

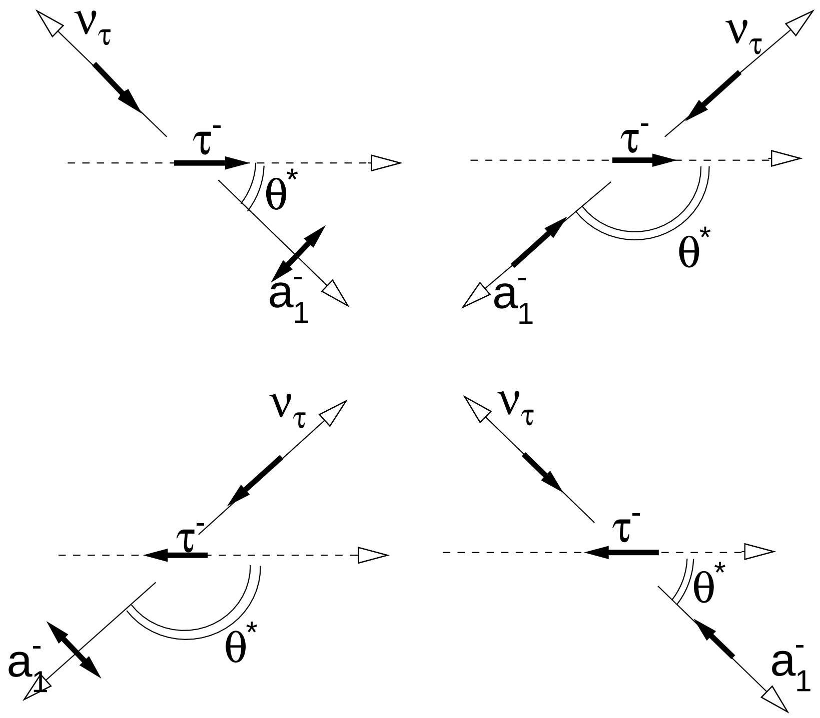

Figure 20: Definition of angle θ^* in the decay $\tau \to a_1\nu$. Open arrows indicate the flight direction of the particle, the solid arrow the spin.

flight direction (transverse a_1, $\lambda_{a_1} = -1$) washes this information out. The longitudinal and transverse amplitudes for a τ helicity h_τ are derived in Appendix B to be:

$$\begin{aligned} |M_{T,h_\tau}|^2 &\propto\ 2(1 - h\cos\theta^*), \\ |M_{L,h_\tau}|^2 &\propto\ \frac{m_\tau^2}{m_{a_1}^2}(1 + h\cos\theta^*). \end{aligned} \tag{5.3}$$

From Eq. (5.3) the relative strength of T and L amplitudes is:

$$\frac{|M_T|}{|M_L|} = \frac{\sqrt{2}m_{a_1}}{m_\tau}. \tag{5.4}$$

Combining the spin amplitudes for all possible configuration of a_1 and τ helicities, one gets:

$$\frac{1}{\Gamma}\frac{d\Gamma}{d\cos\theta^*} \propto 1 + \alpha_{a_1} h_\tau \cos\theta^*, \tag{5.5}$$

where the dilution factor $\alpha_{a_1} = \frac{|M_L|^2 - |M_T|^2}{|M_T|^2 + |M_L|^2} = \frac{m_\tau^2 - 2m_{a_1}^2}{m_\tau^2 + 2m_{a_1}^2} \approx 0.021$ is a result of the presence of the transverse a_1 amplitude. The value of the factor α characterizes the sensitivity of the $\cos\theta^*$ observable. Fore comparison, in the τ decay to ρ, $\alpha_\rho = 0.46$ and in the pion decay $\alpha_\pi = 1$.

Consequently, the sensitivity to the τ helicity in the decay $\tau^- \rightarrow a_1^- \nu$ is strongly reduced if only the $\cos\theta^*$ angle is analyzed.

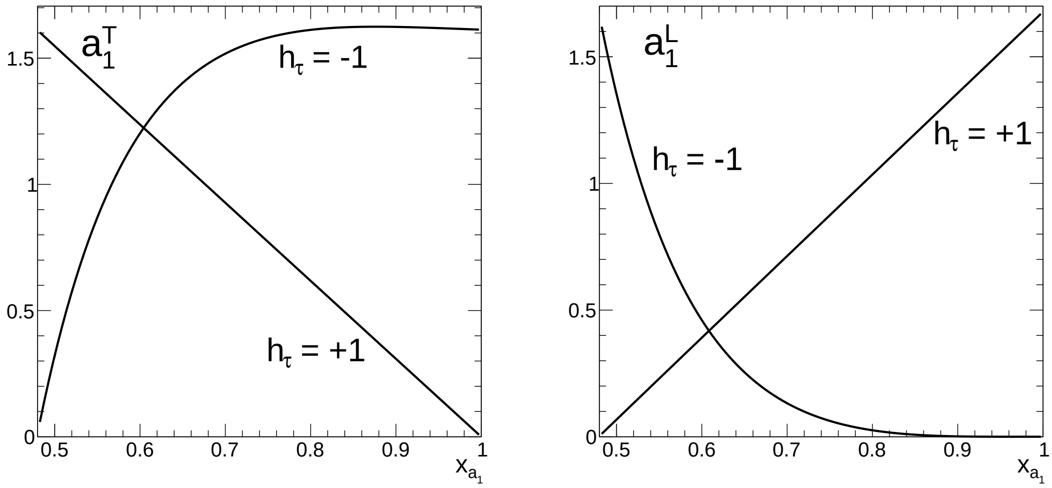

Figure 21: The spectrum of a_1 in the decay $\tau \rightarrow a_1\nu$ in the quantity $x_{a_1} = E_{a_1}/E_\tau$; $h_\tau = +1$ corresponds to 100% positive τ polarization, $h_\tau = -1$ to negative polarization. *Left plot*: transverse a_1. *Right plot*: longitudinal a_1.

The angle θ^* (5.2) can be expressed in terms of the a_1 and τ energy in the laboratory frame, E_{a_1} and E_τ [1]:

$$cos\theta^* = \frac{x_{a_1} m_\tau^2 - m_\tau^2 - Q^2}{(m_\tau^2 - Q^2)\sqrt{1 - m_\tau^2/E_\tau}}, \tag{5.6}$$

where $x_{a1} = E_{a_1}/E_\tau$, Q^2 is the mass of hadronic system. The spectrum for x_{a_1} is shown in Fig. 21 and is derived in Appendix C.

The loss of sensitivity due to factor α_{a_1} can be compensated if it is distinguished whether the a_1 meson is in a transverse or longitudinal state. The spin of the a_1 meson is transformed into the orbital angular momentum of the decay products and thus can be retrieved by analyzing the subsequent decay $a_1^- \rightarrow \pi^-\pi^-\pi^+$. The angle β is the angle between the normal to the 3π plane in the a_1 rest frame and the direction of a_1 in the laboratory frame, and an angle γ that describes the relative orientation of the pions in their decay plane. Both angles are shown in Fig. 22 for illustration. Quantitatively these angles can be defined as:

$$\begin{aligned} \cos\beta &= \vec{n}_\perp \vec{n}_{a_1} \\ \sin\gamma &= \frac{(\vec{n}_\perp \times \vec{n}_{a_1})\vec{q}_3}{|\vec{n}_\perp \times \vec{n}_{a_1}|} \end{aligned} \tag{5.7}$$

where $\vec{n}_{a_1}$ denotes direction of the a_1 in the laboratory frame, $\vec{n}_\perp$ the normal to the 3π plane in the a_1 rest frame, and $\vec{q}_3 = \vec{p}_3/|\vec{p}_3|$ the unit vector along the direction of the π^+ (π^-) if the final state is $\pi^-\pi^-\pi^+$ ($\pi^+\pi^+\pi^-$).

[1] Boosting Eq. (5.2) into the laboratory frame with $\gamma_\tau = E_\tau/m_\tau, \beta \approx 1$

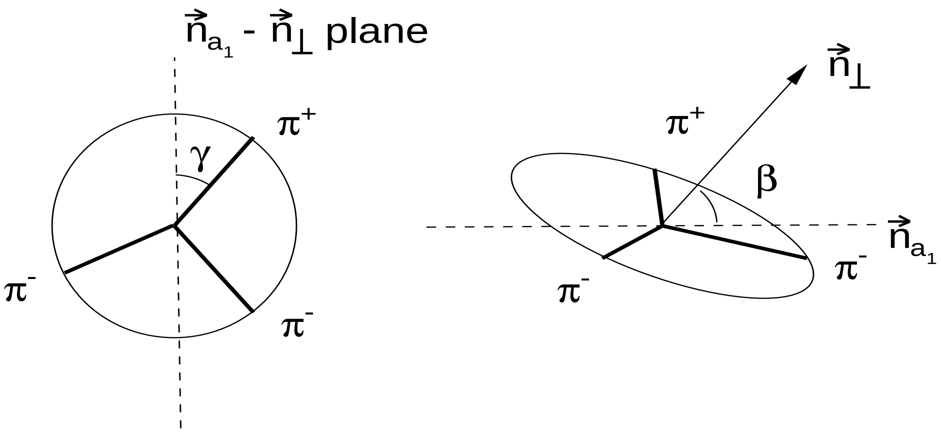

Figure 22: Definitions of angles β (*right*) and γ (*left*) in the a_1 rest frame. $\vec{n}_\perp$ defines the 3π plane in the a_1 rest frame, and $\vec{n}_{a_1}$ the direction of the laboratory frame.

The vector $\vec{n}_\perp$ coincides with the direction of the spin of the a_1 meson. If a_1 is in a longitudinally polarized state the pions plane tends to be parallel to $\vec{n}_{a_1}$, i.e. β is large, and, oppositely, the angle β is small if a_1 is transversely polarized.

Similarly to the angle θ^* the angles β and γ can be expressed in terms of quantities measured in the laboratory frame by boosting Eq. (5.7):

$$cos\beta = \frac{\vec{p}_3(\vec{p}_1 \times \vec{p}_2)}{|\vec{p}_{3\pi}|T}, \tag{5.8}$$

where

$$\begin{aligned}
&T = \frac{1}{2}\sqrt{-\lambda(B_1, B_2, B_3)},\\
&\lambda(B_1, B_2, B_3) = B_1^2 + B_2^2 + B_3^2 - 2B_1B_2 - 2B_1B_3 - 2B_2B_3,\\
&B_i = \frac{(E_iE_{3\pi} - \vec{p}_{3\pi}\vec{p}_i)^2 - Q^2m_\pi^2}{Q^2}.
\end{aligned}$$

$\vec{p}_i$ is the laboratory momentum of pion i, m_{ij} the invariant mass of pions i and j and Q the invariant mass of the three pions.

The decay distributions for the angles β and θ for a $J^P = 1^+$ system are [32]:

$$W(\cos\theta, \cos\beta) = \frac{3}{4(m_\tau^2 + 2m_{a_1}^2)}[(1+h_\tau)W^+(\cos\theta, \cos\beta) + (1-h_\tau)W^-(\cos\theta, \cos\beta)]. \tag{5.9}$$

$$
\begin{aligned}
W^+ =& \Big\{ \sin^2\beta \Big[m_\tau \cos\eta \cos\frac{\theta}{2} + m_{a_1} \sin\eta \sin\frac{\theta}{2} \Big]^2 \\
&+ \frac{1+\cos^2\beta}{2} \Big[\Big(m_\tau \sin\eta \cos\frac{\theta}{2} - m_{a_1} \cos\eta \sin\frac{\theta}{2} \Big)^2 + m_{a_1}^2 \sin^2\frac{\theta}{2} \Big] \Big\}, \\
W^- =& \Big\{ \sin^2\beta \Big[m_\tau \cos\eta \sin\frac{\theta}{2} - m_{a_1} \sin\eta \cos\frac{\theta}{2} \Big]^2 \\
&+ \frac{1+\cos^2\beta}{2} \Big[\Big(m_\tau \sin\eta \sin\frac{\theta}{2} + m_{a_1} \cos\eta \cos\frac{\theta}{2} \Big)^2 + m_{a_1}^2 \cos^2\frac{\theta}{2} \Big] \Big\}, \\
\cos\eta =& \frac{x_V(m^2 + M_V^2) - 2M_V^2}{(m^2 - M_V^2)\sqrt{x_V^2 - M_V^2/E_\tau}}.
\end{aligned}
\tag{5.10}
$$

The functions W^+ and W^- are the decay angular distributions for 100% $h_\tau = +1$ and 100% $h_\tau = -1$ state and plotted in Fig. 23. The same distributions are obtained using CMS Monte Carlo simulation of the process $q\bar{q} \to Z^0 \to \tau\tau$, as shown in Fig. 24.

The angle γ also carries information about the a_1 polarization. This can be understood by considering that the three pion system in the a_1 decay is produced through an intermediate $\pi\rho$ system. If the $\pi\rho$ system is produced in S-wave then the spin of a_1 is transferred to spin of the ρ and can be extracted by analyzing the angle between the one pion from ρ decay with respect to the other two. However, the presence of a D-wave $\pi\rho$ system, not large, though, makes the situation more complex, compared to the angle β, and consequently the angle γ contains less information than β.

The τ polarization can be obtained from data by analyzing and comparing angular distributions for θ^*, β and γ to Monte Carlo simulations of these distributions for $h_\tau = 1$ and $h_\tau = -1$. However, the analysis of multidimensional distributions is not practical and requires large statistics. A method to reduce the problem of a multi-dimensional fitting to an one-dimensional is described in the next chapter.

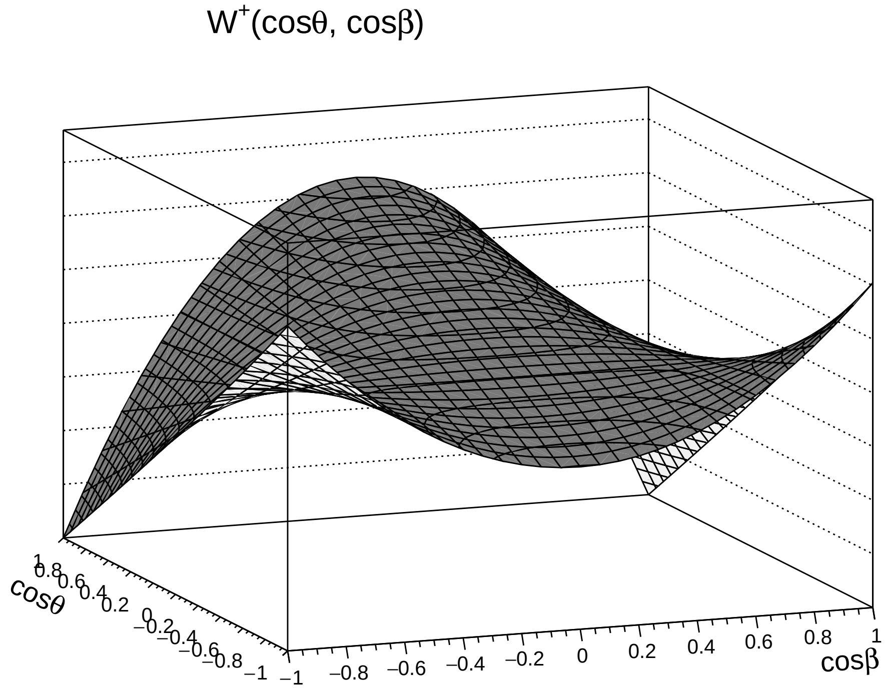

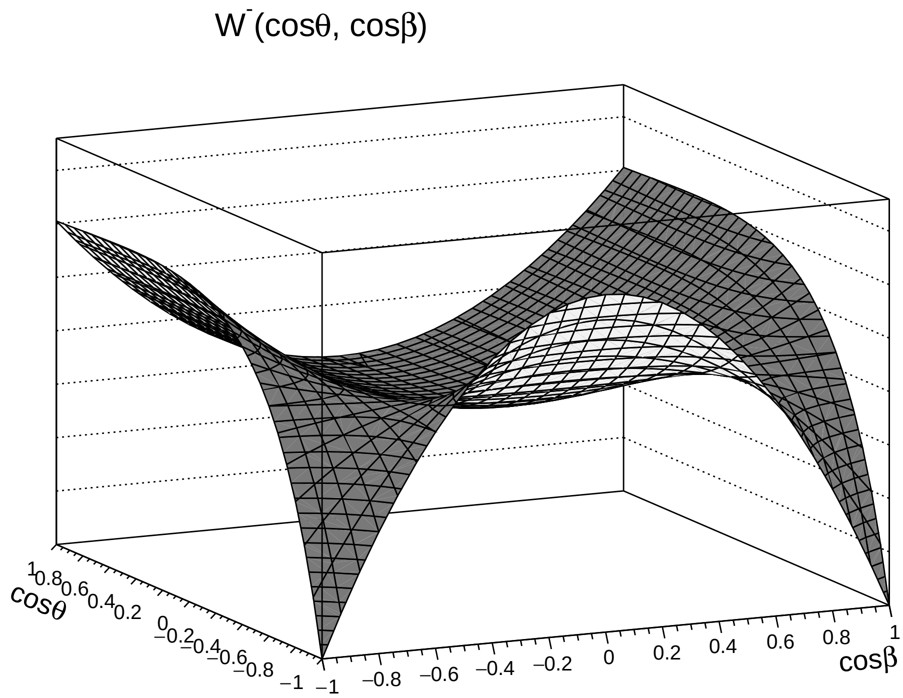

Figure 23: Distributions of the angles θ and β for the decay $\tau \to a_1\nu$; *Upper plot*: $h_\tau = +1$; *Lower plot*: $h_\tau = -1$.

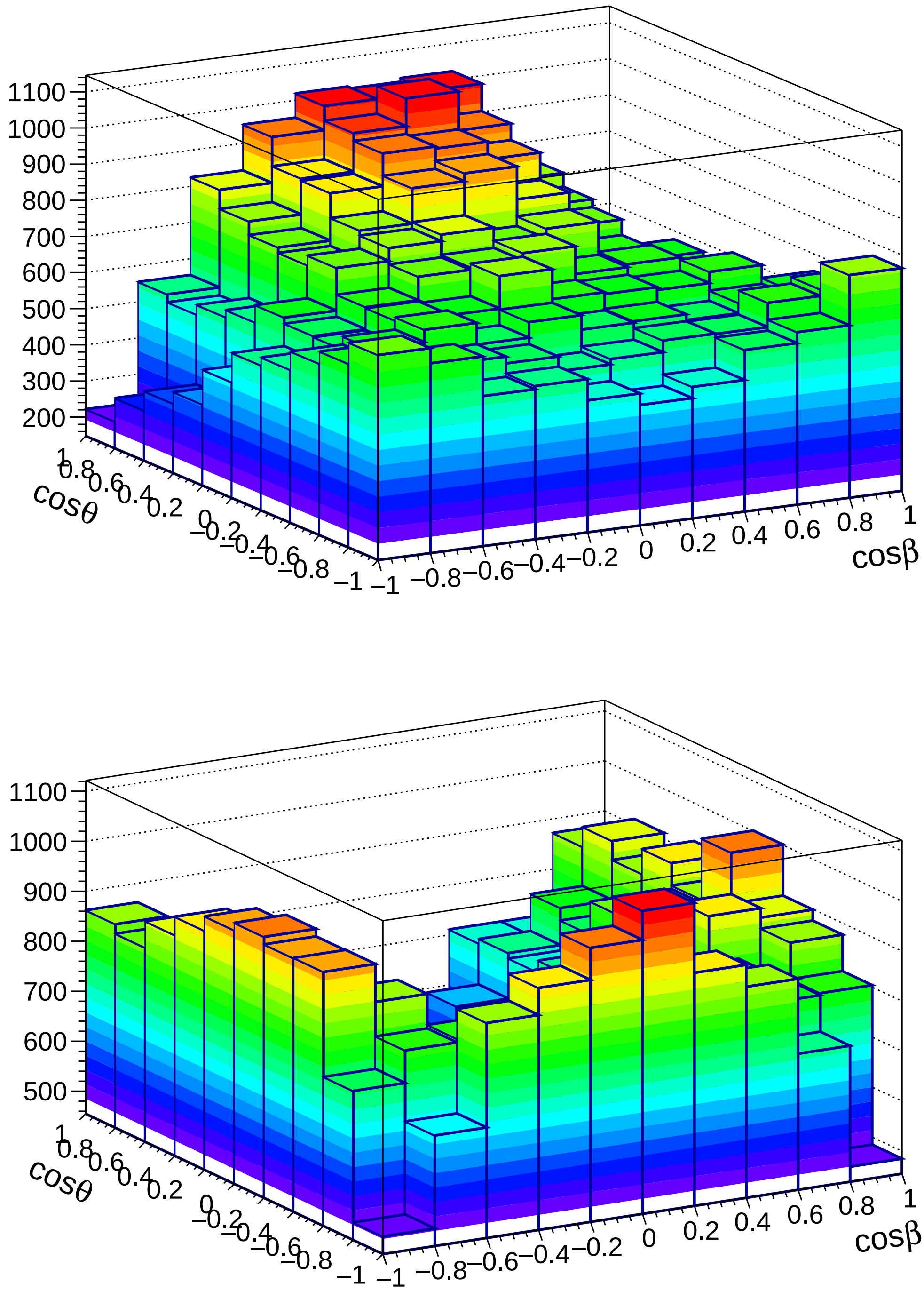

Figure 24: Distributions of the angles θ and β for the decay $\tau \rightarrow a_1\nu$; *Upper plot*: $h_\tau = +1$; *Lower plot*: $h_\tau = -1$.

5.2 Optimal Observable

The measurement of P_τ is not possible on an event-by-event basis. Instead, the angular distributions defined in the previous chapter can be used to determine the probability of a τ lepton being in the helicity state $h_\tau = +1$ or $h_\tau = -1$.

It can be shown that for each τ decay channel the decay distributions can be written as [14]:

$$\frac{1}{\Gamma}\frac{d^n\Gamma}{d^n\vec{\xi}} = f(\vec{\xi}) + P_\tau g(\vec{\xi}), \tag{5.11}$$

with the normalization and positivity conditions:

$$\begin{aligned} \int f(\vec{\xi})d^n\vec{\xi} &= 1, \\ \int g(\vec{\xi})d^n\vec{\xi} &= 0, \\ f(\vec{\xi}) &\geq 0, \\ |g(\vec{\xi})| &\leq f(\vec{\xi}), \end{aligned} \tag{5.12}$$

where $\vec{\xi}$ is the vector of all spin sensitive kinematic variables. The general approach to extract the polarization in an optimal way [33] uses the advantage of the linear dependence of the decay distributions on the polarization P_τ. For a sample of N τ decays, the true polarization maximizes the likelihood $\mathcal{L}(P_\tau, \vec{\xi})$ and therefore its value is obtained from:

$$\frac{d}{dp} log\mathcal{L}(P_\tau, \vec{\xi}) = \sum_i^N \frac{g(\vec{\xi}_i)}{f(\vec{\xi}_i) + P_\tau g(\vec{\xi}_i)} = \sum_i^N \frac{\omega_i}{1 + P_\tau \omega_i} = 0, \tag{5.13}$$

which depends only on the variable ω defined as:

$$\omega = \frac{g(\vec{\xi})}{f(\vec{\xi})} = \frac{|M_+(\vec{\xi})|^2 - |M_-(\vec{\xi})|^2}{|M_+(\vec{\xi})|^2 + |M_-(\vec{\xi})|^2}, \tag{5.14}$$

where $|M_\pm|^2$ is the squared matrix element of the decay for helicity plus and minus, respectively. A fit to the one dimensional distribution ω leads to the same result for polarization P_τ with the same error as the fit to the multidimensional distribution in the variable $\vec{\xi}$.

The variance on P_τ is (in the limit of large N),

$$\frac{1}{\sigma^2} = -\frac{\partial^2 log\mathcal{L}}{\partial^2 P_\tau} = N\langle \frac{\omega^2}{(1 + P_0\omega)^2} \rangle. \tag{5.15}$$

As an assessment of the sensitivity of the given τ decay channel to the polarization the following parameter is defined,

$$S^2 = \frac{1}{N\sigma^2} = \langle \frac{\omega^2}{(1 + P_0\omega)^2} \rangle = \int \frac{g^2}{f + P_0 g} d^n\vec{\xi}. \tag{5.16}$$

The parameter S quantifies the statistical error that results from a likelihood fit to the ideal distributions, i.e. not altered by the reconstruction effects. The sensitivity depends on the τ decay channel analyzed and the polarization P_τ. As can be seen from (5.16), a τ decay with larger sensitivity provides a better statistical uncertainty on the extracted value of P_τ.

5.3 Decay Model and Optimal Observable in the decay $\tau^- \to \pi^-\pi^-\pi^+\nu$

The decay model for $\tau^- \to \pi^+\pi^-\pi^-\nu_\tau$ used in this work is described in a general ansatz in Ref. [34].

The matrix element for this semi-leptonic τ lepton decay can be written as:

$$\mathcal{M}(\tau^- \to h^-\nu_\tau) = \frac{G_F V_{ij}}{\sqrt{2}} M_\mu J^\mu = \frac{G_F V_{ij}}{\sqrt{2}} \bar{u}_{\nu_\tau} \gamma_\mu (1-\gamma_5) u_\tau J^\mu, \tag{5.17}$$

where V_{ij} is the CKM matrix element and J^μ is the contravariant notation of the production of the hadronic state $h_1(q_1, ..., h_n(q_n)$ from the vacuum through the vector and axial vector hadronic currents $J^\mu = \langle h_1(q_1, ..., h_n(q_n) | J_A^\mu(0) + J_V^\mu(0)|0\rangle$.

From this, the differential decay width of $\tau^- \to h\nu_\tau$ can be simplified to

$$d\Gamma(\tau^- \to h^-\nu_\tau) = \frac{G_F^2 V_{ud}^2}{4m_\tau} \{L_{\mu\nu} H^{\mu\nu}\} dPS^{(4)}, \tag{5.18}$$

where $L_{\mu\nu}$ is the leptonic tensor describing the electro-weak decay of the τ, $H^{\mu\nu}$ is the hadronic tensor which describes the hadronic decay and $dPS^{(4)}$ is the differential phase space element, which can be expressed as:

$$dPS^{(4)} = \frac{m_\tau^2 - Q^2}{(2\pi)^5 64 Q^2 m_\tau^2} dQ^2 ds_1 ds_2 \frac{d\alpha}{2\pi} \frac{d\gamma}{2\pi} \frac{d\cos\beta}{2} \frac{d\cos\theta}{2}, \tag{5.19}$$

where α is the angle between the planes $(\vec{n}_{a_1}, \vec{n}_\tau)$ and $(\vec{n}_{a_1}, \vec{n}_\perp)$, $\vec{n}_\tau$ - is the unit vector along τ direction in the laboratory frame, and the vectors $\vec{n}_{a_1}$ and $\vec{n}_\perp$ are defined in Fig. 22. The angles θ, β and the γ are shown in Fig. 20 and 22.

The hadronic current, J^μ, from which the hadronic tensor is constructed ($H^{\mu\nu} = J^\mu (J^\nu)^\dagger$) contains the dynamic of the hadron decay and can be decomposed into 4 form factors:

$$J^\mu = J^\mu = \langle h_1(p_1, ..., h_n(p_n) | J_A^\mu(0) + J_V^\mu(0)|0\rangle = V_1^\mu F_1 + V_2^\mu F_2 + iV_3^\mu F_3 + V_4^\mu F_4, \tag{5.20}$$

where

$$\begin{aligned} V_1^\mu &= p_1^\mu - p_3^\mu - Q^\mu \frac{Q\cdot(p_1 - p_3)}{Q^2}, \\ V_2^\mu &= p_2^\mu - p_3^\mu - Q^\mu \frac{Q\cdot(p_1 - p_3)}{Q^2}, \\ V_3^\mu &= \epsilon^{\mu\alpha\beta\gamma} p_{1\alpha} p_{1\beta} p_{3\gamma}, \\ V_4^\mu &= Q^\mu = p_1^\mu + p_2^\mu + p_3^\mu. \end{aligned} \tag{5.21}$$

The terms proportional to F_1 and F_2 (F_3) describe the axial vector current (vector current) contributions and correspond to spin 1 of the hadronic system. The F_4 term originate from the spin 0 part of the axial current matrix element.

Integrating out the angle α and rearranging the term $L_{\mu\nu}H^{\mu\nu}$ to 16 symmetric and antisymmetric combinations of $L_X W_X$, the differential decay rate is written as [35]:

$$d\Gamma_{\tau\to\pi\pi\pi\nu} = \frac{G_F^2(m_\tau^2 - Q^2)}{256(2\pi)^5 m_\tau^3}((v_\tau^{CC})^2 + (a_\tau^{CC})^2)cos^2\theta_C \sum_X \bar{L}_X W_X \frac{dQ^2}{Q^2} ds_1 ds_2 \frac{d\gamma}{2\pi}\frac{dcos\beta}{2}\frac{dcos\theta}{2}, \tag{5.22}$$

where v_τ^{CC} and a_τ^{CC} are the vector and axial-vector weak charged couplings.

The hadronic structure functions W_X describe the dynamics of the 3π decay and depend on invariant masses s_1,s_2 and Q^2, which are defined as:

$$s_i = (E_j + E_k)^2 - (\vec{p}_j + \vec{p}_k)^2, (i, j, k = 1, 2, 3; i \neq j \neq k) \tag{5.23}$$

$$Q^2 = E_{3\pi}^2 - (\vec{p}_{3\pi})^2, \tag{5.24}$$

where $\vec{p}_i$ and $\vec{E}_i$ denote the momentum and energy of the pion i. The indices 1 and 2 are assigned to the same charge pions and the index 3 to the opposite charge pion. $E_{3\pi}$ and $\vec{p}_{3\pi}$ are the sum of the pion energies and momenta, respectively. The explicit expressions for L_X, W_X and the angles angles θ, β and γ can be found in Ref. [34]. All variables are measured in the laboratory frame.

The decay rate distribution (5.22) can be written in a form (5.11) with $\vec{\xi} = (\cos\theta, \gamma, \cos\beta, s_1, s_2, Q^2)$. The explicit form for the functions f and g is [35]:

$$\begin{aligned} f(cos\theta, \gamma, \cos\beta, s_1, s_2, Q^2) =& \frac{1}{3}[(2 + \frac{m_\tau^2}{Q^2}) + \frac{1}{2}(3\cos^2\beta - 1)U]W_A - \\ & \frac{1}{2}\sin^2\beta\cos 2\gamma U W_C + \frac{1}{2}\sin^2\beta \sin 2\gamma U W_D + \\ & \cos\psi\cos\beta W_E \end{aligned} \tag{5.25}$$

$$\begin{aligned} g(cos\theta, \gamma, \cos\beta, s_1, s_2, Q^2) =& \frac{1}{3}[\cos\theta(\frac{m_\tau^2}{Q^2} - 2) - \frac{1}{2}(3\cos^2\beta - 1)V]W_A + \\ & \frac{1}{2}sin^2\beta\cos 2\gamma V W_C - \frac{1}{2}\sin^2\beta\cos 2\gamma V W_D - \\ & cos\beta(\cos\theta\cos\psi + \cos\theta\sin\psi\sqrt{\frac{m_\tau^2}{Q^2}})W_E, \end{aligned} \tag{5.26}$$

where

$$\begin{aligned} U =& \frac{3\cos^2\psi - 1}{2}(1 - \frac{m_\tau^2}{Q^2}), \\ V =& \frac{3\cos^2\psi - 1}{2}\cos\theta(1 + \frac{m_\tau^2}{Q^2}) + \frac{3}{2}\sin 2\psi\sqrt{\frac{m_\tau^2}{Q^2}}\sin\theta. \end{aligned} \tag{5.27}$$

The optimal observable for the decay $\tau^- \to \pi^+\pi^-\pi^-\nu$ is defined as $\omega_{a_1} = \frac{g(\vec{\xi})}{f(\vec{\xi})}$ and is used to measure the τ polarization asymmetry from data.

The sensitivity for variable ω_{a_1} and for other τ decay channels assuming $P_0 = 0$ is given in Table 5.1.

Table 5.1: The sensitivity S and branching fraction $\mathcal{B}$ for different τ decay channels.

Decay mode $\tau \to X$	Sensitivity S_X	$\mathcal{B}_X, \%$
$\tau \to \pi\nu$	0.6	10.83
$\tau \to \rho\nu$	0.54	25.52
$\tau \to a_1\nu$	0.44	8.99
$\tau \to e\nu\bar{\nu}$	0.22	17.41
$\tau \to \mu\nu\bar{n}u$	0.22	17.83

It should be noted that the reconstruction of ω_{a_1} or $\vec{\xi}$ requires the knowledge of the τ rest frame, which at LHC is a challenging task due to escaped neutrinos. However, combining together the whole available information of the decay topology it is possible not only to reconstruct the rest frame of the τ_{a_1} but the whole kinematic of the process $pp \to Z^0 \to \tau\tau \to \mu\nu\nu, a_1\nu$. The procedure is described in Chapter 8.

Chapter 6

The CMS detector at the Large Hadron Collider

6.1 The Large Hadron Collider

The Large Hadron Collider (LHC) [36] is the world biggest proton-proton collider located in Switzerland/France with a circumference of $\approx$ 27 km about 100 m below the ground. The collider was designed to accelerate protons to an energy of up to 7 TeV which corresponds to the center-of-mass energy of 14 TeV in head-on collisions. Each proton beam consists of 2808 bunches with 1.15×10^{11} protons in each. The large general-purpose particle detectors at LHC are CMS [37] and ATLAS [38] designed to investigate the largest range of physics possible. Having two independently built detectors is crucial for cross-confirmation of any new discovery and measurements of new phenomena. The two smaller experiments LHCb [39] and ALICE [40] are focusing on more specific topics. LHCb is specialized on b quark physics, e.g. investigate CP violation effects, while ALICE is investigating the heavy ion collisions, e.g. focus on quark-gluon plasma. The CMS and ATLAS detectors are built for an instantaneous luminosity of $\mathcal{L} = 10^{34} cm^{-2} s^{-1}$.

6.2 The CMS detector

The Compact Muon Solenoid (CMS) detector is designed to measure the energy and momentum of charged particles, photons and neutral hadrons originating from the collision with high efficiency and resolution. As a typical general purpose detector CMS consist of subdetectors aimed on the reconstruction of objects of different type. Geometrically the CMS is divided into three parts: the barrel region ($\eta \lesssim |1|$) and two endcaps regions. The pseudorapidity η is:

$$\eta = \ln(\tan\frac{\theta}{2}).$$

The polar angle θ is defined from the z-axis of the detector pointing along the beam direction. The whole detector is centered around the interaction point. The first subdetector is the tracker consisting of the silicon pixel and strips trackers, followed by the electromagnetic calorimeter (ECAL) and hadronic calorimeter (HCAL). These detectors are inside a superconducting magnet inducing a solenoid field of 3.8 T. The most outer subdetector is the Muon System. The overall layout of CMS detector with indication of the various subdetectors is shown in Fig. 25. In the following a brief descriptions of the main detector components is given.

The primary goal of the tracker is the reconstruction of the track curvature to determine the transverse momentum, p_T, of charged particle from the track radius. The tracker layout is shown in Fig. 26. The innermost tracker part closest to the interaction point is the silicon pixel detector (PIXEL), which consists of 3 barrel layers and 2 endcap disks made of pixel sensors on each side. The 3 barrel layers are located at mean radii of 4.4 cm, 7.3 cm and 10.2 cm, and have a length of 53 cm. The 2 end disks, extending from 6 to 15 cm in radius, are placed on each side at $|z|$ = 34.5 cm and 46.5 cm.

The intermediate region (20 $<$ r $<$ 55 cm) is complemented by Tracker Inner Barrel (TIB) comprised four layers of silicon strip sensors that cover the region $|z|$ $<$ 65 cm and three Tracker Inner Disks (TID) at each side. The Tracker Outer Barrel (TOB) with six silicon sensor layers is placed in the region r $>$ 55 cm, r $<$ 110 cm and the z coordinate covers the range $|z|$ $<$ 120cm. The end cap parts in forward and backward regions are complemented by nine Tracker End Cap (TEC) disks at each side. The transverse and longitudinal coordinate resolution differs from 10 μm to 50 μm and from 20 μm to 500 μm, respectively, depending on the radius and the pseudorapidity.

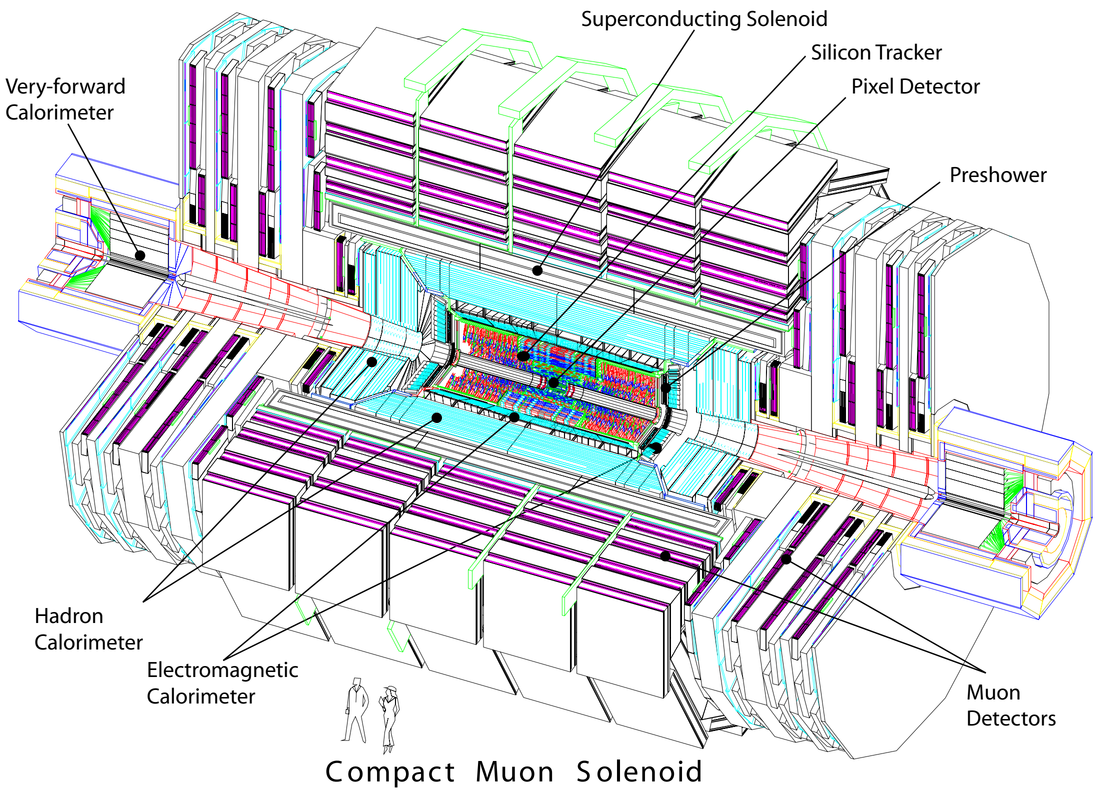

Figure 25: The CMS detector.

The inner tracking system is enclosed by two calorimeters. The Electromagnetic Calorimeter (ECAL) with an inner radius of 129cm is an almost hermetic and homogeneous calorimeter consisting of 61200 lead tungstate ($PbWO_4$) crystals mounted in the central barrel part (EB), covering the pseudorapidity range of $|\eta|$ $<$ 1.5, closed by 7324 crystals in each of the 2 end-caps (EE) with a pseudorapidity coverage of $|\eta|$ $<$ 3. The $PbWO_4$ crystals have a radiation length of X_0=0.89 cm, and a Moliere radius of 2.2 cm. The crystals have a front cross-section

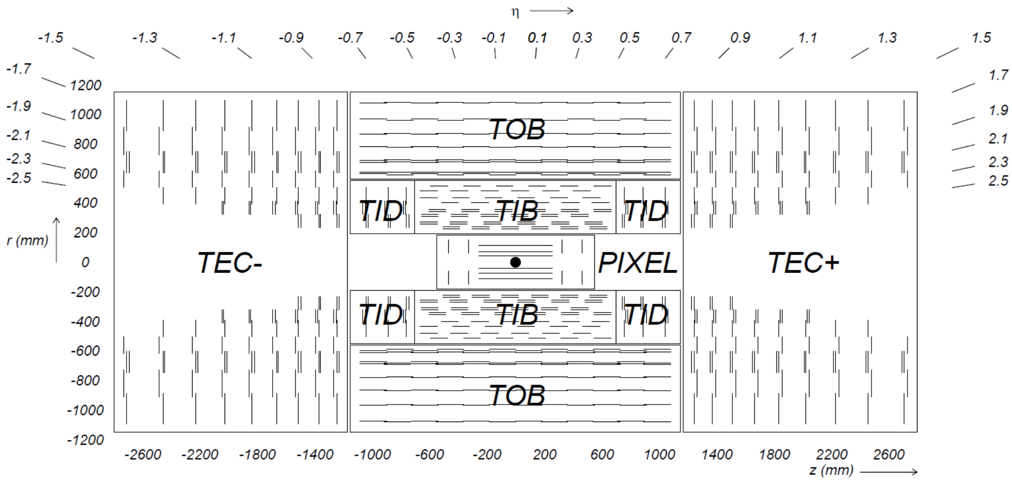

Figure 26: The layout of the CMS tracker.

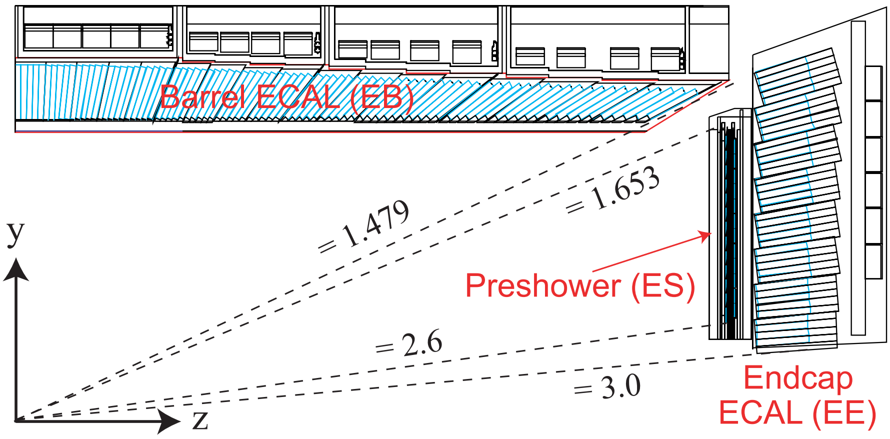

Figure 27: The layout of the CMS ECAL.

of about 22×22 mm^2 and a length of 230 mm, corresponding to 25.8 radiation lengths X_0. In the end cap regions $1.7 < |\eta| < 2.6$ the silicon preshower detector (ES) is placed.

The ECAL energy resolution is parametrized as a function of the energy:

$$(\frac{\sigma}{E})^2 = (\frac{2.83\%}{\sqrt{E}})^2 + (\frac{124 MeV}{E})^2 + (0.26\%)^2.$$

The resolution for a photon with energy of 100 GeV is better than half a percent. A quarter of the ECAL is shown in Fig. 27.

The second calorimeter is the hadron calorimeter (HCAL). The HCAL, as well as the ECAL, is used to measure the energy of hadrons and for the indirect measurement of the neutrinos by reconstructing the so-called missing transverse energy. The calorimeter is installed in a range of 181 cm < r < 286 cm. The three pseudorapidity ranges include the barrel part (HB) with a coverage $|\eta| < 1.4$, and the endcap part (HE) with $1.4 < |\eta| < 3$. Both are sampling calorimeters, use brass as an absorber interspersed with scintillator tiles as sensors. The

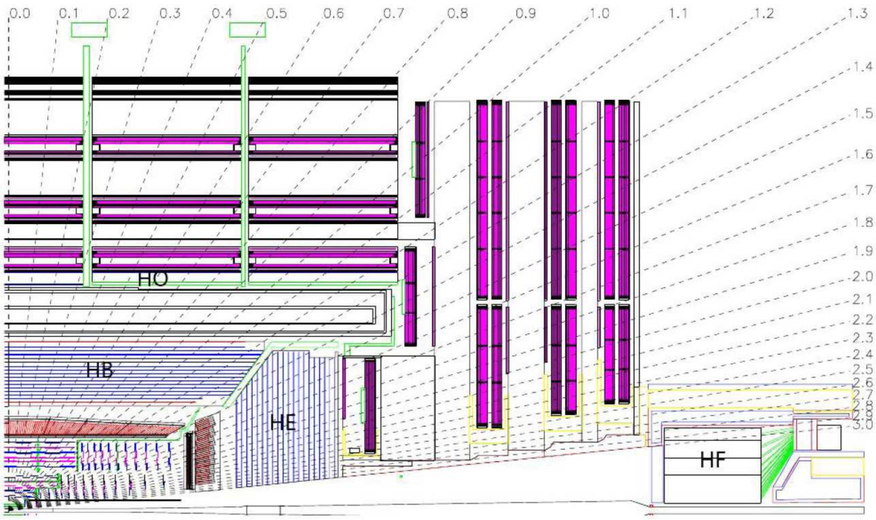

Figure 28: The layout of the CMS HCAL.

forward calorimeter (HF) $3 < |\eta| < 5$ consist of steel absorbers and quartz fibers as sensors. Schematically HCAL is shown in Fig. 28.

The most outer detector is the muon system, which exploits three different gaseous detectors. Four muon "stations" are integrated in the iron yoke, each comprises several layers of aluminium drift tubes (DT) in the barrel region ($|\eta| < 1.2$) and cathode strip chambers (CSCs) in the endcap region ($|\eta| < 2.4$), complemented by resistive plate chambers (RPCs). A quarter of the CMS muon system is shown in Fig. 29 The muon system provides excellent muon identification and spatial resolution. The second is significantly improved by a combination of the muon system and the CMS tracker. For muons with momentum of ≈ 1 TeV the resolution is $\delta p/p \approx 5\%$. For muons with low momentum of ≈ 100 GeV the resolution is noticeably better, $\delta p/p \approx 1\%$.

A two level trigger system is used to deal with the 40 MHz proton-proton collision rate. The Level-1 trigger consists of flexibly programmable electronics which performs online a very fast reconstruction ($\approx$ μs) and reduces the output rate to 100 kHz. The High Level Trigger (HLT) is a software system implemented in a farm of about 2000 CPU cores. The HLT combines the data from all subdetectors and spends approximately 40 ms per CPU on each event. At the output the HLT reduces the accepted event rate to 300 Hz.

6.2.1 Objects Reconstruction

This section describes the reconstruction of basic objects that are relevant to identify and measure the kinematic of τ – lepton decay.

- Track reconstruction

The reconstruction of tracks in the CMS tracker is performed in four steps:

1. Provide a seed of initial track candidates using a few (2-3) hits in the tracker. A seed defines the initial rough estimate of the track trajectory and its uncertainty.
2. The Kalman Fitter extrapolates seed trajectory by the expected flight path of a charged particle in the CMS magnetic field.

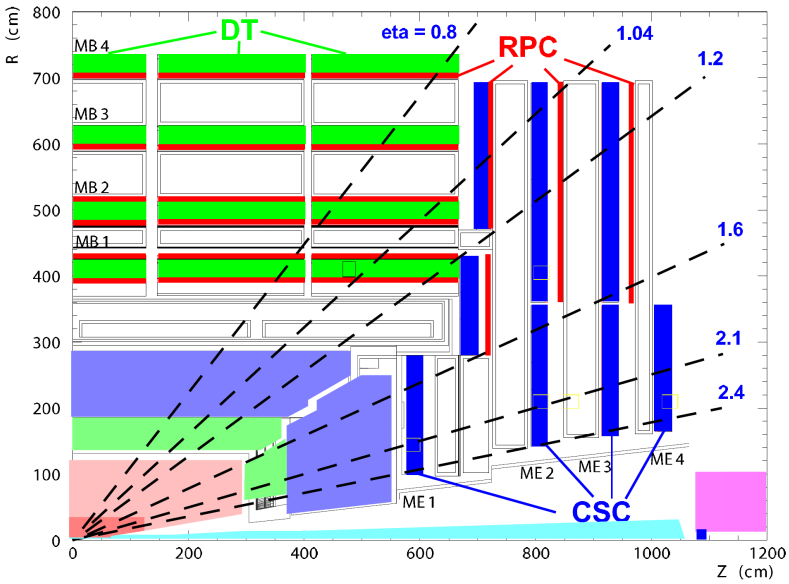

Figure 29: A quarter of the CMS muon system.

3. The iterative procedure searches firstly for tracks that are easiest to reconstruct, after each iteration hits associated with reconstructed tracks are removed from consideration, thereby simplifying the subsequent iteration.
4. After assigning all hits to tracks and cleaning the duplicates the Kalman Fitter performs a fit, determining five track helix parameters $(d_{xy}, d_z, \phi_0, \cot\theta, Q/p_T)$. The parameters d_{xy} and d_z are the transverse and longitudinal impact parameters, i.e. the minimal transverse and longitudinal distances between the track and interaction point. ϕ_0, θ are the azimuthal, and polar angles of the track at the point defined by the parameters d_{xy} and d_z. Q and p_T are the charge and transverse momentum of the particle.

The reconstruction of muon tracks is better than that of other charged particles, mainly because muons interact only with the silicon detector through ionization and their energy loss due to bremsstrahlung is negligible. Also muons cross the whole detector volume, producing hits in the muon system also considered during the track reconstruction.

The relative transverse momentum resolution of muons and pions as a function of the transverse momentum is shown in Fig. 30, and the reconstruction efficiency for muons and pions as a function of transverse momentum and rapidity is shown in Fig. 31 [41].

- Vertex reconstruction

The vertex reconstruction is performed in two steps. The first step consist in searching and grouping tracks that originate from a common space point. The second step includes the fitting and determination of vertex position using the track helix parameters. The primary vertex positions are required to be within 2 cm around the beamspot in transverse direction and not more than 24 cm away from the detector centre in longitudinal direction. The primary vertex with the largest sum of p_T of all tracks is chosen as the event vertex. The reconstruction of secondary vertices is performed using tracks that are not associated to any primary vertex. The reconstruction of primary and secondary vertices in the process $Z \to \tau\tau \to \mu\nu\nu$, $a_1\nu$ is described in Chapter 8.

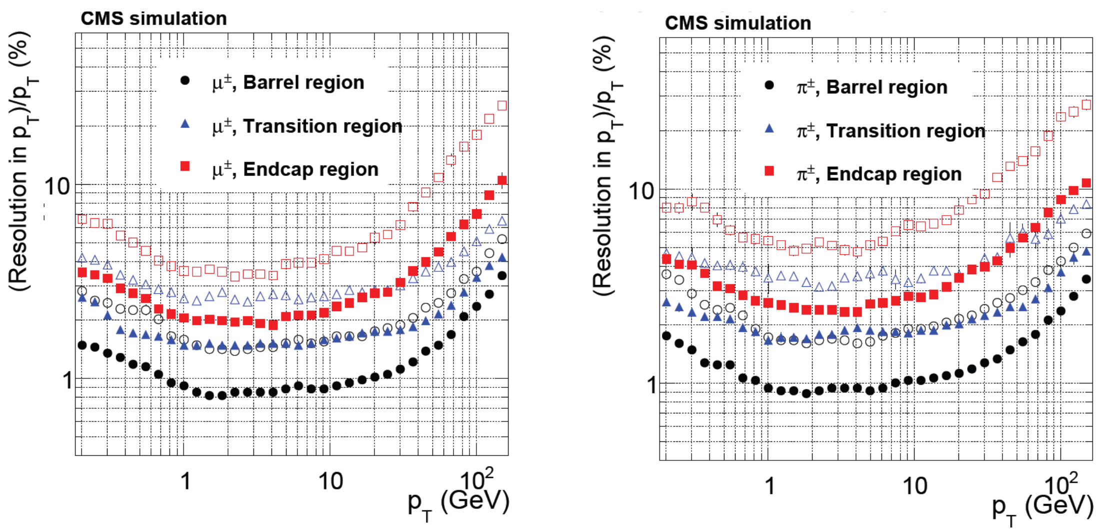

Figure 30: Momentum resolution, as a function of p_T for muons (*Left*) and for pions (*Right*). The solid (open) symbols correspond to the half-width for 68% (90%) intervals of the resolution distribution at each bin of p_T .

- Tau reconstruction

Reconstruction of the momentum of the decay products of the τ lepton, hereafter referred to as visible momentum of the τ lepton, and the decay channel identification is performed by the "Hadron Plus Strips" algorithm (HPS)[42]. The algorithm is intended to reconstruct individual τ decay modes exploiting the excellent performance of the Particle Flow algorithm [43]. Combining the information from all CMS sub-detectors the Particle Flow algorithm reconstructs individual charged hadrons, neutral hadrons, electrons, photons and muons.

The HPS algorithm is performed in two steps:

1. Reconstruction: Combinations of charged and neutral particles reconstructed by the Particle Flow algorithm that are compatible with the hadronic τ decay signature. The visible four-momentum of the τ_h candidate is computed as a sum of particles identified as τ decay products.
2. Identification: Various discriminators are introduced in order to distinguish the hadronic τ decays from quark and gluon jets, electrons and muons. The discriminators are based on the multivariate technique and compare the signature in the detector which can be produced by the hadronically decaying tau, τ_h and by the objects which can fake τ_h. Discriminators are intended to reduce the rate of $jet \rightarrow \tau_h$, $e \rightarrow \tau_h$, $\mu \rightarrow \tau_h$ fakes.

The reconstruction of hadronic τ decays require the reconstruction of π^0 being present in a large fraction of τ decays. The large amount of tracker material, sensors, electronics, cables, etc., results in a large probability of photons originating from the decay $\pi^0 \rightarrow \gamma\gamma$ to be converted into a e^+e^- pair in the tracker. The photon candidates are reconstructed as a $\eta - \phi$ "strip" in ECAL. A strip is an energy deposition in the ECAL containing the electromagnetic shower from the photon or $e^{\pm}$. The strip size, $\Delta\eta \times \Delta\phi$ =0.20 $\times$ 0.05 is enlarged in η to account for the signal broadening due to bending of electrond and positron pair in the magnetic field. Strips that contain one or more photons with a transverse momentum $>$ 2.5 GeV give rise to π^0 candidates. The charged particles are required to pass the quality criteria

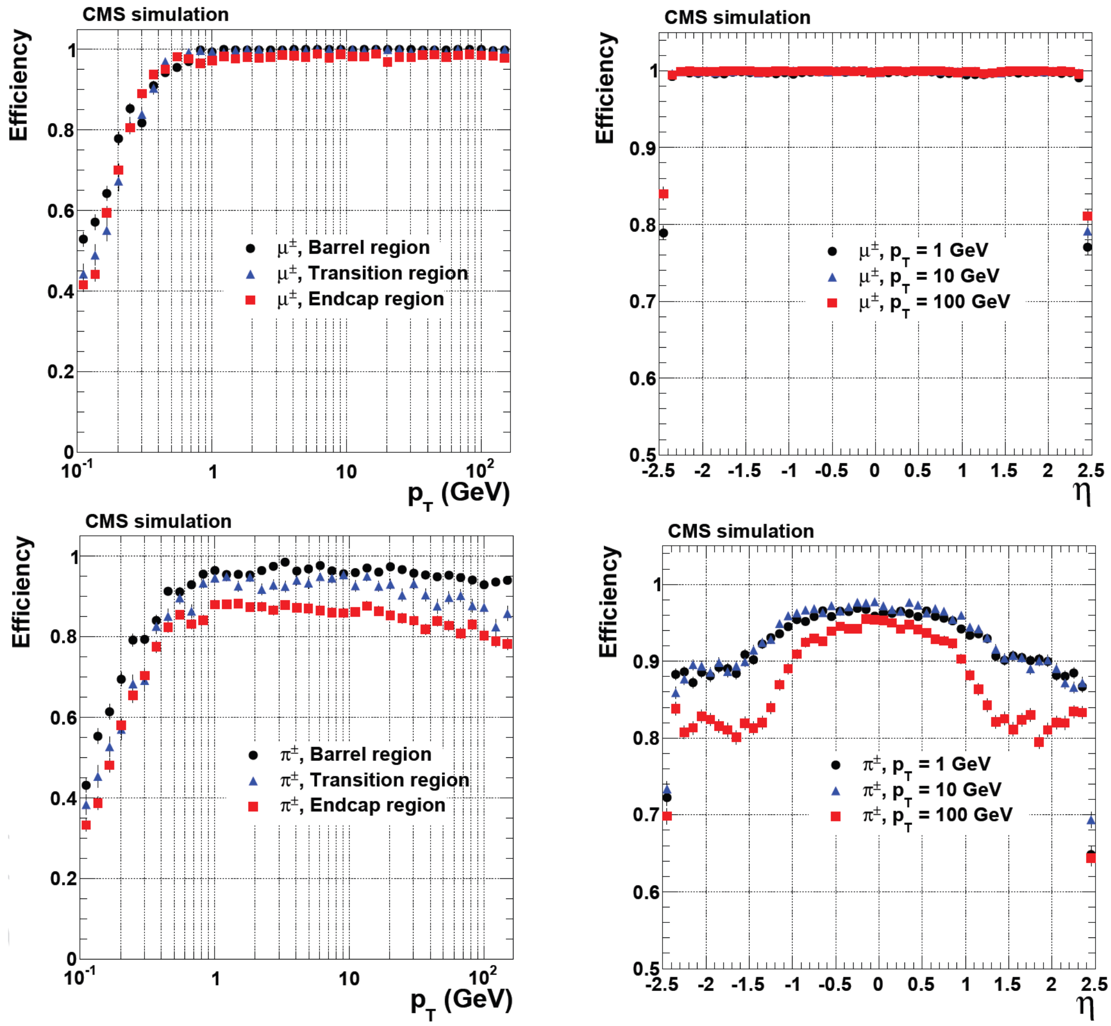

Figure 31: Track reconstruction efficiency for muons (*Top*) and pions (*Bottom*). Efficiencies are shown as a function of p_T (*Left*) for the barrel, transition and endcap regions, that are defined by the η intervals 0–0.9, 0.9–1.4 and 1.4–2.5, respectively and as a function of η (*Right*) for p_T = 1, 10, 100 GeV.

given in Table. 6.1

Individual hadronic τ decay modes are build by combining the strips and charged tracks reconstructed, giving rise to four decay categories:

- Three Hadrons: Combination of three charged hadrons with invariant mass of 0.8 $<$ M $<$ 1.5 GeV. The tracks are required to originate from a common vertex within Δz $<$ 0.4 cm and with total charge ± 1.
- Hadron plus two Strips: Combination of one charged hadron with two strips with an invariant mass of $0.4 < \mathrm{M} < 1.2 \times \sqrt{P_T[\mathrm{GeV}]/100\mathrm{GeV}}$. The mass window is enlarged for high PT τ_h candidates to account for resolution effects. For τ_h candidates with transverse momentum $p_T < 100$ GeV (> 1111 GeV) the upper limit of the mass window is set to 1.2 GeV (4.0 GeV).
- Hadron plus one Strip: Combination of one charged hadron plus one strip, fitting

Table 6.1: Quality criteria applied to charged particles used for building τ_h candidates. p_T is the track transverse momentum, χ^2 is the track reconstruction quality parameter, d_{xy} and d_z are the track impact parameters and N_{hit} total number of hits associated to a track in the detector.

Parameter	Value
p_T	>0.5 GeV
χ^2	< 100
d_z	< 0.03 cm
d_{xy}	< 0.4 cm
N_{hit}	≥ 3

within a mass window of $0.3 <$ M $< 1.3\sqrt{P_T[\text{GeV}]/100\text{GeV}}$. For τ_h candidates with $P_T < 100$ GeV (> 1044 GeV) the upper limit of the mass window is set to 1.3 GeV (4.2 GeV).

- Single hadron: A single charged hadron reconstructed by the PF algorithm without any strips.

If τ_h candidate fulfill more than one of the categories above the one with the largest p_T is given preference. Additionally the electrons and muons originating from Z and W decays, have a probability to pass τ_h identification criteria. Dedicated anti-electron and anti-muon discriminators, based on a multivariate approach, have been developed to reduce $e \rightarrow \tau_h$ and $\mu \rightarrow \tau_h$ fakes.

The isolation of τ_h candidate, I_τ, is calculated as a sum of the transverse momentum of all charged particles with $p_T > 0.5$ GeV and photons with transverse energy E_T >0.5 GeV that are found within a cone of $\Delta R = 0.5$ around the τ_h direction, when $\Delta R = \sqrt{\Delta\phi^2 + \Delta\eta^2}$. All tracks are required to have d_z >0.2 cm. The contribution of tracks arising from other primary vertices are accounted for by applying a corrections $\Delta\beta$:

$$I_\tau = \sum p_T^{tracks}(d_z < 0.2cm) + max(P_T^\gamma - \Delta\beta, 0).$$

The $\Delta\beta$ corrections are calculated by summing the transverse momenta of tracks that are contained in a cone of size $\Delta R = 0.8$ and have $d_z > 0.2$ cm from the primary vertex that τ_h is assigned to.

$$\Delta\beta = 0.4576 \sum p_T^{tracks}(d_z > 0.2cm).$$

Three working points are defined: Loose, Medium and Tight by requiring the τ_h isolation, I_τ, not to exceed the value of 2.0, 1.0, 0.8 GeV, respectively. The efficiency of a τ candidate to pass the HPS reconstruction is shown in Fig. 32 [42].

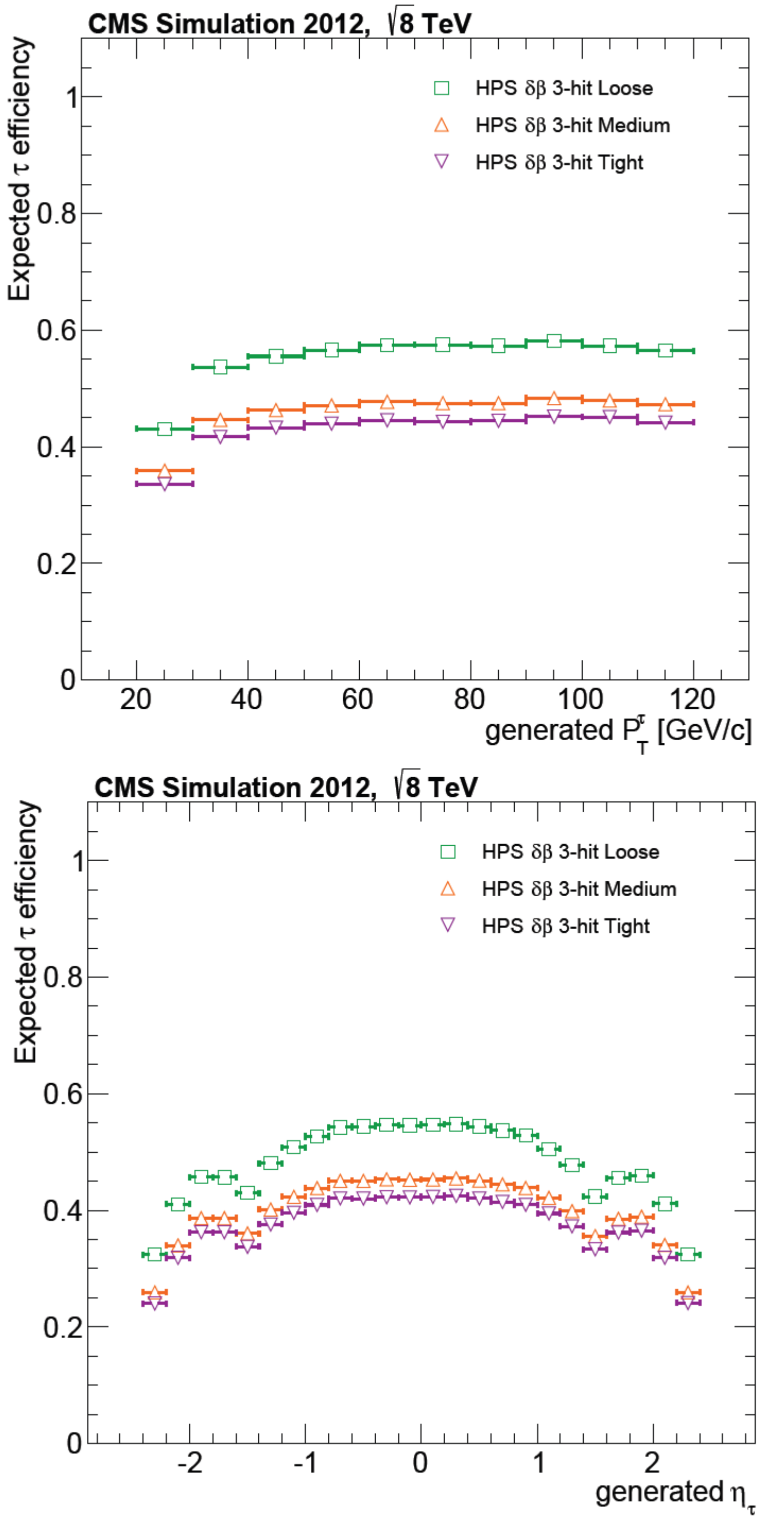

Figure 32: Efficiency for hadronic τ decay to pass Loose, Meidum and Tight working points. The efficiencies are plotted as a function of p_T (*Upper plot*) and η (*Lower plot*).

Chapter 7

Selection of $Z \longrightarrow \tau\tau$ events

This chapter describes the selection of $Z \rightarrow \tau\tau \rightarrow \mu\nu\nu, 3\pi\nu$ events and estimation of the background using data corresponding to an integrated luminosity of $\mathcal{L} = 19.7\,\mathrm{fb}^{-1}$ of proton-proton collisions collected at $\sqrt{s} = 8$ TeV in the 2012. The Monte Carlo to data corrections are described at the end of the chapter.

7.1 Data and Monte-Carlo Samples

A list of the data samples and Monte Carlo samples used in this analysis is shown in Tables 7.1 and 7.2.

Table 7.1: The data samples used in this analysis with the corresponding run range and integrated luminosity.

Data Sample	Run range	$\mathcal{L}$ [fb^{-1}]
Run2012A	190456-193621	0.887
Run2012B	193833-196531	4.446
Run2012C	198022-203742	7.153
Run2012D	203777-208686	7.318

Table 7.2: The list of used Monte Carlo samples.

Process	Monte Carlo Sample	Cross-section [pb]
$Z^0 \rightarrow l^+l^-$	DYJetsToLL_M-50_TuneZ2Star_8TeV-madgraph-tarball	3503.7 [44]
$W^\pm \rightarrow l^\pm\nu$	WJetsToLNu_TuneZ2Star_8TeV-madgraph-tarball	36257.2 [44]
	WJetsToLNu_TuneZ2Star_8TeV-madgraph-tarball (version 2)	36257.2 [44]
$t\bar{t}$	TT_CT10_TuneZ2star_8TeV-powheg-tauola	239 [45]
Di-Boson	ZZJetsTo2L2Q_TuneZ2star_8TeV-madgraph-tauola	2.502 [44, 46]
	WZJetsTo2L2Q_TuneZ2star_8TeV-madgraph-tauola	2.207 [44, 46]
	ZZJetsTo2L2Nu_TuneZ2star_8TeV-madgraph-tauola	0.716 [44, 46]
	WWJetsTo2L2Nu_TuneZ2star_8TeV-madgraph-tauola	5.824 [44, 46]

All background contributions except arising from QCD events are modeled using Monte Carlo simulations. The shape of $W + Jets$ events is taken from Monte Carlo simulation, while the overall normalization is estimated from data. Monte Carlo events are normalized to the respective NNLO cross-sections [47]. The contributions from Di-Boson events are combined together and labelled as electroweak background (EWK). The τ leptons are decayed using TAUOLA [48], τ polarization is modeled using TauSpinner [49]. All generated events are passed the full GEANT [50] simulation of the CMS apparatus and are reconstructed using the same CMS software release, as used for the data.

There are three background contributions from $Z \to \tau\tau$ with a signature similar to the μa_1 final state, namely $Z \to \mu/3\pi\pi^0, KK\pi, K\pi\pi$. These contributions are treated as *signal* events. The branching fractions of these τ decays and their contribution to the signal cross section are given in Table 7.3. The signal cross section summed over all final states, labelled hereafter as $\tau\tau \to \mu 3h(\pi^0)$, is 55.93 $\pm$ 0.36 pb^{-1}.

Table 7.3: The branching fractions of the hadronic tau decays selected as signal and the corresponding cross sections leading to the $\mu 3h(\pi^0)$ final state.

Decay	B	$\sigma(Z \to \tau\tau \to \mu\nu, X\nu)$, pb^{-1}
$a_1\nu$	(8.99 $\pm$ 0.06) %	36.56
$3\pi\pi^0\nu$	(4.76 $\pm$ 0.06) %	19.36
$KK\pi\nu$	(3.49 $\pm$ 0.16) $\times 10^{-3}$	1.41
$K\pi\pi\nu$	(1.44 $\pm$ 0.05) $\times 10^{-3}$	0.58

7.2 Event Selection

7.2.1 Trigger

Each event is required to pass the cross trigger that require the presence of muon and hadronically decaying tau candidates. The trigger requirements include the loose isolation on both μ and τ candidates and the requirement on a minimum transverse momentum. The transverse momentum threshold is different depending on the run period. The list of used triggers requirements is given below:

- Isolated muon with $p_T > 12$ GeV and isolated tau with $p_T > 10$ GeV
- Isolated muon with $p_T > 15$ GeV and isolated tau with $p_T > 15$ GeV
- Isolated muon with $p_T > 15$ GeV and $|\eta| < 2.1$ and isolated tau with $p_T > 20$ GeV
- Isolated muon with $p_T > 17$ GeV and $|\eta| < 2.1$ and isolated tau with $p_T > 10$ GeV
- Isolated muon with $p_T > 18$ GeV and $|\eta| < 2.1$ and isolated tau with $p_T > 10$ GeV

The objects that are identified by the trigger as tau and mu candidates are required to match the finally selected tau and mu.

7.2.1.1 Muon Selection

The muon candidate is required to be identified by the particle-flow algorithm [43] and Global muon reconstruction [51] with $\chi^2/ndf < 10$ and at least one hit in the muon chamber included in the global-muon track fit. Additionally, transverse and longitudinal impact parameters of the muon track are required to be less than 0.2 cm and 0.5 cm, respectively.

To suppress muons from decays in flight and to ensure a good p_T measurement the track is required to have at least one pixel and at least six tracker layer hits.

Furthermore, the transverse momentum must be greater than 20 GeV and the pseudorapidity $|\eta|$ less than 2.1. In order to suppress contamination's from muons within jets or decays in flight the selected muon candidate has to be isolated. The isolation is based on particle-flow candidates and accounts for transverse energy deposits from photons, neutral hadrons and charged particles found within an isolation cone of size $\Delta R < 0.4$ around the muon candidate. The quantity

$$I_{rel} = \frac{\Sigma p_T(charged) + max(\Sigma E_T(neutral) + \Sigma E_T(photon) - \Delta\beta, 0)}{p_T^{\mu}}, \tag{7.1}$$

where $p_T(charged)$ are the transverse momenta of charged particles, $E_T(neutral, photons)$ the transverse energies of neutral hadrons and photons and $\delta\beta$ is a correction accounting for possible energy contribution from particles arising from other primary vertices, must be less than 0.12.

7.2.1.2 τ Selection

τ-lepton candidates decaying into three charged hadrons is required to pass the "Three Hadrons" category of the HPS algorithm as described in 6.2.1. In addition, the transverse momentum and pseudorapidity of the a_1 must be $p_T > 20$ GeV and $|\eta| < 2.1$, respectively.

Being produced in the decay of colorless boson, τ leptons, as well as, their decay products are, in contrary to quark and gluon jets, isolated in the detector. The τ_h candidate is required to pass the Medium working point of the HPS reconstruction, i.e. the τ_h isolation, I_τ is required to be larger than 1.0 GeV

Additionally, the presence of three tracks in the τ_h decay allows to reconstruct the point in space of the τ decay, the secondary vertex (SV), as described in Section 8. With the knowledge of the interaction point, primary vertex (PV), the flight length of the τ_h lepton can be calculated as $|\vec{r}_{SV} - \vec{r}_{PV}|$. Also this quantity can be expressed in units of its uncertainty, $\sigma_{PV-SV} = \frac{\vec{r}_{SV} - \vec{r}_{PV}}{\sigma_{|\vec{r}_{SV} - \vec{r}_{PV}|}}$. The value σ_{PV-SV} is called flight length significance and provides a very powerful discrimination against jets that fake a τ_h, as shown in Fig. 33. In the selection the value of σ_{PV-SV} is required to be larger than 2.2, to suppress a large fraction of the backgrounds.

7.2.2 Event Criteria

Only events with oppositely charged muon and the τ_h are considered. To further discriminate signal events from background, like W+Jets, where the W decays to a muon and a neutrino, and an additional jet which fakes a τ_h, the missing transverse mass,

$$M_T(\mu) = \sqrt{2 p_T(\mu) MET (1 - cos(\Delta\phi_{\mu,MET}))} \tag{7.2}$$

is used. MET is the missing transverse energy and $\Delta\phi_{\mu,MET}$ the angle between the muon transverse momentum at the interaction point and the direction of the MET. $M_T(\mu)$ must be less than 35 GeV. The invariant mass distribution of the selected pair and $M_T(\mu)$ (without cut applied) are shown in Fig. 34. A cut on $M_T(\mu)$ is powerful against the background events with large transverse mass, $M_T(\mu)$.

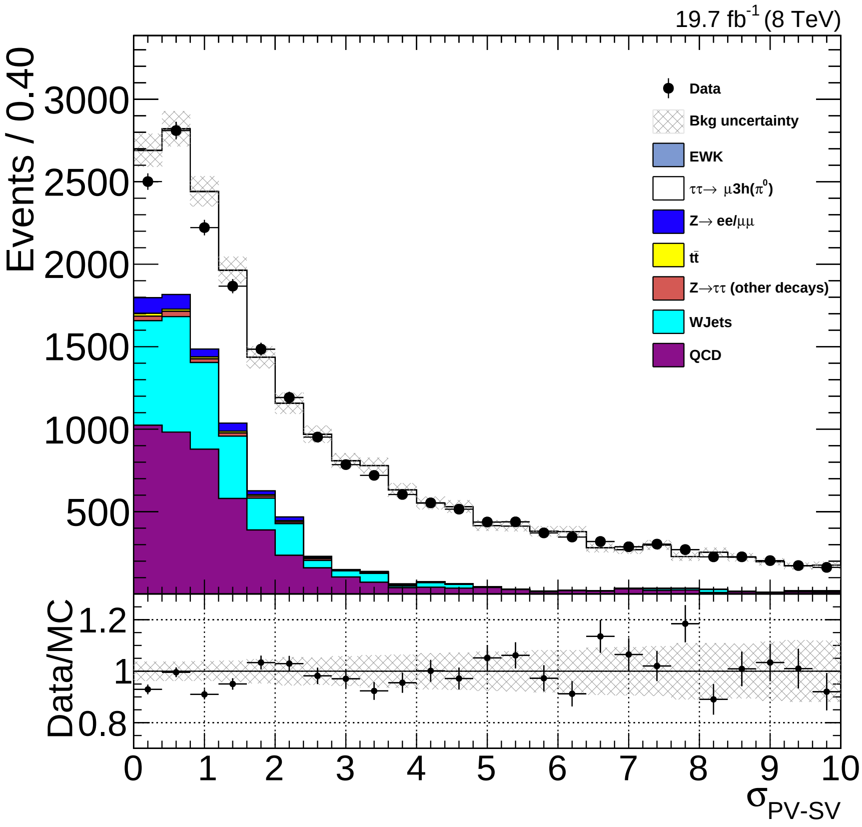

Figure 33: Flight length significance σ_{PV-SV} of the selected τ_h candidate and the background processes.

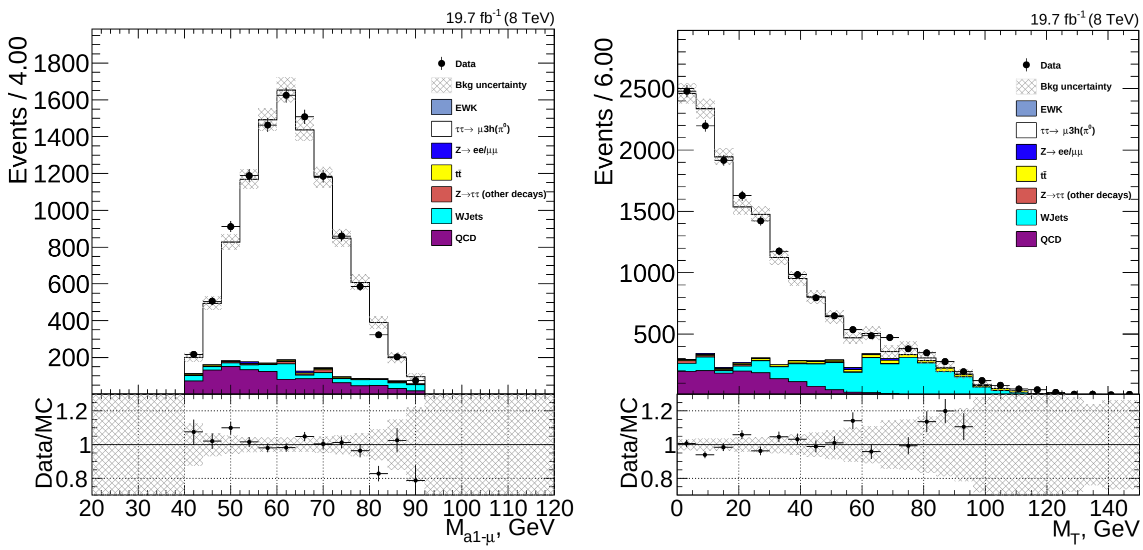

Figure 34: Distribution of the visible invariant mass of the selected pair (*Left*) and missing transverse mass, $M_T(\mu)$, defined in Eq. (7.2) (*Right*).

7.3 Background Estimation

7.3.1 QCD and W+Jets

The QCD and W+Jets background contributions are estimated from data. They are obtained by applying the selection as described above, except the requirement on the muon isolation and the requirements that the charge of the selected $\mu - \tau$ pair is opposite. Four regions are defined as shown in Fig. 35 (*left*). The control region where the charge of τ_h is required to be the same as the charge of muon and the signal region where τ_h and muon have opposite charge with the requirement on the muon $I_\mu < 0.12$. These two regions are referred to as the same-sign (B) and the opposite-sign (A) regions. The regions C and D are the same-sign and the opposite sign regions with the muon isolation being inverted. The value of muon isolation for regions C and D is chosen to be $I_\mu > 0.2$ in order to ensure that C and D are background dominated. Additionally two transverse mass regions are defined by applying a cut to M_T; High-M_T ($M_T > 70$ GeV) and Low-M_T ($M_T < 35$ GeV) as shown in Fig. 35 (*Right*).

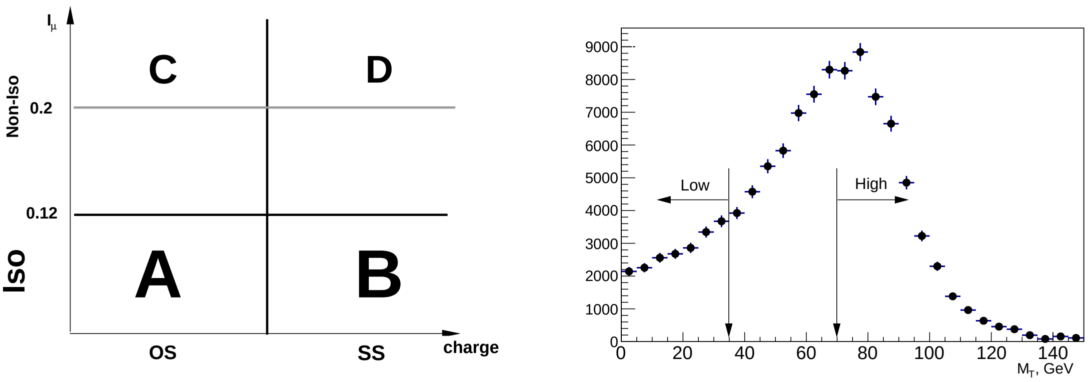

Figure 35: ABCD regions used to estimate the QCD background (*Left*); The missing transverse mass distribution obtained from Monte Carlo simulation (*Right*). OS stands for opposite charge of the $\mu - \tau_h$ pair, SS for the same sign.

The amount of QCD events in the signal region A is obtained by multiplying the number of events in the region B by the OS/SS extrapolation factor, $f^{OS/SS}$:

$$\begin{aligned} QCD^A_{Low} &= QCD^B_{Low} \times f^{OS/SS} \\ QCD^B_{Low} &= N^B_{Low} - EWK^B_{Low} - W^B_{Low}. \end{aligned}$$

The factor $f^{OS/SS}$ is defined as the ratio of observed events in regions C and D subtracted by the non-QCD background contributions estimated using MC predictions and is found to be:

$$f^{OS/SS} = 1.07 \pm 0.05.$$

N^B_{Low} is the number of observed events in region B, EWK^B_{Low} includes the contributions from

$t\bar{t}$, Di-boson and $Z \rightarrow ll + Jets$ and is estimated using the MC prediction. W^B_{Low} is the expected number of W+Jets events in region B and in signal region A. It is obtained by extrapolating the amount of observed events in the region $M_T > 70$ GeV, which is expected to be dominated by W+Jets, by using factors $f^{SS}_{Low/High}$ and $f^{OS}_{Low/High}$:

$$\begin{aligned} W^B_{Low} &= W^B_{High} \times f^{SS}_{Low/High}, \\ W^A_{Low} &= W^A_{High} \times f^{OS}_{Low/High}. \end{aligned}$$

The factors $f^{SS}_{Low/High}$ and $f^{OS}_{Low/High}$ are obtained using the M_T shape obtained from the W+Jets MC sample, as shown in Fig. 35 (*Right*). Both W^B_{High} and W^A_{High} are corrected for the EWK contribution using the MC prediction.

As a cross check the estimated number of W+Jets events in signal region A is compared to the prediction obtained from Monte Carlo simulation, and found to be in agreement within 3%.

7.3.2 Other backgrounds.

7.3.2.1 $Z \rightarrow \mu\mu, ee$

$Z \rightarrow \mu\mu$ process contribute if additional QCD jet is misidentified as τ_h. In order to suppress it a di-muon veto is applied. Cases in which one of the muons fake τ_h, are rejected if the τ_h candidate is required to pass the anti-muon HPS discriminator. The contribution from the $Z \rightarrow ee$ process is suppressed by applying an electron veto and the anti-electron HPS discriminator to the τ_h candidate. Both $Z \rightarrow \mu\mu, ee$ contributions are estimated using Monte Carlo simulation.

7.3.2.2 Other τ decays in $Z \rightarrow \tau\tau$

Contributions from other τ decays are estimated using Monte Carlo simulation. The only large contribution is coming from the $3\pi\pi^0\nu$ decay, which is approximately 10% of the final selected signal events. Since the $Z \rightarrow \tau\tau$ background is polarization dependent it is treated as signal.

7.3.2.3 $t\bar{t}$ and di-bosons

The background contributions from $t\bar{t}$ and di-bosons are estimated entirely from Monte Carlo simulation and are found to be very small. The total contribution of EWK events is estimated to be less than 1% of the selected sample.

7.4 Corrections Applied to Monte Carlo Samples

In order to account for biases on measured objects and imperfect modeling in the simulation the following corrections are applied:

- Pileup

The Monte Carlo simulation assumes a number of interaction per bunch crossing called pileup being usually slightly different from the real running conditions. The level of pileup can be estimated the distribution of the number of reconstructed primary vertices. In every sample of Monte Carlo events the number of interaction per bunch crossing is corrected to match the one in data by applying the pileup weight to each event. The distributions of the number of primary vertices for data and MC samples are shown in Fig. 36 (*Left*) . Both distributions are in good agreement.

- μ, τ_h trigger efficiency
- τ_h energy scale

The trigger efficiency is determined using a tag-and-probe method. In this approach, the trigger selection under study represents the probe, while a tighter trigger selection is used as a tag. The correction arising from different trigger efficiencies in Monte Carlo and data is applied as described in Ref. [52]. The energy scale correction on τ_h is taken according to recommendations given in Ref. [42].

- μ momentum scale
- μ isolation and identification efficiency

The muon momentum scale, isolation and identification efficiency have been studied using $Z \to \mu\mu$ events and the corrections are applied according to the recommendations received from private communications with the corresponding CMS working group.

- $E_{\mathrm{T}}^{\mathrm{miss}}$ resolution and response

Different kind of corrections are necessary for the missing transverse energy. The largest contribution to a bias in the MET measurement is coming from the jet energy misreconstruction. Other uncertainties arise from pileup. These corrections are applied according to Ref. [53].

The corrected missing transverse mass distribution for the selected events is shown in Fig. 34 (*Right*). The transverse momentum distribution of the selected τ and μ candidates and are shown in Fig. 37. The invariant mass of pions from τ_h decay is shown in Fig. 36 (*Right*). Fairly good agreement is observed in all distributions.

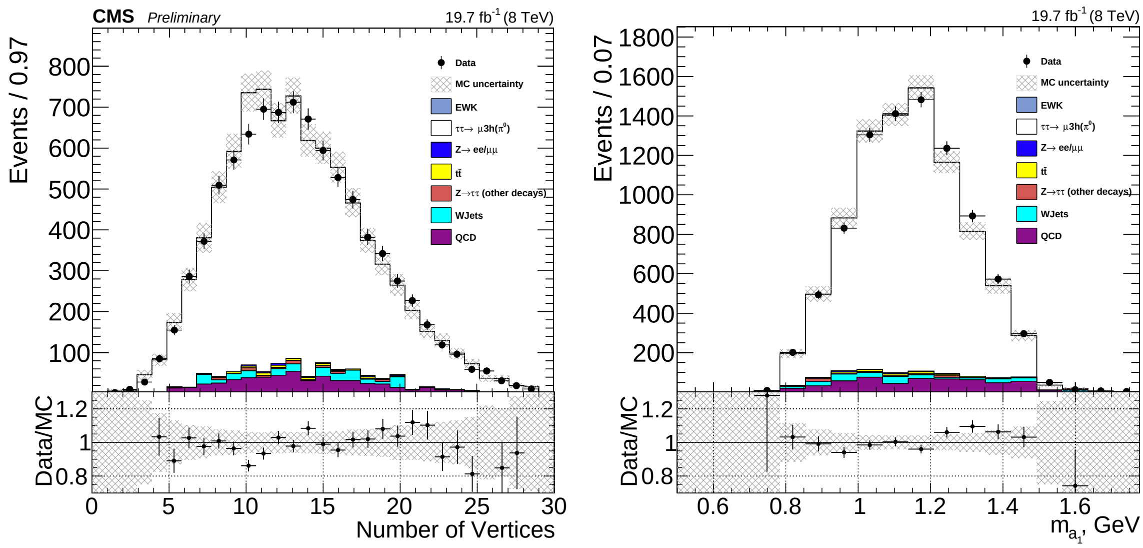

Figure 36: Number of Primary Vertices (*Left*) . The invariant mass of three pions from the selected τ_h candidate (*Right*) .

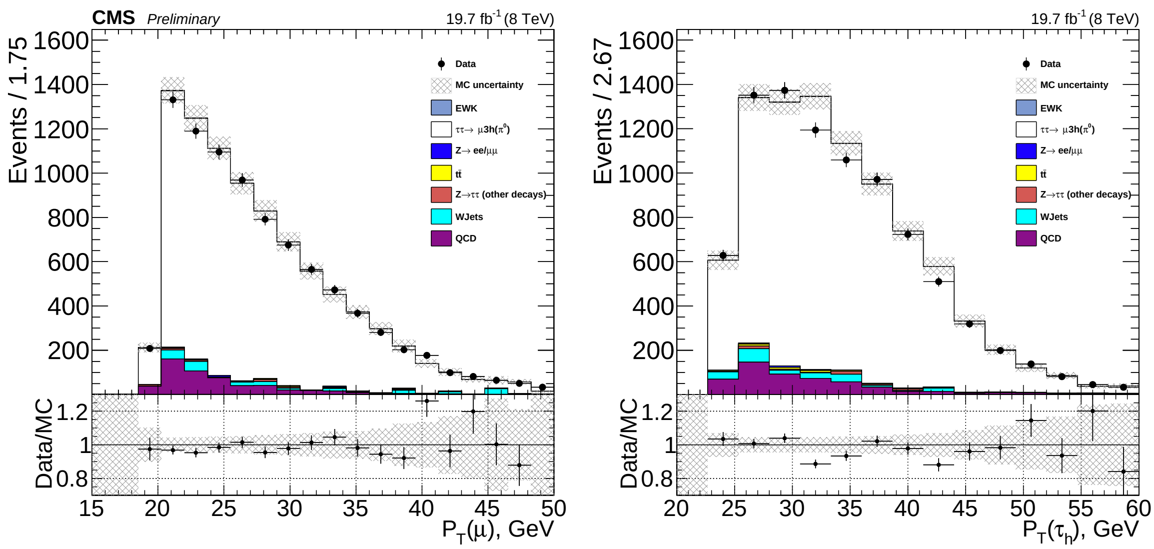

Figure 37: Transverse momentum, p_T, of the selected muon (*Right*) and visible transverse momentum of the selected τ_h candidate (*Left*) .

Chapter 8

Kinematic Reconstruction of $Z \rightarrow \tau\tau$ events

In every τ decay at least one neutrino is present in the final state which escapes detection. Hence, the reconstruction of the whole kinematic of the τ decay is a challenging task. However, it is possible to recover the missing momentum for both τ leptons and thus the full event kinematic in the final state $Z \rightarrow \tau\tau \rightarrow \mu\nu\nu, a_1\nu$. For this purpose a Global Event Fit (GEF) has been developed. The description of the algorithm and its performance is given in this chapter.

The general procedure is subdivided into three steps.

1. The reconstruction of the primary vertex (PV) and the secondary vertex (SV) of the hadronically decaying τ.
2. The calculation of the τ momentum in the decay $\tau^- \rightarrow \pi^-\pi^-\pi^+\nu_\tau$.
3. The reconstruction of the momentum of both tau leptons by applying a kinematic fit with constraints on the di- τ system.

8.1 Primary Vertex

The primary vertex of the event is re-fit using the *AdaptiveVertexFitter* after removing the visible decay products from the τ Leptons. This method [54] was developed to reduce the bias on the vertex position created by the decay products of the τ leptons.

8.2 Secondary Vertex

For particle-flow τ leptons, identified as 3-prong τ decay, the 3 charged tracks are used to reconstruct the secondary vertex with the *KalmanVertexFitter* [55] program.
The momentum of the a_1 resonance is obtained as the sum of the momenta of the three pions. With the knowledge of both vertices the flight direction of the τ lepton is determined as $\hat{p} = \frac{\vec{SV}-\vec{PV}}{|\vec{SV}-\vec{PV}|}$. In Fig. 38 the pull distributions of the secondary vertex x coordinate and of the flight length, respectively, are shown. The distributions for y and z coordinates are similar to one for x. Good agreement with the expected normal Gaussian distribution is found.

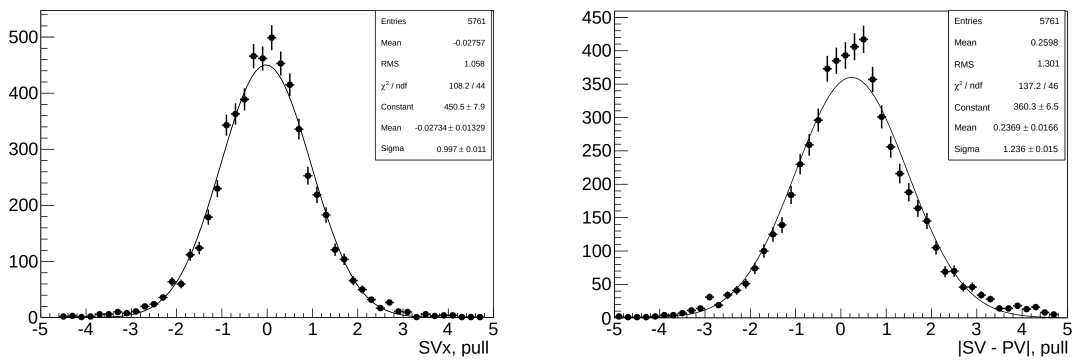

Figure 38: The pull distributions of secondary vertex x component (*Left*) and the decay length (*Right*).

8.3 Calculation of the τ momentum in the decay $\tau \longrightarrow a_1\nu$

Since the decay $\tau \rightarrow 3\pi^{\pm} + \nu_\tau$ is a two-body decay to a_1 and ν_τ, the momentum of the τ lepton can be calculated using energy and momentum conservation. Assuming the neutrino to be massless, in the laboratory frame holds:

$$(P_\tau - P_{a_1})^2 = 0, \tag{8.1}$$

where P_τ and P_{a_1} are the four-momenta of the τ lepton and the a_1, respectively. The τ momentum reads then:

$$|\vec{p}_\tau| = \frac{(m_{a_1}^2 + m_\tau^2)|\vec{p}_{a_1}|\cos\theta_{GJ} \pm \sqrt{(m_{a_1}^2 + \vec{p}_{a_1}^2)[(m_{a_1}^2 - m_\tau^2)^2 - 4m_\tau^2\vec{p}_{a_1}^2\sin^2\theta_{GJ}]}}{2(m_{a_1}^2 + \vec{p}_{a_1}^2\sin^2\theta_{GJ})}. \tag{8.2}$$

The Gottfried-Jackson angle θ_{GJ} is defined as the angle between the directions of the τ lepton and the a_1 in the laboratory frame. For a given θ_{GJ} and momentum of the a_1 two values for the τ momentum are possible. This ambiguity vanishes if the square root in Eq. (8.2) is zero, it happens if the Gottfried-Jackson angle θ_{GJ} reaches its maximum allowed value θ_{GJ}^{max};

$$\begin{aligned} &(m_{a_1}^2 + \vec{p}_{a_1}^2)[(m_{a_1}^2 - m_\tau^2)^2 - 4m_\tau^2\vec{p}_{a_1}^2 sin^2\theta_{GJ}] = 0; \\ &\theta_{GJ}^{max} = arcsin\frac{m_\tau^2 - m_{a_1}^2}{2m_\tau|\vec{p}_{a1}|}. \end{aligned} \tag{8.3}$$

An illustration of the kinematics is given in Fig. 39 (*Left*). The solid curve shows the value of the τ momentum as a function of θ_{GJ}. For a given value of θ_{GJ} the two solutions of Eq. (8.2) are denoted as positive and negative for the higher and lower value of the τ momenta, respectively. The ambiguity point corresponds to the τ momentum at θ_{GJ}^{max}.

The τ leptons produced in Z decays are strongly boosted leading to very small values for θ_{GJ}. Hence the measured value of θ_{GJ} is very sensitive to even small shifts in the primary and secondary vertex positions. Without additional quality criteria on the separation between the

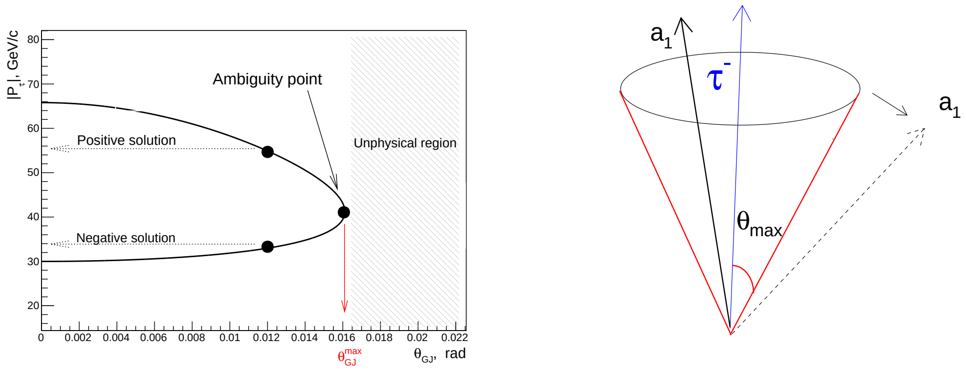

Figure 39: *Left*: The calculated tau momentum in the $\tau \longrightarrow a_1\nu$ with: $m_{a_1} = 1.2GeV/c^2$ and $p_{a_1} = 30GeV/c$. The range of allowed θ_{GJ} is limited by its maximal value indicated as Ambiguity point. *Right*: The rotation of τ cone in the case of unphysical value of θ_{GJ} in order to approach the ambiguity point.

primary and the secondary vertex, approximately 40% of the decays populate the unphysical region shown by the shaded area in Fig.39 (*Left*). Rejecting events of the unphysical region or applying stronger quality criteria would lead to a significant loss of statistics. A recovery of these events is, however, possible by moving the decay topology from the forbidden region to the ambiguity point as shown in Fig. 39 (*Left*). Geometrically this means a rotation of the τ decay cone towards the a_1 direction until θ_{GJ} approaching θ_{GJ}^{max}, as illustrated in Fig.39 (*Right*). The τ momentum in Eq. (8.2) is then also shifted deteriorating slightly the momentum resolution for these events.

The ambiguity in the τ momentum for events with $\theta_{GJ} < \theta_{GJ}^{max}$ is solved exploiting the whole event kinematics, as described in the next section.

8.4 Reconstruction of $Z \longrightarrow \tau\tau \longrightarrow \mu\nu\nu, 3\pi\nu$ final state.

A mathematical framework for kinematic fits using the least mean squares method with Lagrange multipliers is used. Since the τ leptons originate from Z boson decays the following constraints are applied:

1. Invariant mass of the τ leptons to be equal to M_Z
2. Transverse momentum balance of both τ leptons taking into account a possible transversal boost of the Z boson.
3. Angular constraints on the τ leptons directions, derived from the measured momenta of the decay products and positions of the SV and PV.

The angular constraints are schematically shown in Fig. 40. The indices 1 and 2 correspond to the decays $\tau \longrightarrow a_1\nu$ and $\tau \longrightarrow \mu\nu\nu$, respectively. The angle ϕ_2 is estimated as $\phi_2 = \pi + \phi_1 + \delta\phi$. The correction term $\delta\phi$ is introduced to account for the boost of the Z boson in the transversal plane and is used to estimate the starting point of the τ leptons kinematic for the fit. There are two alternative ways to estimate $\delta\phi$.

- If the Z boson is boosted then the neutrinos from τ decays are not flying back-to-

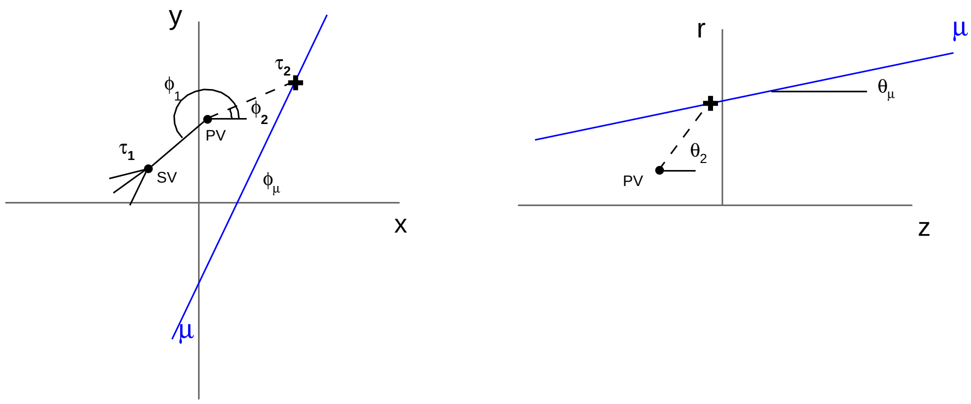

Figure 40: *left* The projection of the decay topology on the transversal plane. *right* The projection of the decay topology on the rz plane. PV is the primary vertex and SV the secondary vertex of the τ 1 decay. The angles ϕ_1 and ϕ_2 are the azimuthal angle of the flight direction of the τ_1 and τ_2. ϕ_μ is the azimuthal angle of the muon. θ_μ and θ_2 are the polar angles of the muon and the tau lepton in the the decay $\tau \rightarrow \mu\nu\nu$. The black solid cross indicates the decay point of τ_2.

back but tend to move in the same direction, and thus $\delta\phi$ can be estimated from the direction of the missing transverse energy. Fig. 41 shows the correlation between the generated and the reconstructed value of the ϕ angle of the Z boson direction of flight.

- The other approach is to use the sum of the momenta of all particles originating from the primary vertex, $\vec{P} = \sum\limits_{tracks} \vec{p}$. The direction of $\vec{P}$ in the transversal plane also shows a correlation with generated transversal direction of Z the boson.

Both methods was studied and showed similar performance. The approach using the missing transverse energy was given preference.

Due to the large track radius of the selected muons in the CMS magnetic field their bending is neglected and the muon track is approximated by a straight line .

The decay point of τ_2 is estimated as the intersection of the muon track and the direction of τ_2 given by the dashed line in Fig. 40 (*Left*). The corresponding z coordinate and accordingly the polar angle θ_2 are determined by projecting the decay topology onto the r-z plane, as shown in Fig.40 (*right*). The flight direction of the τ_2 in the r-z plane is shown as the dashed line between the primary vertex and the point where the muon track crosses the flight direction of the τ_2. The angle θ_2 is used as an estimate for the τ_2 flight direction in the r-z plain.

The Lagrange function is defined as follows:

$$L = (\vec{y} - \vec{a})^T \boldsymbol{V}_y^{-1} (\vec{y} - \vec{a}) + \vec{f}^T(\vec{a}, \vec{b}) \boldsymbol{V}_f^{-1} \vec{f}(\vec{a}, \vec{b}) + 2\vec{\lambda}^T \vec{H}(\vec{a}, \vec{b}) \tag{8.4}$$

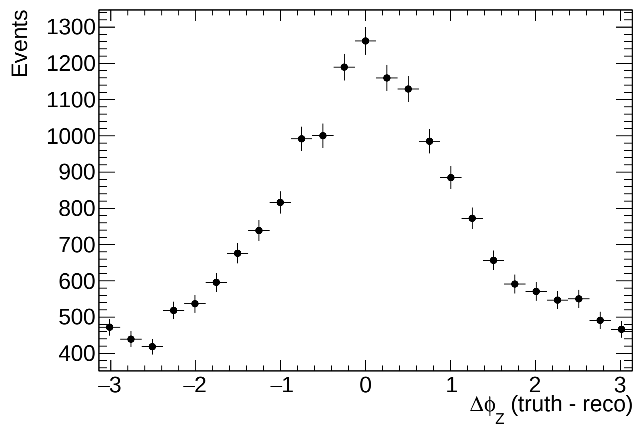

Figure 41: The difference between the generated and reconstructed azimuthal angle of the Z boson direction of flight.

The first term describes only the parameters of τ_1. The vector $\vec{y} = (p_x, p_y, p_z)$ comprises the measured parameters of τ_1 as determined in Chapter (8.3) and $\boldsymbol{V}_y$ is the covariance matrix of the parameters in $\vec{y}$. The vectors $\vec{a}$ and $\vec{b}$ comprise the post-fit momenta of τ_1 and τ_2. The parameters for the τ_1 and τ_2 must match the constraints, which are separated into two parts - the so-called soft $\vec{f}(\vec{a}, \vec{b})$ and hard $\vec{H}(\vec{a}, \vec{b})$ constraints. The matrix $\boldsymbol{V}_f$ comprises the joint covariance matrix of parameters $\vec{a}$ and $\vec{b}$ propagated through the functions $\vec{f}$. The quantity $\vec{\lambda}$ represent the Lagrange multipliers.

The momentum of the τ_1 and the τ_2, are obtained by minimizing L from the Eq. (8.4) with respect to vectors $\vec{a}, \vec{b}$ and $\vec{\lambda}$ as described in Appendix D.

8.5 Constraints

The explicit view of the constraints discussed above is given in this section. The constraints on the invariant mass of the di-τ system and on the longitudinal momentum component of the τ_2 are introduced as hard constraints $\vec{H} = 0$, i.e.:

$$\vec{H} = \begin{cases} M_{\tau\tau} - M_Z \\ p_z - |\vec{p}_2| cos\theta_c \end{cases} \tag{8.5}$$

where M_Z is the mass of the Z boson, $M_{\tau\tau}$ the invariant mass of di-tau system, p_z and $|\vec{p}_2|$ are the longitudinal component and the total momentum of τ_2. There are two options for the constraint on the polar angle θ_c of τ_2:

1. θ_c = θ_2 as described in Fig. 40 (*Right*)

2. Set θ_c to be equal to the polar angle of the muon, θ_μ, taking into account that the tau leptons in the decay of the Z boson are highly boosted and consequently the decay products are collimated in a small cone around the τ lepton flight direction.

The first approach is more physical but leads to some numerical instability during the minimization. The second is more stable, and was chosen in this work. However, it should be noted that the angle between the muon and the τ_2 carries the information on the helicity state of τ_{2u} which is lost if $\theta_c = \theta_\mu$.

In order to account for the transversal boost of the Z boson, the soft constraint term $\vec{f}$ is defined as:

$$\vec{f} = \left\{ \begin{array}{l} p_x^{\tau_1} + p_x^{\tau_2} - p_x^{a_1} - p_x^{\mu} - MET_x \\ p_y^{\tau_1} + p_y^{\tau_2} - p_y^{a_1} - p_y^{\mu} - MET_y \end{array} \right\} \tag{8.6}$$

Here $\vec{p}^{\tau_1}$, $\vec{p}^{\tau_2}$, $\vec{p}^{a_1}$, $\vec{p}^{\mu}$ are the momenta of the τ leptons, the a_1 and the muon, respectively, and MET_x and MET_y are the x and y components of the missing transverse energy MET.

8.6 Global Event Fit performance

The efficiency and the resolution of the relevant parameters of the τ leptons kinematics determine the performance of the whole algorithmThe efficiency is defined as the probability that an event passes all the steps to reconstruct the $Z \to \tau\tau \to \mu\nu\nu, a_1\nu$ final state. It has been studied using a Monte Carlo sample of the $Z \to \tau\tau$ decays.

The efficiencies as a function of transversal momenta, the pseudorapidities and the polar angles of the a_1 and the μ, respectively, are shown in Fig. 42. As can be seen, they are almost flat and at a reasonable level of about 90%.

The efficiencies to pass the event fit for the hadronic τ decays $3\pi\nu$, $3\pi\pi^0\nu$, $KK\pi\nu$, $K\pi\pi\nu$ is shown in Fig. 44. They amount to roughly the same value. However the decays $\tau \to KK\pi\nu$ and $\tau \to K\pi\pi\nu$ are Cabibbo suppressed and their contribution in the selected sample is only about 2%.

The branching fraction of the $\tau \to 3\pi\pi^0\nu$ decay is approximately half of the one for $\tau \to 3\pi\nu$. Additional criteria will be applied to reduce the contribution from the $\tau \to 3\pi\pi^0\nu$ channel.

The resolution of the kinematic quantity α_i is obtained from the distribution of the difference between the generated and reconstructed value $\Delta\alpha_i = \alpha_i^{gen} - \alpha_i^{reco}$. The transversal momenta, pseudorapidities and azimuthal angle resolutions, respectively, for both τ leptons are shown in Fig. 43. The Gaussian width of the p_T resolution for both τ leptons is of about 6 GeV. The η and ϕ resolutions for the τ lepton in the decay $\tau \to a_1\nu$ ($\tau \to \mu\nu\nu$) are about 0.05 (0.1) and 0.03 rad (0.15 rad). The ϕ resolution for τ_2 is significantly worse than those of τ_1 mainly due to the presence of 2 neutrinos and less information available on the direction of τ_2.

In order to resolve the ambiguity in the momentum of the tau lepton in the $\tau \to a_1\nu$ decay the global event fit is performed for both values and the one is taken with the smaller value of the minimized function L in Eq. (8.4). The probability to obtain the correct value of the τ momentum and the probability to accept the wrong value is shown in Fig. 45. The negative and positive solutions correspond to the lower and higher momentum, as indicated in Fig. 39 (*Left*).

The Event Fit was used to reconstruct the event kinematic and the angles θ, β and γ described in Chapter 5. The resolution for these three angles and the relative resolution of

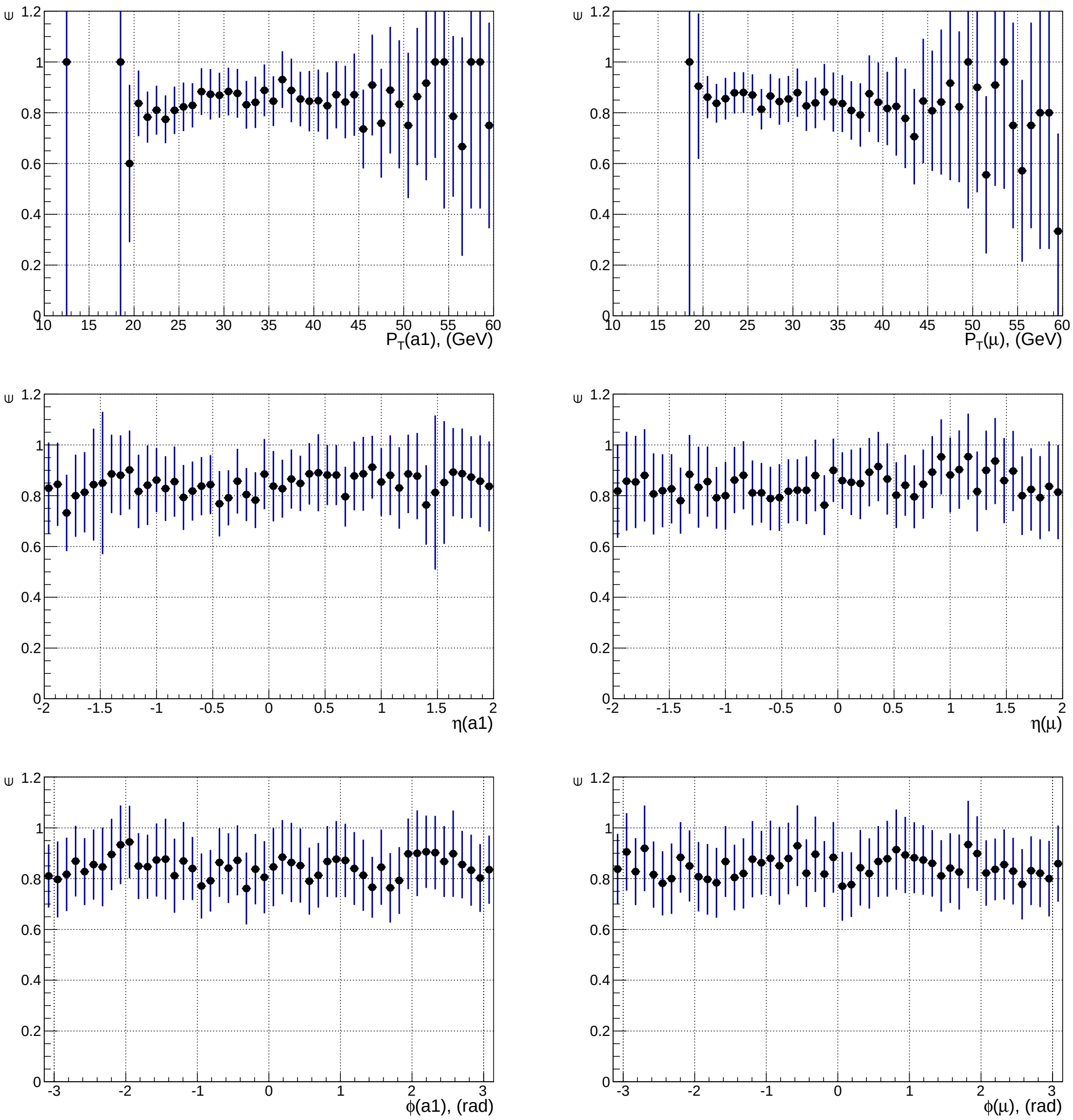

Figure 42: Event Fit efficiency as a function of p_T, η and ϕ of the a_1 and the muon, respectively.

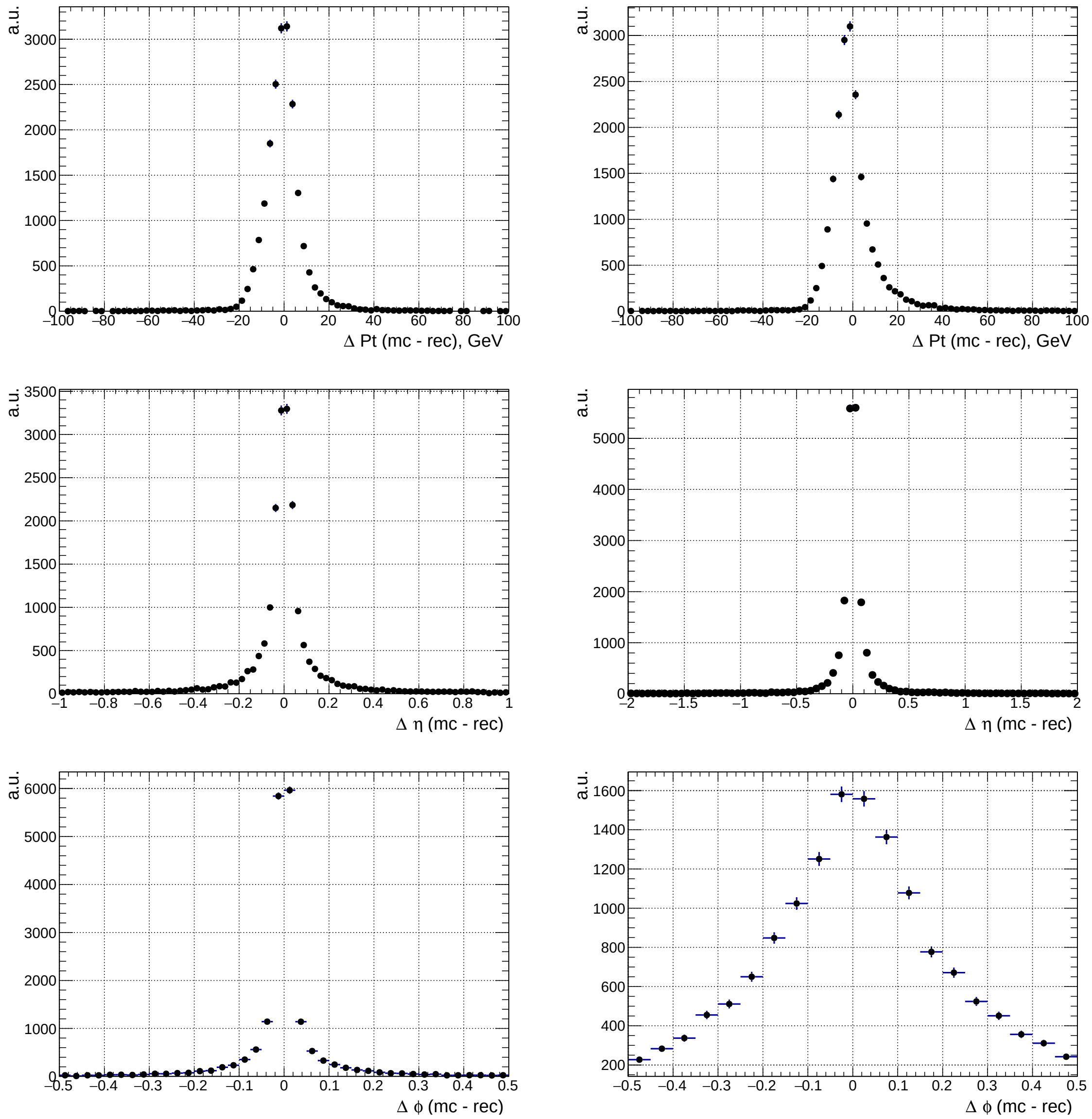

Figure 43: The resolutions in p_T, ϕ and η of the $\tau \to a_1 \nu$ (*left column*) and $\tau \to \mu\nu\nu$ (*right column*) decays.

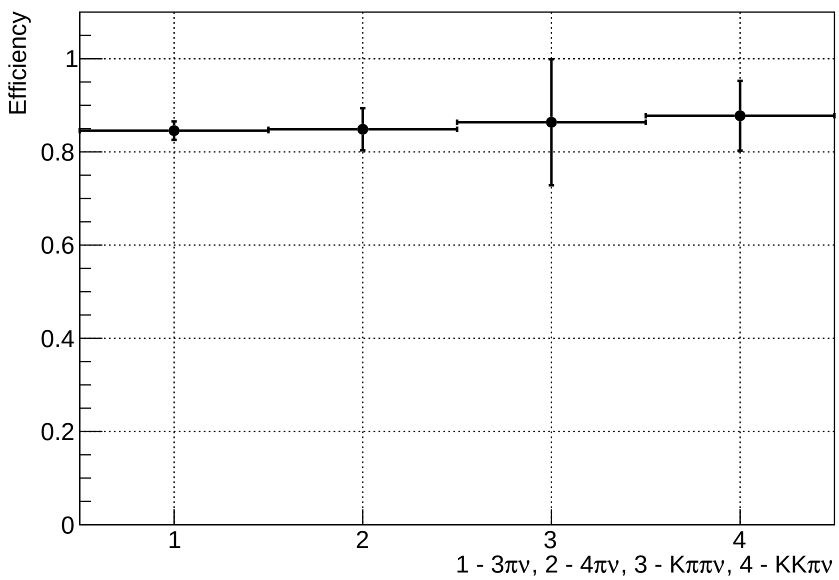

Figure 44: Event Fit efficiency for hadronic decay channels in the selected sample.

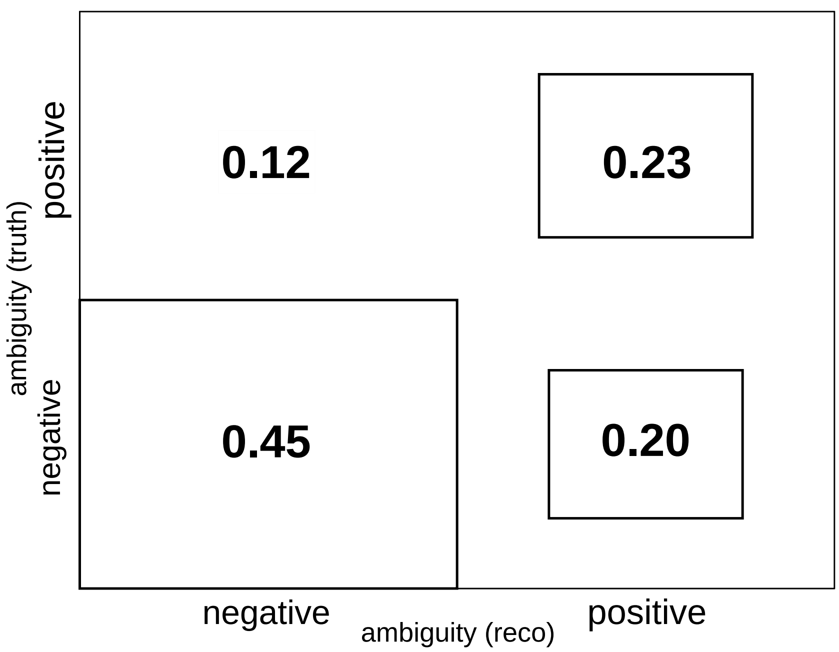

Figure 45: The probability matrix for resolving the kinematical ambiguity in the decay $\tau \to 3\pi\nu$.

reconstruction of variable ω_{a_1} are shown in Fig. 46.

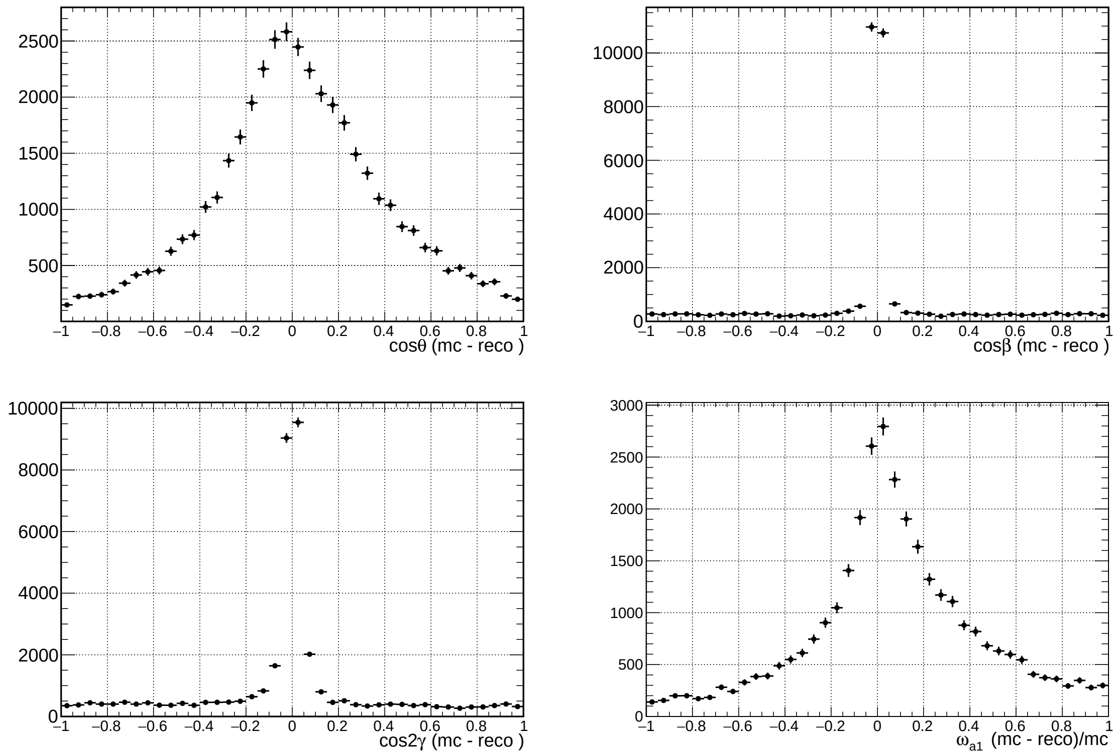

Figure 46: Resolution of angles θ, β and γ, and the relative resolution for the quantity ω_{a_1} in the decay $\tau \to a_1\nu$, reconstructed using Event Fit.

Chapter 9

Measurement

9.1 Measurement of the τ polarization

The τ polarization is measured performing a fit to the distribution of the variable ω_{a_1}, obtained from the data, using two template distributions for τ leptons with helicity $+1$ and -1 obtained from Monte Carlo. The τ polarisation P_τ is the free parameter. The templates are produced using the TauSpinner [49, 56] package to simulate the decay $Z \to \tau\tau$. They are shown in Fig. 47 before and after reconstruction and event selection, respectively. As can be seen, the reconstruction and event selection slightly dilutes the polarisation sensitivity in the distribution of the quantity ω_{a_1}

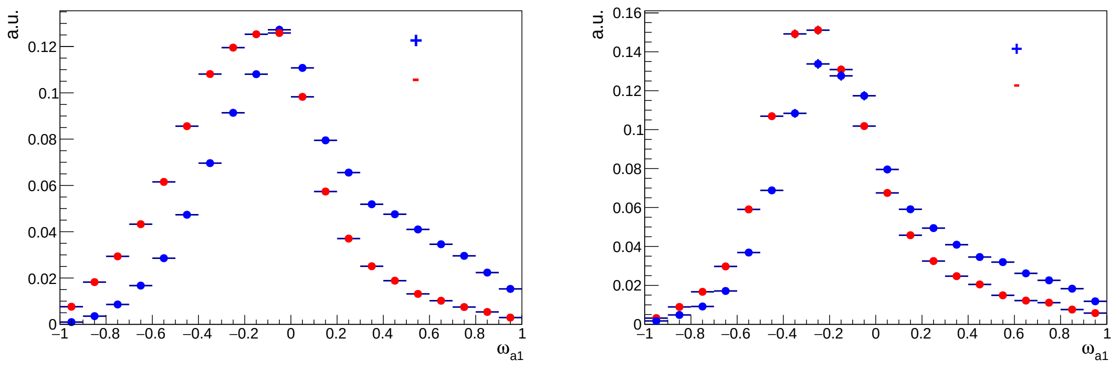

Figure 47: The ω_{a_1} distribution for the τ helicity $h_\tau = +1$ (*blue*) and $h_\tau = -1$ (*red*). *Left*: Using generated events. *Right*: Using reconstructed and selected events.

In addition, templates are produced for non-signal τ lepton decays that passed the selection and added to the corresponding templates shown in Fig. 47. The probability per bin i is constructed as:

$$\mathcal{P}[i] = \frac{e^{-T_i}(T_i)^{N_i}}{N_i!} \times \frac{e^{-\mu b_i}(\mu b_i)^{B_i}}{B_i!} \times \mathcal{G}(p|p_0, \sigma_p) \tag{9.1}$$

The first term in Equation (9.1) refers to the probability to observe N_i events in data for a given expected value T_i. The second term is included in order to account for the finite Monte Carlo statistics in the background templates. The last Gaussian term accounts for the uncertainty on the background normalization.

The values of T_i are obtained from the linear combination of the template contribution per bin;

$$T_i(P_\tau) = N_{sig}[(\frac{1-P_\tau^{obs}}{2})\frac{h_i^L}{H^L} + (\frac{1+P_\tau^{obs}}{2})\frac{h_i^R}{H^R}] + pb_i, \quad (9.2)$$

where N_{sig} is the estimated number of the signal events and b_i the estimated background. H^L and H^R are the Monte Carlo normalizations of the templates, $\sum\limits_{bins} \frac{h_i^{L,R}}{H_i^{L,R}} = 1$. The signal components with helicity $+1$ and -1, h^R, h^L are weighted with the parameter P_τ^{obs}, being the observed average τ polarization. The parameter p describes the background normalisation and is left as a free parameter.

The values for B_i are taken without scaling to the integrated luminosity from the Monte Carlo samples, the factor μ is the scaling factor of the actual value of B_i to the estimated value b_i. However, the expected values b_i are unknown and therefore the probability (9.1) is integrated over the all possible values of b_i:

$$d_i = \int_0^\infty \mathcal{P}[i] db_i. \quad (9.3)$$

The integration can be performed analytically[1] and the likelihood function to be minimized is then:

$$\mathcal{L} = \prod_i d_i. \quad (9.4)$$

The different kinematics of the τ lepton decay products with helicities ±1 results in different selection and reconstruction efficiencies. Labeling with ϵ_+ and ϵ_- the efficiencies of the selection and reconstruction for right-handed and left-handed τ leptons, the observed value for the τ polarization, P_τ^{obs} is expressed as[2]:

$$P_\tau^{obs} = \frac{\epsilon_r - \frac{1-P_\tau^{true}}{1+P_\tau^{true}}}{\epsilon_r + \frac{1-P_\tau^{true}}{1+P_\tau^{true}}}, \quad (9.5)$$

where $\epsilon_r = \frac{\epsilon_+}{\epsilon_-}$. This ratio has been determined from Monte Carlo samples to be $\epsilon_r = 0.612$. The quantity P_τ^{true} is the "true" τ lepton polarization, it is a free parameter and obtained from the minimization of (9.1).

The fit is performed in the range -1 $< \omega_{a_1} <$ 1 with a bin width $\Delta\omega_{a_1} = 0.1$. The ω_{a_1} distribution for the events selected in data, the both helicity states, background and the best fit Monte Carlo distributions are shown in Fig. 48.

The value of the τ polarization obtained from the fit is $< P_\tau^{true} >= -0.1261 \pm 0.0730$.

[1]An easy way to perform the integration is to use the following relations: $(a+b)^n = \sum\limits_{k=0}^{n} \frac{n!}{k!(n-k)!} a^{n-k} b^k$, $\int\limits_0^\infty x^{z-1} e^{-x} dx = z!$

[2]This can be derived from the definition of polarization $P_\tau = \frac{N_+ - N_-}{N_+ + N_-}$.

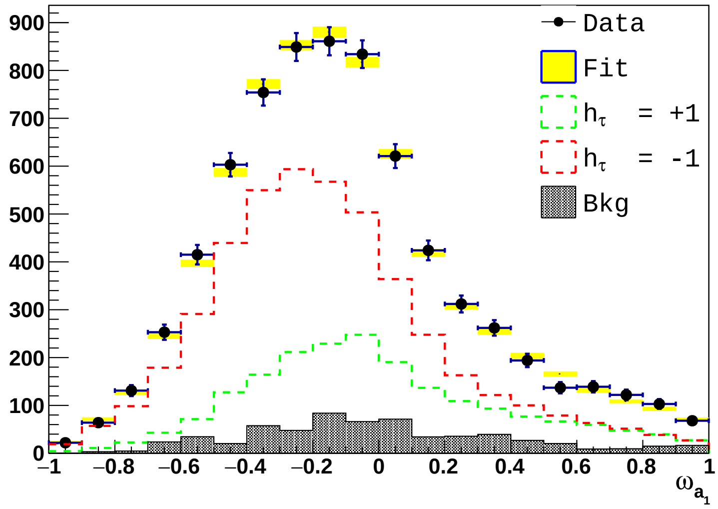

Figure 48: The distribution of ω_{a_1} in data, for the two tau helicities from Monte Carlo and from the background, and the result of the fit for the observed polarisation P_τ^{obs}.

The error is estimated varying the value for $< P_\tau >$ corresponding to a change of 0.5 in $ln\mathcal{L}$. As an assessment of the fit quality the χ^2 per degree of freedom is calculated using only the statistical uncertainty in the data. With 18 degrees of freedom the resulting value is χ^2/ndf = 0.76. The value of the background normalization is obtained as p = 0.99$\pm$ 0.09.

9.2 Systematic Uncertainties

Various systematic effects have been studied that affect the shape or overall normalization of the simulated signal and background templates for variable ω_{a_1} used to extract the τ polarization value. For each type, new templates are produced and fit to the data. The uncertainty on P_τ is taken as a difference between the fit result obtained with the default and the new templates.

- The number of interactions per bunch crossing in data in data is estimated from the measured luminosity in each bunch crossing times the average cross section, therefore there are two sources of uncertainties for the pileup simulation. According to the recommendations for 2012 data, the pileup weight applied to each event is varied by $\pm$ 5% around the central value. The difference between results is treated as a systematic uncertainty. The obtained value is ΔP_τ = 0.006.

- The systematic uncertainty arising from imperfect knowledge of the background is estimated by varying the corresponding nuisance parameter in Eq. (9.1) by $\pm$ 8% and fixing it during the minimization. The value of 8% is taken from the statistical uncertainty of the two major background sources, QCD and W+Jets. The systematic uncertainty due to the uncertainty in the EWK background is negligible. The obtained value for the uncertainty on polarization is found to be $\Delta P_\tau = {}^{+0.007}_{-0.009}$.

- As described in section 7.4 the corrections are applied to the muon momentum.

The systematic uncertainty related to the muon momentum scale is found to be negligible.

- In order to evaluate the uncertainty on trigger and ID the normalization uncertainties of 2% from muons and 6% for taus have been applied. The resulting value for the uncertainty on tau polarization is ΔP_τ = = $\pm$ 0.003(2).

The theoretical uncertainty from the model dependence includes the following effects: the variation of a_1 parameters, e.g. mass, width, the effect of different theoretical models, [57–59], the different treatment of the D- and S- wave contribution in the $\rho\pi$ intermediate state of the a_1, the effect of the scalar contribution in the final 3π state originating from $\pi'(1300)$. These uncertainties have been studied in Ref. [35], a conservative estimate $\Delta P_\tau^{theor} = \pm 0.015$ is given.

The summary on systematic uncertainties is given in Table. 9.1

Table 9.1: Summary of the systematic uncertainties in P_τ

Uncertainty type	Value
Pileup	0.006
Muon momentum scale	0.000(05)
TauID/Trigger	0.003(2)
Bkg. estimation	$^{+0.007}_{-0.009}$
a_1 decay model	0.015
Total	$^{+0.018}_{-0.019}$

9.3 Determination of $\sin^2\theta_{eff}$

The τ polarization $P_\tau(s)$ and the cross section $\sigma(s)$ can be expressed in terms of the structure functions from Eq. (2.35):

$$\begin{aligned} \sigma_q &= \frac{16}{3} F_0^q(s), \\ P_\tau^q(s) &= -\frac{F_2^q(s)}{F_0^q(s)}, \end{aligned} \tag{9.6}$$

where label q denotes the flavour of the initial quark anti-quark pair in the process $q\bar{q} \to Z \to \tau\tau$.

The τ polarization averaged over the center-of-mass energy of the τ pair can then be expressed in terms of the total cross section $\hat{\sigma}$ and τ polarization, $\hat{P}_\tau$, the average over the initial quarks flavour as:

$$< P_\tau >= \frac{\int \hat{P}_\tau(x)\hat{\sigma}(x)\epsilon(x)dx}{\int \hat{\sigma}(x)\epsilon(x)dx}, \tag{9.7}$$

where $x = \sqrt{s}$ of the τ pair and $\epsilon(x)$ is the acceptance as shown in Fig. 49. The τ polarization as a function of $\sqrt{s}$ for the case of initial quarks be $u\bar{u}(c\bar{c})$, $d\bar{d}(s\bar{s}$,$b\bar{b})$ and the averaged $\hat{P}_\tau(s)$

are shown in Fig. 7. The value of $\hat{\sigma}(x)$ is calculated as described in Eq. 3.6, $\hat{P}(s)$ is averaged over parton cross sections as:

$$\hat{P}_\tau(s) = \frac{\alpha P_\tau^{u,c}(s)\sigma_{u,c}(s)}{\alpha\sigma_{u,c}(s) + (1-\alpha)\sigma_{d,s,b}(s)} + \frac{(1-\alpha)P_\tau^{d,s,b}(s)\sigma_{d,s,b}(s)}{\alpha\sigma_{u,c}(s) + (1-\alpha)\sigma_{d,s,b}(s)}, \tag{9.8}$$

The factor α in Eq. 9.8 describes the relative contribution of u/c quarks in the Z formation and is calculated using the PDFs described in Chapter 3.

In order to evaluate the EWK radiative corrections for $\hat{\sigma}(s)$ and $\hat{P}_\tau(s)$ the values of σ_q and P_τ^q, the cross section and τ polarization for a given flavour q of initial quarks, are calculated using the ZFitter program [10]. The ZFitter package was developed to calculate the radiative corrections, as predicted in the Standard Model, to a variety of observable quantities, related to the Z-boson resonance produced in e^+e^- collisions, however by changing the relevant parameters it is modified to calculate the quantities of interest for the Z boson produced in the annihilation of $q\bar{q}$. This was verified by comparison of the analytically calculated $P_\tau(s)$ shown in Fig. 7 to the tree-level calculation provided by ZFitter.

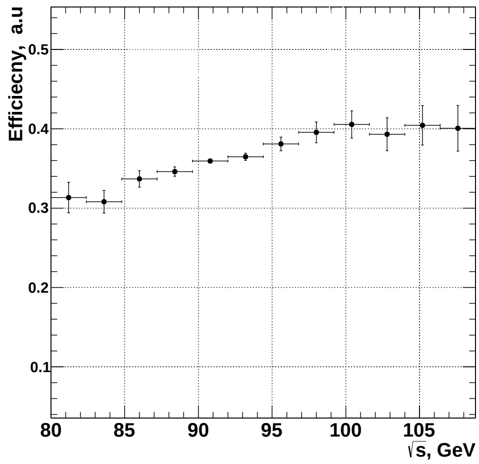

Figure 49: The efficiency to select $\tau^+\tau^-$ as a function of $\sqrt{s}$.

The calculation of the average polarization (9.7) is performed for 11 values of $\sin^2\theta_{eff}$ in the range of 0.20-0.25 using ZFitter. The value of the measured average polarization as well as its uncertainty is then propagated to the value of the effective mixing angle as shown in Fig. 50. The resulting value is:

$$\sin^2\theta_W = 0.2336 \pm 0.0096. \tag{9.9}$$

In order to directly compare to LEP results and also for the consistency check we perform the propagation for the measured average polarization $< P_\tau >$ to the value at the peak $P_\tau(M_Z)$ as shown in Fig. 51. The obtained value is $P_\tau(M_Z) = -0.1301 \pm 0.0760$.

The effective vector and axial-vector couplings can be expressed in terms of an effective weak mixing angle $\sin^2\theta_{eff}$ as:

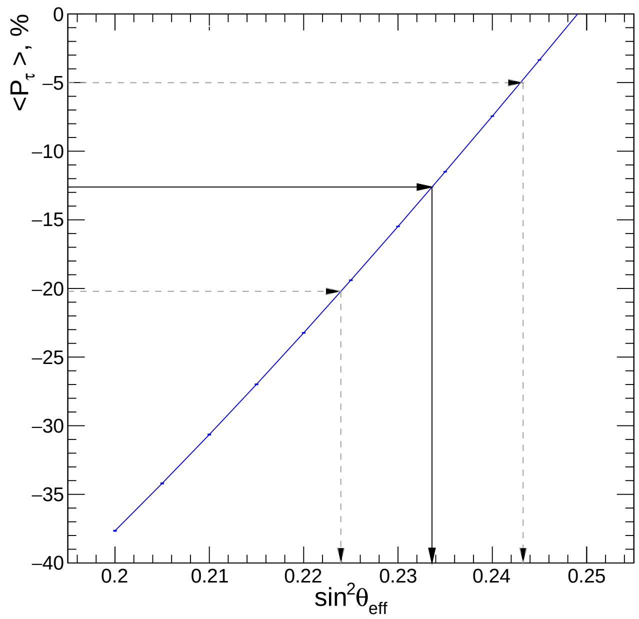

Figure 50: The average τ polarization as a function of the weak mixing angle.

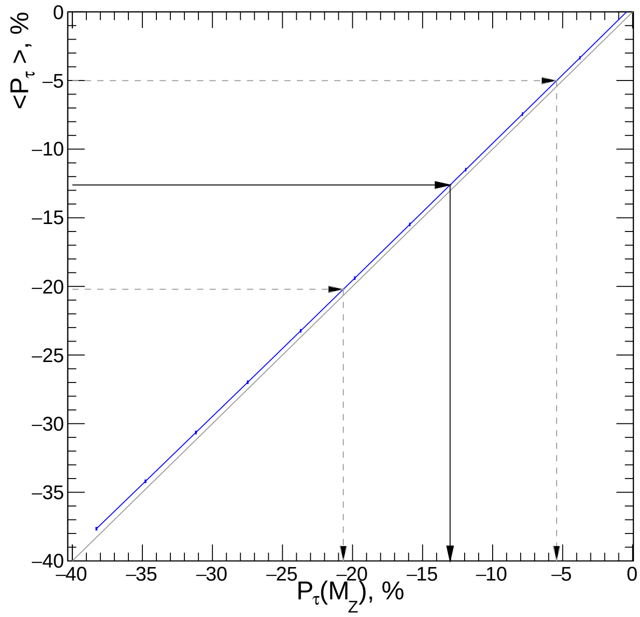

Figure 51: The average τ polarization $< P_\tau >$ as a function of $P_\tau(M_Z)$. The gray straight line corresponds to the case $< P_\tau >= P_\tau(M_Z)$.

$$\frac{\bar{v}_\tau}{\bar{a}_\tau} = 1 - 4|Q_\tau| \sin^2 \theta_{eff} \tag{9.10}$$

Combining the equations (2.44), (9.10) and using our value for the polarization at the Z pole we obtain for the $\sin^2\theta_{eff} = 0.2337 \pm 0.0095$, which is in a good agreement with (9.9).

A comparison between the $\sin^2\theta_{eff}$ result obtained in this analysis and those from other experiments is shown in Fig. 52. The result is in agreement with other measurements within the uncertainty.

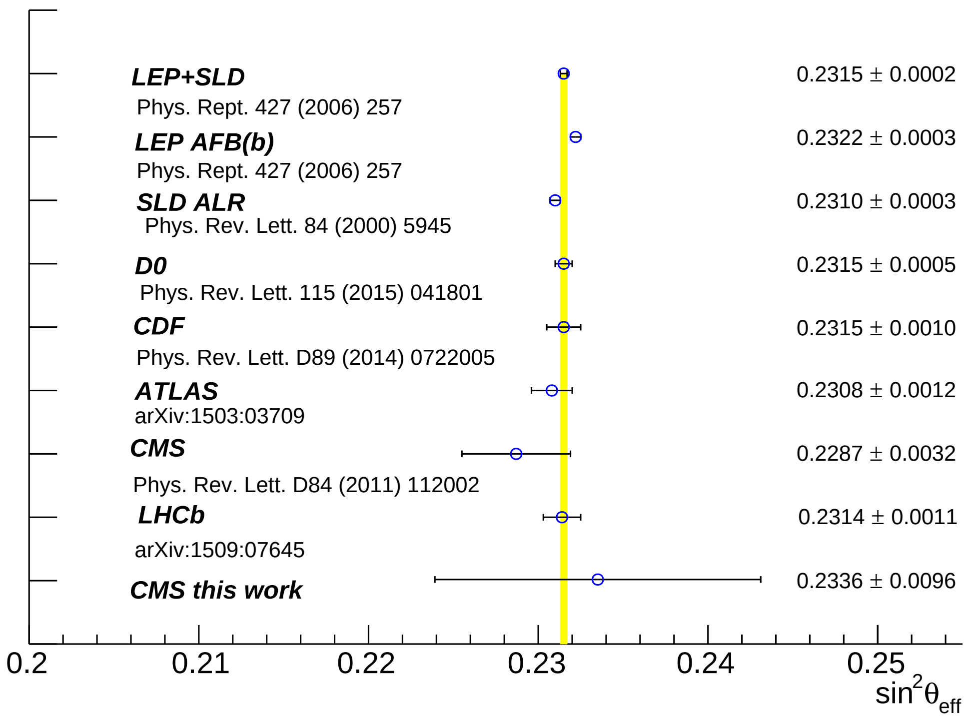

Figure 52: A comparison of the $\sin^2\theta_{eff}$ in τ polarization at CMS and other experiments. The combined LEP and SLD measurement is indicated be the yellow band.

Chapter 10

Conclusions

In this thesis the τ lepton polarization in the process $pp \to Z^0 \to \tau^+\tau^-$ was measured using the τ decay into three charged pions produced from the decay of the a_1 resonance. The result is obtained from 19.6 fb^{-1} of proton-proton collision data corresponding to a luminosity of 19.6 fb^{-1} collected by the CMS detector in 2012 at 8 TeV center-of-mass energy. Using 8812 selected events of the decay $Z \to \tau\tau \to \mu\nu\nu, a_1\nu$, the average τ polarization is measured to be:

$$< P_\tau >= -0.1261 \pm 0.073(stat)^{+0.018}_{-0.019}(syst). \tag{10.1}$$

From the value of the averaged τ polarization the effective weak mixing angle is derived:

$$\sin^2\theta_W = 0.2336 \pm 0.0096. \tag{10.2}$$

Using Eq. (9.10) we also derive the ratio of vector to axial-vector neutral current couplings for τ leptons:

$$g_V^\tau/g_A^\tau = 0.0656 \pm 0.0384. \tag{10.3}$$

This is the first measurement of the τ lepton polarization at the LHC. The results are in agreement with previous measurements.

A larger data sample will allow to reduce the statistical uncertainty and detector related systematic uncertainties. The systematic uncertainty on the a_1 model can also be improved by using more recent models [60] that exploit data from CLEO and BaBar in the fit of a_1 parameters.

The statistical uncertainty can also be reduced by improving the sensitivity of the optimal observable ω_{a_1}. The Global Event Fit described in Chapter 8 provides the full event kinematic and hence an access to all polarization sensitive variables. The angle α, discussed in Chapter 5[1] was not considered in this analysis, however, in Ref. [33] authors noted than even the modest precision of the reconstruction of the angle α can provide a sizable improvement in the sensitivity of variable ω_{a_1}.

This measurement can be performed using other τ decay modes. In the channel $l\nu\nu/\rho\nu$ only the angle ψ in the ρ rest frame between the axis defined by the ρ^- flight direction and π^-

[1] An angle between the plane made by τ direction and the direction of the laboratory system and the plane made by τ direction and normal vector to the three pions plane.

flight direction can be used. This angle is similar to the angle β in the a_1 decay mode. Using the Global Event Fit in the channel $\rho\nu$, $\pi\nu/a_1$ has twofold benefit. Firstly, both τ legs can be analyzed, and secondly, exploiting the knowledge of the full kinematic, the angle θ in the decays $\tau \to \rho\nu$ and $\tau \to \pi\nu$ can be reconstructed. The situation is the same in $a_1\nu/a_1\nu$ decay modes, but here better performance of the event fit can be expected due to the knowledge of flight direction of both τ leptons. The multijet background in this decay mode can be kept at reasonably low level by applying a cut on the flightlenght of both τ leptons.

Appendix A

The cross section of the process $q\bar{q} \longrightarrow Z^0 \longrightarrow \tau^+\tau^-$

The tree level diagrams for τ pair production in pp collisions are shown in Fig. 53.

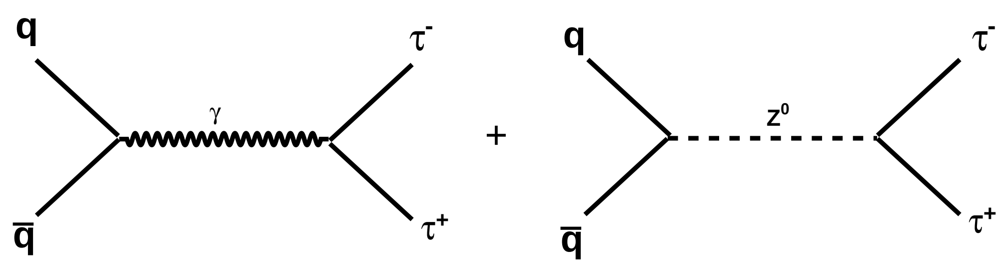

Figure 53: Feynman diagrams for the τ pair production through the photon and Z^0 exchange.

With the strength of vertices according to the SM:

- $q\gamma q$: $-iq_q\gamma^\mu$
- $\tau\gamma\tau$: $-iq_\tau\gamma^\mu$
- qZ^0q: $-ig_Z\gamma^\mu(v_q - a_q\gamma^5)$
- $\tau Z^0\tau$: $-ig_Z\gamma^\mu(v_\tau - a_\tau\gamma^5)$

The matrix element is written as the sum of two contributions shown in Fig. 53:

$$|M|^2 = |M_\gamma + M_Z|^2 = |M_\gamma|^2 + |M_Z|^2 + 2ReM_\gamma M_Z. \tag{A.1}$$

Equation (A.1) can be rewritten in terms of Dirac spinors according to Feynman rules:

$$\begin{aligned} M =& e_q e_\tau [\bar{v}(\bar{q})\gamma^\mu u(q)]\frac{g_{\mu\nu}}{s}[\bar{u}(\tau^-)\gamma^\nu v(\tau^+)]+ \\ & g_Z^2[\bar{v}(\bar{q})\gamma^\mu(v_q - a_q\gamma^5)u(q)]\frac{g_{\mu\nu} - p_\mu p_\nu/M_Z^2}{s - M^2 + is\frac{\Gamma_Z}{M_Z}}[\bar{u}(\tau^-)\gamma^\nu(v_\tau - a_\tau\gamma^5)v(\tau^+)]. \end{aligned} \tag{A.2}$$

Here $s = (p(q) + p(\bar{q}))^2$ and $\frac{g_{\mu\nu} - p_\mu p_\nu / M_Z^2}{s - M^2 + is\frac{\Gamma_Z}{M_Z}}$ is the propagator of Z^0, M_Z and Γ_Z are respectively mass and widths of the Z^0, $g_Z = \frac{e}{\sin\theta_W \cos\theta_W}$. The problem can be simplified noting that only four amplitudes have to be calculated: $M_{LR\to LR}$, $M_{RL\to RL}$, $M_{RL\to LR}$ and $M_{LR\to RL}$, where the indices below indicate the helicity state of initial quarks and final łeptons. In the massless limit of initial and final particles $\sqrt{s} \gg m_q, m_\tau$ and in the rest frame system of virtual γ/Z as shown in Fig. 54 the Dirac spinors in (A.2) can be written as:

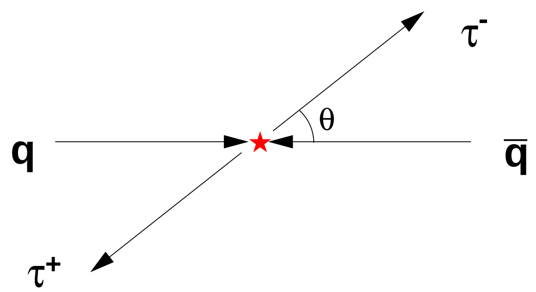

Figure 54: Kinematic of the process in the cm system of $q\bar{q}$.

$$
\begin{aligned}
u_R(\tau) &= \sqrt{E}\begin{pmatrix} c \\ s \\ c \\ s \end{pmatrix} & u_L(\tau) &= \sqrt{E}\begin{pmatrix} -s \\ c \\ s \\ -c \end{pmatrix} \\
v_R(\tau) &= \sqrt{E}\begin{pmatrix} c \\ s \\ -c \\ -s \end{pmatrix} & v_L(\tau) &= \sqrt{E}\begin{pmatrix} s \\ -c \\ s \\ -c \end{pmatrix} \\
u_R(q) &= \sqrt{E}\begin{pmatrix} 1 \\ 0 \\ 1 \\ 0 \end{pmatrix} & u_L(q) &= \sqrt{E}\begin{pmatrix} 0 \\ 1 \\ 0 \\ -1 \end{pmatrix} \\
v_R(\bar{q}) &= \sqrt{E}\begin{pmatrix} 1 \\ 0 \\ -1 \\ 0 \end{pmatrix} & v_L(\bar{q}) &= \sqrt{E}\begin{pmatrix} 0 \\ 1 \\ 0 \\ 1 \end{pmatrix}
\end{aligned}
\tag{A.3}
$$

where $s = \sin\frac{\theta}{2}$, $c = \cos\frac{\theta}{2}$ and θ is the the angle between τ^- and incoming anti-quark. Using the expression for the differential cross-section, $\frac{d\sigma}{d\cos\theta} = \frac{2\pi}{64\pi^2 s}|M|^2$ and evaluating $|M|^2$ using spinors (A.3) one obtains cross section for four non-zero helicity combinations:

$$\begin{aligned}
\frac{d\sigma}{d\cos\theta}(q_L\bar{q}_R \to \tau_L^-\tau_R^+) &= \frac{2\pi\alpha^2(1+\cos\theta)^2}{4s}|q_q q_\tau + (v_q + a_q)(v_\tau + a_\tau)\chi(s)|^2 \\
\frac{d\sigma}{d\cos\theta}(q_R\bar{q}_L \to \tau_R^-\tau_L^+) &= \frac{2\pi\alpha^2(1+\cos\theta)^2}{4s}|q_q q_\tau + (v_q - a_q)(v_\tau - a_\tau)\chi(s)|^2 \\
\frac{d\sigma}{d\cos\theta}(q_R\bar{q}_L \to \tau_L^-\tau_R^+) &= \frac{2\pi\alpha^2(1-\cos\theta)^2}{4s}|q_q q_\tau + (v_q - a_q)(v_\tau + a_\tau)\chi(s)|^2 \\
\frac{d\sigma}{d\cos\theta}(q_L\bar{q}_R \to \tau_R^-\tau_L^+) &= \frac{2\pi\alpha^2(1-\cos\theta)^2}{4s}|q_q q_\tau + (v_q + a_q)(v_\tau - a_\tau)\chi(s)|^2
\end{aligned} \tag{A.4}$$

where the function $\chi(s)$ determines the lineshape of the Z^0:

$$\chi(s) = \frac{1}{4\sin^2\theta_W\cos^2\theta_W}\ \frac{s}{s - M_Z^2 + is\frac{\Gamma_Z}{M_Z}} \tag{A.5}$$

It is convenient to write the total cross-section in a form like $A(\cos\theta) + h_\tau B(\cos\theta)$, where h_τ denotes the helicity state of τ^-. From (A.4) the cross-section can be derived as:

$$\frac{d\sigma}{d\cos\theta} = F_0(s)(1+\cos^2\theta) + 2F_1(s)\cos\theta - h_\tau[F_2(s)(1+\cos^2\theta) + 2F_3(s)\cos\theta], \tag{A.6}$$

where $F_i(s)$ are the structure functions describing the energy dependence of the cross section. The are given by:

$$\begin{aligned}
F_0(s) &= \frac{\pi\alpha}{4s}[q_q^2 q_\tau^2 + 2Re\chi(s)q_q q_\tau v_q v_\tau + |\chi(s)|^2(v_q^2 + a_q^2)(v_\tau^2 + a_\tau^2)] \\
F_1(s) &= \frac{\pi\alpha}{4s}[2Re\chi(s)q_q q_\tau a_q a_\tau + |\chi(s)|^2 2v_q a_q 2v_\tau a_\tau] \\
F_3(s) &= \frac{\pi\alpha}{4s}[2Re\chi(s)q_q q_\tau v_q a_\tau + |\chi(s)|^2(v_q^2 + a_q^2)2v_\tau a_\tau] \\
F_4(s) &= \frac{\pi\alpha}{4s}[2Re\chi(s)q_q q_\tau a_q v_\tau + |\chi(s)|^2 2v_q a_q(v_\tau^2 + a_\tau^2)]
\end{aligned} \tag{A.7}$$

From Eq. (A.1) one can notice that terms proportional $\propto Re\chi$ describe the electro-weak interference contribution and terms $\propto |\chi|^2$ describe pure weak interaction. Therefore from Eq. (A.6) and Eq. (A.7) one can derive the separate contributions:

- QED contribution: $1 + \cos^2\theta$
- EWK interference contribution: $2q_q q_\tau[v_q v_\tau(1+\cos^2\theta) + 2a_q a_\tau\cos\theta)]Re\chi(s)$
- Weak contribution: $[(v_q^2 + a_q^2)(v_\tau^2 + a_\tau^2)(1+\cos^2\theta) + 8v_q v_\tau a_q a_\tau\cos\theta]|\chi(s)|^2$

Appendix B

Hadronic τ decays: $\tau \longrightarrow a_1\nu$, $\rho\nu$

Assuming that the 2π and 3π decay channels are resonance dominated:

$$\tau^- \rightarrow \rho^- \bar{\nu}_\tau, \rho^- \rightarrow \pi^- \ \pi^0$$
$$\tau^- \rightarrow a_1^- \bar{\nu}_\tau, a_1^- \rightarrow \pi^- \ \pi^- \ \pi^+ \text{ or } \pi^- \ \pi^0 \ \pi^0$$

we can treat the ρ and a_1 cases together considering the production of spin-one resonance. The decay amplitude for $\tau^- \rightarrow V^- \nu_\tau$ can be written as:

$$M = \frac{G}{\sqrt{2}} g_V \cos\theta_C \bar{u}(l) O^\mu u(k) e^*_\mu(\lambda), \tag{B.1}$$

where l, and k are the momenta of the τ and ν_τ respectively, $O^\mu = \gamma^\mu(1-\gamma_5)$, g_V is a scalar parameter with dimension of m^2, $e_\mu(\lambda)$ the vector describing polarization state of vector meson.

Squaring B.1 and projecting out states of definite τ^- polarization defined by the four-vector s (in the τ rest frame $s = (0,0,0,h)$) and also noting that $\Sigma u(k)\bar{u}(k) = \hat{k}$, $u(l)\bar{u}(l) = (\hat{l} + m)(1+\gamma_5\hat{s})$ and $\gamma_0 O^{\mu\dagger}\gamma_0 = O^\mu$ gives the following relation:

$$\begin{aligned} |M_{\lambda h}|^2 =& \frac{G^2}{2} g_V^2 \cos^2\theta_C e^*_\mu(\lambda) e_\nu(\lambda) Tr[\hat{k}\gamma^\mu(1-\gamma_5)(\hat{l}+m_\tau)(1+\gamma_5\hat{s})\gamma^\nu(1-\gamma_5)] \\ =& G^2 g_V^2 \cos^2\theta_C e^*_\mu(\lambda) e_\nu(\lambda) Tr[\hat{k}\gamma^\mu(\hat{l}+m\hat{s})\gamma^\nu + (\hat{l}+m\hat{s})\gamma^\mu\gamma^\nu\hat{k}\gamma_5]. \end{aligned} \tag{B.2}$$

Using expressions for gamma matrices tr($\gamma^\mu \ \gamma^\nu \ \gamma^\sigma \ \gamma^\rho$) = $4(g^{\mu\nu}g^{\sigma\rho} - g^{\mu\sigma}g^{\nu\rho} + g^{\mu\rho}g^{\nu\sigma})$ and tr($\gamma^\mu \ \gamma^\nu \ \gamma^\sigma \ \gamma^\rho \ \gamma_5$) = $-4i\epsilon_{\mu\nu\sigma\rho}$ one gets (further the normalization factor is ignored):

$$\begin{aligned} |M_{\lambda h}|^2 = k\cdot e^*(\lambda)(l+ms)\cdot e(\lambda) + k\cdot e(\lambda)(l+ms)\cdot e^*(\lambda) + k\cdot(l+ms) - \\ i\epsilon_{\mu\nu\sigma\rho}(l+ms)^\mu e^{*\nu}(\lambda) e^\sigma(\lambda) k^\rho. \end{aligned} \tag{B.3}$$

For the following calculations it is convenient to choose the coordinate system where z axis is defined along the travelling direction of the vector resonance, in this system we have:

$$
\begin{aligned}
e^{\mu}(\pm\lambda) &= \frac{1}{\sqrt{2}}(0,1,i\lambda,0); (\lambda = 1,-1) \\
e^{\mu}(0) &= \frac{1}{M_V}(p_V^*,0,0,E_V^*) \\
l &= (m,0,0,0) \\
s &= (0,0,h\sin\theta,h\cos\theta) \\
k &= (m-E_V^*,0,0,-P_V^*) \\
E_V^* &= \frac{m^2+M_V^2}{2m} \\
p_V^* &= \frac{m^2-M_V^2}{2m},
\end{aligned}
\tag{B.4}
$$

where E_V^* and p_V^* are the energy and momentum of the vector resonance in the τ rest frame. After some calculation the following results are obtained, when the contributions are explicitly written out for the various meson helicity state, λ:

$$
\begin{aligned}
|M_{0h}|^2 =& \frac{m^2-m_V^2}{2}\frac{m^2}{M_V^2}(1+h\cos\theta) \\
|M_{\lambda h}|^2 =& \frac{m^2-m_V^2}{2}(1-\lambda)(1-h\cos\theta)
\end{aligned}
\tag{B.5}
$$

One can note here that amplitude corresponding to $\lambda = 1$ is equal to zero which is a consequence of the spin conservation: this configuration requires the spin of the final state to be 3/2 which cannot be produced in τ decays.

Appendix C

Angular distributions in the decay $\tau \longrightarrow a_1\nu$

As shown in Appendix B the expression of the helicity amplitudes:

$$M_{h\lambda} = j^\mu e^*_\mu(\lambda), \tag{C.1}$$

where $j^\mu = \bar{u}(\nu_\tau)O^\mu u(\tau)$ is the leptonic current and $e^*_\mu(\lambda)$ the polarization vector of the spin 1 resonance.

In the τ rest frame with helicity axis defined along the travel direction of ν_τ the spinors are(ignoring the normalisation factor common for all 4 amplitudes):

$$u(\nu_\tau) = \begin{pmatrix} 0 \\ 1 \\ 0 \\ -1 \end{pmatrix} \qquad\qquad u(\tau) = \begin{pmatrix} c \\ s \\ 0 \\ 0 \end{pmatrix} \tag{C.2}$$

where $c = \cos(\frac{\theta}{2})$ and $s = \sin(\frac{\theta}{2})$.

We want to evaluate $j^\mu e^*_\mu(\lambda)$ for two helicity combinations. It is straightforward to show that for arbitrary spinors $\bar{\psi}\gamma^\mu\phi$:

$$\begin{aligned}
\bar{\psi}\gamma^0\phi &= \psi^\dagger\gamma^0\gamma^0\phi = \psi_1^*\phi_1 + \psi_2^*\phi_2 + \psi_3^*\phi_3 + \psi_4^*\phi_4 \\
\bar{\psi}\gamma^1\phi &= \psi^\dagger\gamma^0\gamma^1\phi = \psi_1^*\phi_4 + \psi_2^*\phi_3 + \psi_3^*\phi_2 + \psi_4^*\phi_1 \\
\bar{\psi}\gamma^2\phi &= \psi^\dagger\gamma^0\gamma^2\phi = -i(\psi_1^*\phi_4 - \psi_2^*\phi_3 + \psi_3^*\phi_2 - \psi_4^*\phi_1) \\
\bar{\psi}\gamma^3\phi &= \psi^\dagger\gamma^0\gamma^3\phi = \psi_1^*\phi_3 - \psi_2^*\phi_4 + \psi_3^*\phi_1 - \psi_4^*\phi_2,
\end{aligned}$$

and

$$(1-\gamma_5)u(\tau) = \begin{pmatrix} c \\ s \\ -c \\ -s \end{pmatrix}.$$

Consider M_{--} and M_{0-} with definition of $e^*(\lambda)$ B the result is:

$$M_{--} = \sqrt{2}\cos\frac{\theta}{2} \qquad\qquad M_{-0} = \frac{m}{M_V}\sin\frac{\theta}{2}, \tag{C.3}$$

The other amplitudes can be obtained in an analogous manner and found to be:

$$M_{+-} = -\sqrt{2}\sin\frac{\theta}{2} \qquad\qquad M_{+0} = \frac{m}{M_V}\cos\frac{\theta}{2}. \tag{C.4}$$

In order to get observable quantities and compute the decay distribution the amplitudes (C.3),(C.4) must be transformed to the laboratory helicity frame. It corresponds to the rotation by angle η, which is the angle between the laboratory helicity axis and the τ rest frame helicity axis, in the 3π rest frame, and the cosine of such angle is given by:

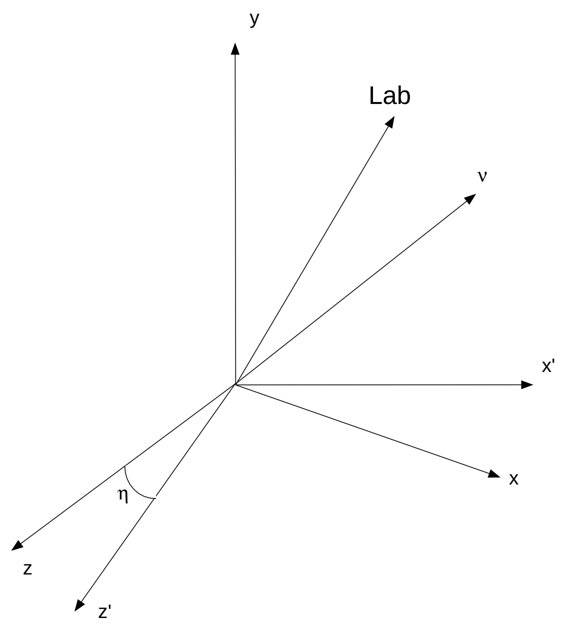

Figure 55: Definition of angle η

$$\cos\eta = \frac{x_V(m^2+M_V^2)-2M_V^2}{(m^2-M_V^2)\sqrt{x_V^2-M_V^2/E_\tau}} \approx \frac{\cos\theta(m^2+M_V^2)+(m^2-M_V^2)}{\cos\theta(m^2-M_V^2)+(m^2+M_V^2)} \quad (E_\tau/m \gg 1), \tag{C.5}$$

where $x_V = \frac{E_V}{E_\tau}$ and $\cos\theta$ can be expressed in laboratory frame quantities as:

$$\cos\theta = \frac{2x_V m^2 - m^2 - M_V^2}{(m^2-Q^2)\sqrt{1-m^2/E_\tau^2}} \approx \frac{2x_V - 1 - M_V^2/m^2}{1-M_V^2/m^2} \quad (E_\tau/m \gg 1). \tag{C.6}$$

The $\tau \to V\nu_\tau$ amplitudes $M'_{h\lambda}$ in the laboratory frame can be obtained from amplitudes M (C.3), (C.4) by a Wigner rotation [61]:

$$M'_{h\lambda'}(\theta) = \sum_{\lambda} d^1_{\lambda'\lambda}(\eta) M_{h\lambda(\theta)}, \tag{C.7}$$

where $d^1_{\lambda'\lambda}$ are the elements of Wigner d-matrix. Using the amplitudes M the amplitudes in the lab frame M' are found to be:

$$\begin{aligned}
M'_{--} &= \frac{1+\cos\eta}{\sqrt{2}}\cos\frac{\theta}{2} - \frac{m}{M_V}\frac{\sin\eta}{\sqrt{2}}\sin\frac{\theta}{2} \\
M'_{+-} &= -\frac{1+\cos\eta}{\sqrt{2}}\sin\frac{\theta}{2} - \frac{m}{M_V}\frac{\sin\eta}{\sqrt{2}}\cos\frac{\theta}{2} \\
M'_{-0} &= \frac{m}{M_V}\cos\eta\sin\frac{\theta}{2} - \sin\eta\cos\frac{\theta}{2} \\
M'_{+0} &= \frac{m}{M_V}\cos\eta\cos\frac{\theta}{2} - \sin\eta\sin\frac{\theta}{2}.
\end{aligned}$$

Hence the distributions in the laboratory frame reads as follow:

$$\begin{aligned}
\frac{1}{\Gamma_V}\frac{d\Gamma^L_V}{dx_V} = \frac{m^2 M_V^2}{(m^2+2M_V^2)(m^2-M_V^2)} &\Big[\frac{m^2}{M_V^2}\cos^2\eta + \sin^2\eta + P_\tau\cos\theta \\
&\times\Big(\frac{m^2}{M_V^2}\cos^2\eta + \frac{m}{M_V}\sin 2\eta tg\theta - \sin^2\eta\Big)\Big]
\end{aligned} \tag{C.8}$$

$$\begin{aligned}
\frac{1}{\Gamma_V}\frac{d\Gamma^T_V}{dx_V} = \frac{m^2 M_V^2}{(m^2+2M_V^2)(m^2-M_V^2)} &\Big[\frac{m^2}{M_V^2}\sin^2\eta + \cos^2\eta + 1 + P_\tau\cos\theta \\
&\times\Big(\frac{m^2}{M_V^2}\sin^2\eta - \frac{m}{M_V}\sin 2\eta tg\theta - \sin^2\eta - 1\Big)\Big].
\end{aligned} \tag{C.9}$$

Appendix D

Event Fit Formalism

The method of Lagrange multipliers allows to minimize or maximize a function with constraints. To find a general solution for the unknown parameters $\vec{a}$ and $\vec{b}$ with the set of measured parameters $\vec{y}$ the Lagrange function:

$$L = (\vec{y} - \vec{a})^T \boldsymbol{V}_y^{-1} (\vec{y} - \vec{a}) + \vec{f}^T(\vec{a}, \vec{b}) \boldsymbol{V}_f^{-1} \vec{f}(\vec{a}, \vec{b}) + 2\vec{\lambda}^T \vec{H}(\vec{a}, \vec{b}) \tag{D.1}$$

is to be minimized. The vectors $\vec{a}$ and $\vec{b}$ are composed of $n \times m$ parameters:

$$\vec{a} = \begin{pmatrix} a_1 \\ a_2 \\ \vdots \\ a_n \end{pmatrix} \qquad \vec{b} = \begin{pmatrix} b_1 \\ b_2 \\ \vdots \\ b_m. \end{pmatrix} \tag{D.2}$$

$\boldsymbol{V}_y$ is the covariance matrix of parameters $\vec{a}$ and $\boldsymbol{V}_f$ is a covariance matrix of both $\vec{a}$ and $\vec{b}$ propagated through the functions $\vec{f}$.

The r functions $\vec{H}$ and k functions $\vec{f}$, describing physical constraints, are defined in a form:

$$\vec{H}(\vec{a}, \vec{b}) = 0 \qquad \vec{f}(\vec{a}, \vec{b}) = 0. \tag{D.3}$$

It is assumed that the constraint functions can be linearized by expanding around some convenient points $\vec{a}_0$ and $\vec{b}_0$. In the iterative procedure the points of expansion for every iteration can be chosen as the solution for $\vec{a}$ and $\vec{b}$ obtained in the previous iteration. While for the first iteration a reasonable, estimation of the parameters of interest serves as expansion points.

Expanding Eq. (D.3) gives the linearized equations:

$$\begin{aligned} \boldsymbol{H}_a \Delta\vec{a} + \boldsymbol{H}_b \Delta\vec{b} + \vec{H}_0(\vec{a}_0, \vec{b}_0) = 0 \\ \boldsymbol{F}_a \Delta\vec{a} + \boldsymbol{F}_b \Delta\vec{b} + \vec{F}_0(\vec{a}_0, \vec{b}_0) = 0 \end{aligned} \tag{D.4}$$

where $\Delta\vec{a} = \vec{a} - \vec{a}_0$, $\Delta\vec{b} = \vec{b} - \vec{b}_0$. The matrices $\boldsymbol{H}_a$, $\boldsymbol{H}_b$, $\boldsymbol{F}_a$, $\boldsymbol{F}_b$ are Jacobians of the constraints $\vec{H}$ and $\vec{f}$ with respect to parameters $\vec{a}$ and $\vec{b}$ and given by:

$$\boldsymbol{H}_a = \begin{pmatrix} \frac{\partial H_1}{\partial a_1} & \frac{\partial H_1}{\partial a_2} & \cdots & \frac{\partial H_1}{\partial a_n} \\ \frac{\partial H_2}{\partial a_1} & \frac{\partial H_2}{\partial a_2} & \cdots & \frac{\partial H_2}{\partial a_n} \\ \vdots & \vdots & \ddots & \vdots \\ \frac{\partial H_r}{\partial a_1} & \frac{\partial H_r}{\partial a_2} & \cdots & \frac{\partial H_r}{\partial a_n} \end{pmatrix} \qquad \boldsymbol{H}_b = \begin{pmatrix} \frac{\partial H_1}{\partial b_1} & \frac{\partial H_1}{\partial b_2} & \cdots & \frac{\partial H_1}{\partial b_m} \\ \frac{\partial H_2}{\partial b_1} & \frac{\partial H_2}{\partial b_2} & \cdots & \frac{\partial H_2}{\partial b_m} \\ \vdots & \vdots & \ddots & \vdots \\ \frac{\partial H_r}{\partial b_1} & \frac{\partial H_r}{\partial b_2} & \cdots & \frac{\partial H_r}{\partial b_m} \end{pmatrix} \tag{D.5}$$

$$\boldsymbol{F}_a = \begin{pmatrix} \frac{\partial F_1}{\partial a_1} & \frac{\partial F_1}{\partial a_2} & \cdots & \frac{\partial F_1}{\partial a_n} \\ \frac{\partial F_2}{\partial a_1} & \frac{\partial F_2}{\partial a_2} & \cdots & \frac{\partial F_2}{\partial a_n} \\ \vdots & \vdots & \ddots & \vdots \\ \frac{\partial F_k}{\partial a_1} & \frac{\partial F_k}{\partial a_2} & \cdots & \frac{\partial F_k}{\partial a_n} \end{pmatrix} \qquad \boldsymbol{F}_b = \begin{pmatrix} \frac{\partial F_1}{\partial b_1} & \frac{\partial F_1}{\partial b_2} & \cdots & \frac{\partial F_1}{\partial b_m} \\ \frac{\partial F_2}{\partial b_1} & \frac{\partial F_2}{\partial b_2} & \cdots & \frac{\partial F_2}{\partial b_m} \\ \vdots & \vdots & \ddots & \vdots \\ \frac{\partial F_k}{\partial b_1} & \frac{\partial F_k}{\partial b_2} & \cdots & \frac{\partial F_k}{\partial b_m} \end{pmatrix} \tag{D.6}$$

$\vec{H}_0$ and $\vec{F}_0$ are the constraint values at the linearization point:

$$\vec{H}_0 = \begin{pmatrix} H_1(\vec{a}_0, \vec{b}_0) \\ H_2(\vec{a}_0, \vec{b}_0) \\ \vdots \\ H_r(\vec{a}_0, \vec{b}_0) \end{pmatrix} \qquad \vec{F}_0 = \begin{pmatrix} F_1(\vec{a}_0, \vec{b}_0) \\ F_2(\vec{a}_0, \vec{b}_0) \\ \vdots \\ F_k(\vec{a}_0, \vec{b}_0). \end{pmatrix} \tag{D.7}$$

It is worth noting, that the actual representation of the parameters $\vec{a}$ and $\vec{b}$ must be chosen such that the constraint functions are linear. However, often this is not possible which leads to the fact that the Eq. (D.4) are not longer acceptable approximations. In case of highly non-linear constraints one can diminish this effect by expanding Eq. (D.3) to the second or higher orders, but it will make further calculations much more complex.

The solution for set of parameters $\vec{a}$ and $\vec{b}$ can be found now by minimizing Eq. (D.1) with respect to $\vec{a}$, $\vec{b}$ and $\vec{\lambda}$. Substituting in Eq. (D.1) $\vec{H}$ and $\vec{f}$ by

$$\begin{aligned} \vec{H}(\vec{a}, \vec{b}) &= \boldsymbol{H}_a(\vec{a} - \vec{a}_0) + \boldsymbol{H}_b(\vec{b} - \vec{b}_0) + \vec{H}_0(\vec{a}_0, \vec{b}_0) \\ \vec{f}(\vec{a}, \vec{b}) &= \boldsymbol{F}_a(\vec{a} - \vec{a}_0) + \boldsymbol{F}_b(\vec{b} - \vec{b}_0) + \vec{F}_0(\vec{a}_0, \vec{b}_0) \end{aligned} \tag{D.8}$$

and performing derivation one gets the equations:

$$\begin{aligned} \frac{\partial L}{\partial \vec{a}} &= -\boldsymbol{V}^{-1}\vec{y} + \boldsymbol{V}^{-1}\vec{a} + \boldsymbol{F}_a^T \boldsymbol{V}_f^{-1} \vec{F}_0 + \boldsymbol{F}_a^T \boldsymbol{V}_f^{-1} \boldsymbol{F}_a^T \Delta\vec{a} + \boldsymbol{F}_a^T \boldsymbol{V}_f^{-1} \boldsymbol{F}_b^T \Delta\vec{b} + \boldsymbol{H}_a^T \vec{\lambda} = 0 \\ \frac{\partial L}{\partial \vec{b}} &= \boldsymbol{F}_b^T \boldsymbol{V}_f^{-1} \vec{F}_0 + \boldsymbol{F}_b^T \boldsymbol{V}_f^{-1} \boldsymbol{F}_a^T \Delta\vec{a} + \boldsymbol{F}_b^T \boldsymbol{V}_f^{-1} \boldsymbol{F}_b^T \Delta\vec{b} + \boldsymbol{H}_b^T \vec{\lambda} = 0 \\ \frac{\partial L}{\partial \vec{\lambda}} &= \boldsymbol{H}_a \Delta\vec{a} + \boldsymbol{H}_b \Delta\vec{b} + \vec{H}_0 = 0. \end{aligned} \tag{D.9}$$

It is straightforward to find the parameters $\vec{a}$, $\vec{b}$ and $\vec{\lambda}$ from these three linear equations, after some algebra one can write them in a short matrix form as:

$$\begin{pmatrix} \boldsymbol{V}^{-1} + \boldsymbol{F}_a^T \boldsymbol{V}_f^{-1} \boldsymbol{F}_a & \boldsymbol{F}_a^T \boldsymbol{V}_f^{-1} \boldsymbol{F}_b & \boldsymbol{H}_a^T \\ \boldsymbol{F}_b^T \boldsymbol{V}_f^{-1} \boldsymbol{F}_a & \boldsymbol{F}_b^T \boldsymbol{V}_f^{-1} \boldsymbol{F}_b & \boldsymbol{H}_b^T \\ \boldsymbol{H}_a & \boldsymbol{H}_b & \boldsymbol{0} \end{pmatrix} \begin{pmatrix} \vec{a} \\ \vec{b} \\ \vec{\lambda} \end{pmatrix} = \begin{pmatrix} \boldsymbol{V}_y^{-1}\vec{y} - \boldsymbol{F}_a^T \boldsymbol{V}_f^{-1}(\vec{F}_0 - \boldsymbol{F}_a\vec{a}_0 - \boldsymbol{F}_b\vec{b}_0) \\ -\boldsymbol{F}_b^T \boldsymbol{V}_f^{-1}(\vec{F}_0 - \boldsymbol{F}_a\vec{a}_0 - \boldsymbol{F}_b\vec{b}_0) \\ \boldsymbol{H}_a\vec{a}_0 + \boldsymbol{H}_b\vec{b}_0 - \vec{H}_0 \end{pmatrix} \tag{D.10}$$

The corresponding value L_{min} can be found by using Eq.(D.1)with the obtained parameters $\vec{a}, \vec{b}, \vec{\lambda}$.

Appendix E

Perturbative QCD corrections to Drell-Yan process

The calculation of $\mathcal{O}(\alpha_S)$ correction to the Drell-Yan process has been performed by many authors. The description and qualitative discussion can be found in Ref. [62]. The full result for the Drell-Yan cross section corresponding to Feynman diagrams shown in Fig. 56, in the $\overline{\text{MS}}$ scheme with $\mu^2 = M^2$, for a given quark flavor q, is:

$$
\begin{aligned}
\frac{d\hat{\sigma}(M^2)}{dM^2} &= \int_0^1 \frac{d\sigma_{q\bar{q}}(M^2)}{dM^2}\tau dx_1 dx_2 dz \delta(x_1 x_2 z - \tau) \\
&\times \Bigg[\left\{ f_q(x_1, M^2) f_{\bar{q}}(x_2, M^2) + (q \leftrightarrow \bar{q}) \right\} \left(\delta(1-z) + \frac{\alpha_S(M^2)}{2\pi} D_q(z) \right) \\
&+ \left\{ f_g(x_1, M^2)(f_q(x_2, M^2) + f_{\bar{q}}(x_x, M^2)) + (q, \bar{q} \leftrightarrow g) \right\} \frac{\alpha_S(M^2)}{2\pi} D_g(z) \Bigg],
\end{aligned} \tag{E.1}
$$

where, M -invariant mass of the lepton pair, x - part of the proton momentum carried by the parton, $f_q(x)$, $f_{\bar{q}}(x)$ - the parton distribution functions extracted from deep inelastic scattering data. The functions $D_q(z)$ and $D_g(z)$ are given by ($C_F = \frac{4}{3}$, $T_R = \frac{1}{2}$) :

$$
\begin{aligned}
D_q(z) &= C_F \left[4(1+z^2) \left(\frac{\ln(1-z)}{1-z} \right)_+ - 2\frac{1+z^2}{1-z} \ln z + \delta(1-z) \left(\frac{2\pi^2}{3} - 8 \right) \right] \\
D_g(z) &= T_R \left[(z^2 + (1-z)^2) \ln \frac{(1-z)^2}{z} + \frac{1}{2} + 3z - \frac{7}{2} z^2 \right].
\end{aligned} \tag{E.2}
$$

The plus function in (E.2) can be evaluated using the following relations:

$$
\begin{aligned}
\int_0^1 dx F_+(x) G(x) &= \int_0^1 dx F(x) [G(x) - G(1)] \\
\int_a^1 dx F_+(x) G(x) &= \int_a^1 dx F(x) [G(x) - G(1)] + G(1) \int_0^a dx F(x).
\end{aligned} \tag{E.3}
$$

It is also convenient to evaluate the integral with $D_q(z)$ term in hyperbolic coordinates:

$$u = \ln \sqrt{\frac{x_1}{x_2}}; \qquad v = \sqrt{x_1 x_2}$$

The $\mathcal{O}(\alpha_S^2)$ corrections to the Drell-Yan cross section can be found in Ref. [63].

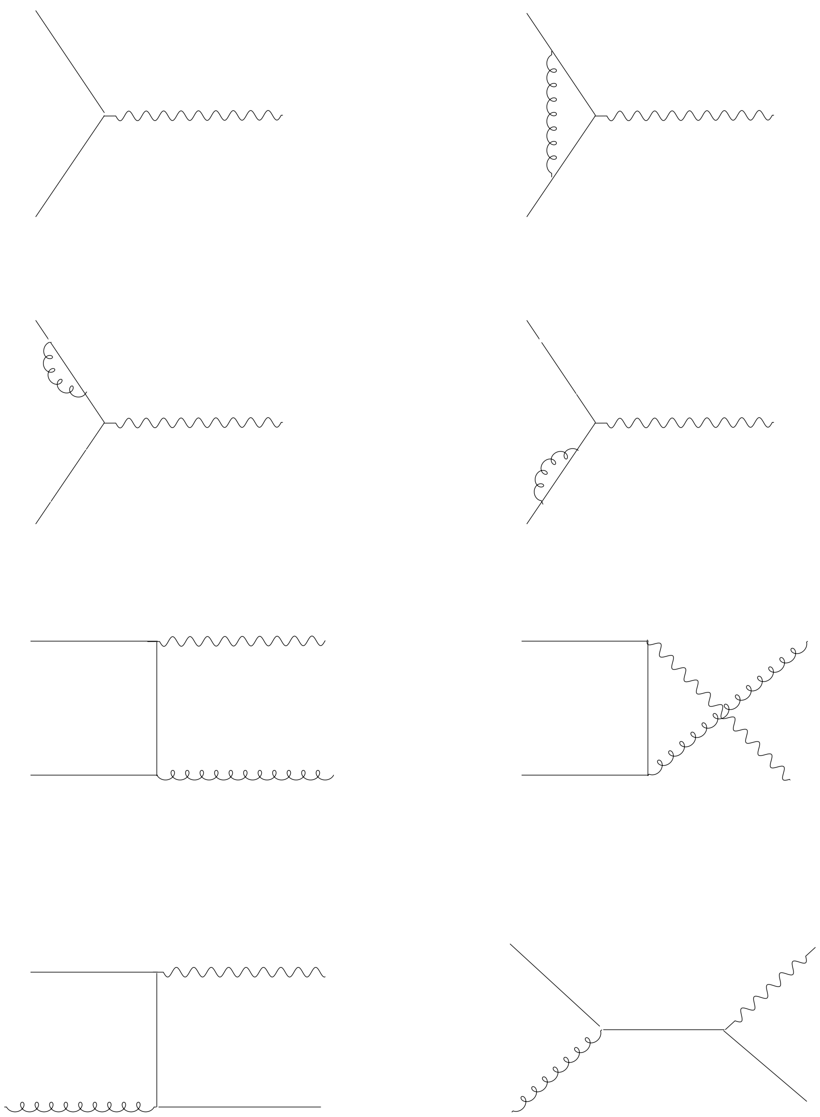

Figure 56: The leading- and next-to-leading-order diagrams for the Drell-Yan process .

Acknowledgements

I would like to acknowledge Achim Stahl and IIIB Aachen tau group for giving me the opportunity to perform this measurement and discussions. I am grateful to Ian Nugent for the very fruitfull collaboration. During this work I benefited from helpful discussions with Zbigniew Was, Tomasz Przedzinski, Mikhail Pletyukhov and Tord Riemann who also provided a very helpful guidance on the usage of ZFitter package. I am deeply indebted to Wolfgang Lohmann for his inestimable help in all aspects.

References

[1] ALEPH, CDF, D0, DELPHI, L3, OPAL, SLD Collaborations, the LEP Electroweak Working Group, the Tevatron Electroweak Working Group, and the SLD Electroweak and Heavy Flavour Groups, "Precision electroweak measurements and constraints on the Standard Model", (2010). arXiv:1012.2367.

[2] SLD Electroweak Group, DELPHI, ALEPH, SLD, SLD Heavy Flavour Group, OPAL, LEP Electroweak Working Group, L3 Collaboration, "Precision electroweak measurements on the Z resonance", *Phys. Rept.* **427** (2006) 257–454, doi:10.1016/j.physrep.2005.12.006, arXiv:hep-ex/0509008.

[3] E. Noether, "Invariant Variation Problems", *Gott. Nachr.* **1918** (1918) 235–257, doi:10.1080/00411457108231446, arXiv:physics/0503066. [Transp. Theory Statist. Phys.1,186(1971)].

[4] D. Hanneke, S. Fogwell, and G. Gabrielse, "New Measurement of the Electron Magnetic Moment and the Fine Structure Constant", *Phys. Rev. Lett.* **100** (2008) 120801, doi:10.1103/PhysRevLett.100.120801, arXiv:0801.1134.

[5] S. L. Glashow, "Partial Symmetries of Weak Interactions", *Nucl. Phys.* **22** (1961) 579–588, doi:10.1016/0029-5582(61)90469-2.

[6] S. Weinberg, "A Model of Leptons", *Phys. Rev. Lett.* **19** (1967) 1264–1266, doi:10.1103/PhysRevLett.19.1264.

[7] A. Salam, "Weak and Electromagnetic Interactions", *Conf. Proc.* **C680519** (1968) 367–377.

[8] P. W. Higgs, "Broken Symmetries and the Masses of Gauge Bosons", *Phys. Rev. Lett.* **13** (1964) 508–509, doi:10.1103/PhysRevLett.13.508.

[9] F. Halzen and A. Martin, "Quarks and leptons: an introductory course in modern particle physics". Wiley, 1984.

[10] A. Akhundov, A. Arbuzov, S. Riemann, and T. Riemann, "The ZFITTER project", *Phys. Part. Nucl.* **45** (2014), no. 3, 529–549, doi:10.1134/S1063779614030022, arXiv:1302.1395.

[11] M. I. Vysotsky, V. A. Novikov, L. B. Okun, and A. N. Rozanov, "Electroweak radiative corrections in Z boson decays", *Phys. Usp.* **39** (1996) 503–538, doi:10.1070/PU1996v039n05ABEH000146, arXiv:hep-ph/9606253. [Usp. Fiz. Nauk166,539(1996)].

[12] S. D. Drell and T.-M. Yan, "Partons and their Applications at High-Energies", *Annals Phys.* **66** (1971) 578, doi:10.1016/0003-4916(71)90071-6. [Annals Phys.281,450(2000)].

[13] A. D. Martin, W. J. Stirling, R. S. Thorne, and G. Watt, "Parton distributions for the LHC", *Eur. Phys. J.* **C63** (2009) 189–285, doi:10.1140/epjc/s10052-009-1072-5, arXiv:0901.0002.

[14] Y.-S. Tsai, "Decay Correlations of Heavy Leptons in e+ e- → Lepton+ Lepton-", *Phys.Rev.* **D4** (1971) 2821, doi:10.1103/PhysRevD.13.771,10.1103/PhysRevD.4.2821.

[15] M. L. Perl et al., "Evidence for Anomalous Lepton Production in e+ - e- Annihilation", *Phys. Rev. Lett.* **35** (1975) 1489–1492, doi:10.1103/PhysRevLett.35.1489.

[16] PLUTO Collaboration, "Anomalous Muon Production in e+ e- Annihilation as Evidence for Heavy Leptons", *Phys. Lett.* **B68** (1977) 297, doi:10.1016/0370-2693(77)90292-1.

[17] A. Barbaro-Galtieri et al., "Electron-Muon and electron-Hadron Production in e+ e- Collisions", *Phys. Rev. Lett.* **39** (1977) 1058, doi:10.1103/PhysRevLett.39.1058.

[18] Particle Data Group Collaboration, "Review of Particle Physics", *Chin. Phys.* **C38** (2014) 090001, doi:10.1088/1674-1137/38/9/090001.

[19] ALEPH Collaboration, "An Upper limit on the tau-neutrino mass from three-prong and five-prong tau decays", *Eur. Phys. J.* **C2** (1998) 395–406, doi:10.1007/s100520050149.

[20] ARGUS Collaboration, "A Measurement of the tau mass", *Phys. Lett.* **B292** (1992) 221–228, doi:10.1016/0370-2693(92)90634-G.

[21] V. V. Anashin et al., "Measurement of the tau lepton mass at the KEDR detector", *JETP Lett.* **85** (2007) 347–352, doi:10.1134/S0021364007080012.

[22] DASP Collaboration, "Measurements of tau Decay Modes and a Precise Determination of the Mass", *Phys. Lett.* **B73** (1978) 109–114, doi:10.1016/0370-2693(78)90183-1.

[23] OPAL Collaboration, "Improved measurement of the lifetime of the tau lepton", *Phys. Lett.* **B374** (1996) 341–350, doi:10.1016/0370-2693(96)00255-9.

[24] A. Stahl, "Physics with tau leptons", *Springer Tracts Mod. Phys.* **160** (2000) 1–316.

[25] S. Gerstein and Y. Zeldovich *Sov. Phys. JETP* **2** (1956) 576.

[26] R. P. Feynman and M. Gell-Mann, "Theory of the Fermi Interaction", *Phys. Rev.* **109** (Jan, 1958) 193–198, doi:10.1103/PhysRev.109.193.

[27] L. B. Okun, "Leptons and Quarks". North-Holland, Amsterdam, 1982.

[28] S. Eidelman, "Status of CVC tests from hadrons and tau lepton decays", *eConf* **C010430** (2001) M07. [16(2001)].

[29] V. A. Cherepanov and S. I. Eidelman, "Conserved vector current and decays tau", *JETP Lett.* **89** (2009) 429–431, doi:10.1134/S002136400909001X. [Pisma Zh. Eksp. Teor. Fiz.89,515(2009)].

[30] S. Weinberg, "Precise relations between the spectra of vector and axial vector mesons", *Phys. Rev. Lett.* **18** (1967) 507–509, doi:10.1103/PhysRevLett.18.507.

[31] M. Davier, A. Hocker, and Z. Zhang, "The Physics of hadronic tau decays", *Rev. Mod. Phys.* **78** (2006) 1043–1109, doi:10.1103/RevModPhys.78.1043, arXiv:hep-ph/0507078.

[32] S. M. Berman and M. Jacob, "SYSTEMATICS OF ANGULAR POLARIZATION DISTRIBUTIONS IN THREE-BODY DECAYS", *Phys. Rev.* **139** (1965) B1023–B1038, doi:10.1103/PhysRev.139.B1023.

[33] M. Davier, L. Duflot, F. Le Diberder, and A. Rouge, "The Optimal method for the measurement of tau polarization", *Phys.Lett.B* **306** (1993) 411–417, doi:10.1016/0370-2693(93)90101-M.

[34] J. H. Kuhn and E. Mirkes, "Structure functions in τ decays", *Z.Phys.* **C56** (1992) 661–672, doi:10.1007/BF01474741.

[35] P. Privitera, "Structure functions in tau $\rightarrow 3\pi\nu_\tau$ and the tau polarization measurement", *Phys.Lett.* **B308** (1993) 163–173, doi:10.1016/0370-2693(93)90617-Q.

[36] O. S. Brüning et al., "LHC Design Report". CERN, Geneva, 2004.

[37] CMS Collaboration Collaboration, T. C. collaboration, "CMS Physics: Technical Design Report Volume 1: Detector Performance and Software". Technical Design Report CMS. CERN, Geneva, 2006. There is an error on cover due to a technical problem for some items.

[38] ATLAS Collaboration, "ATLAS: Technical proposal for a general-purpose p p experiment at the Large Hadron Collider at CERN",.

[39] LHCb Collaboration, "The LHCb Detector at the LHC", *JINST* **3** (2008) S08005, doi:10.1088/1748-0221/3/08/S08005.

[40] ALICE Collaboration Collaboration, "ALICE: Technical proposal for a Large Ion collider Experiment at the CERN LHC". LHC Tech. Proposal. CERN, Geneva, 1995.

[41] CMS Collaboration Collaboration, "Description and performance of track and primary-vertex reconstruction with the CMS tracker", *J. Instrum.* **9** (May, 2014) P10009. 80 p. Comments: Replaced with published version. Added journal reference and DOI.

[42] CMS Collaboration, "Tau POG,Performance of tau reconstruction and identification in pp collisions at sqrt(s) = 8 TeV", CMS Note 2014/008, 2014.

[43] CMS Collaboration, "Particle Flow Event Reconstruction in CMS and Performance for Jets, Taus, and MET", CMS Physics Analysis Summary CMS-PAS-PFT-09-001, 2009.

[44] CMS Collaboration, "Search for MSSM Neutral Higgs Bosons Decaying to Tau Pairs in pp Collisions with improved Tau ID and Tau PT Categories", CMS Note 2014/074, 2014.

[45] CMS Collaboration, "Measurement of the $t\bar{t}$ production cross section in the dilepton channel in pp collisions at $\sqrt{s} = 8$ TeV", *JHEP* **1402** (2014) 024, doi:10.1007/JHEP02(2014)024, 10.1007/JHEP02(2014)102, arXiv:1312.7582.

[46] CMS Collaboration, "Search for the Standard-Model Higgs boson decaying to tau pairs in proton-proton collisions at sqrt(s)= 7 and 8 TeV", CMS Physics Analysis Summary CMS-PAS-HIG-13-004, 2013.

[47] K. Melnikov and F. Petriello, "Electroweak gauge boson production at hadron colliders through $\mathcal{O}(\alpha_s^2)$", *Phys. Rev. D* **74** (Dec, 2006) 114017, doi:10.1103/PhysRevD.74.114017.

[48] S. Jadach, Z. Was, R. Decker, and J. H. Kuhn, "The tau decay library TAUOLA: Version 2.4", *Comput. Phys. Commun.* **76** (1993) 361–380, doi:10.1016/0010-4655(93)90061-G.

[49] Z. Czyczula, T. Przedzinski, and Z. Was, "TauSpinner Program for Studies on Spin Effect in tau Production at the LHC", *Eur.Phys.J.* **C72** (2012) 1988, doi:10.1140/epjc/s10052-012-1988-z, arXiv:1201.0117.

[50] GEANT4 Collaboration, "GEANT4: A Simulation toolkit", *Nucl. Instrum. Meth.* **A506** (2003) 250–303, doi:10.1016/S0168-9002(03)01368-8.

[51] C. Collaboration, "Performance of muon identification in pp collisions at sqrt(s) = 7 TeV", CMS Physics Analysis Summary CMS-PAS-MUO-10-002, 2010.

[52] CMS Collaboration, "Search for additional neutral Higgs bosons decaying to a pair of tau leptons in pp collisions at sqrt(s) = 7 and 8 TeV", Technical Report CMS-PAS-HIG-14-029, CERN, Geneva, 2015.

[53] CMS Collaboration Collaboration, "MET performance in 8 TeV data", Technical Report CMS-PAS-JME-12-002, CERN, Geneva, 2013.

[54] CMS Collaboration, "Kinematic Reconstruction of Tau Lepton", CMS Note 2010/256, 2010.

[55] CMS Collaboration, "Vertex Fitting with the Kalman Filter Formalism in the ORCA Reconstruction Program", CMS Note 2003/008, 2003.

[56] T. Pierzchala, E. Richter-Was, Z. Was, and M. Worek, "Spin effects in tau lepton pair production at LHC", *Acta Phys.Polon.* **B32** (2001) 1277–1296, arXiv:hep-ph/0101311.

[57] J. H. Kuhn and A. Santamaria, "Tau decays to pions", *Z.Phys.* **C48** (1990) 445–452, doi:10.1007/BF01572024.

[58] N. Isgur, C. Morningstar, and C. Reader, "The a1 in tau Decay", *Phys. Rev.* **D39** (1989) 1357, doi:10.1103/PhysRevD.39.1357.

[59] M. Feindt, "Measuring Hadronic Currents and Weak Coupling Constants in $\tau \to$ Neutrino 3 π", *Z. Phys.* **C48** (1990) 681–688, doi:10.1007/BF01614704.

[60] O. Shekhovtsova et al., "RChL currents in Tauola: implementation and fit parameters", *Nucl. Phys. Proc. Suppl.* **253-255** (2014) 73–76, doi:10.1016/j.nuclphysbps.2014.09.018, arXiv:1301.1964.

[61] A. Martin and T. Spearman, "Elementary particle theory". North-Holland, Amsterdam, 1970.

[62] R. Ellis, W. Stirling, and B. Webber, "QCD and Collider Physics". Cambridge Monographs on Particle Physics, Nuclear Physics and Cosmology. Cambridge University Press, 2003.

[63] V. M. Braun and A. V. Kolesnichenko, "POWER CORRECTIONS TO BJORKEN AND GROSS-LLEWELLYN SMITH SUM RULES IN QCD", *Nucl. Phys.* **B283** (1987) 723, doi:10.1016/0550-3213(87)90295-1.